Predicting Detection of Changes in Controlled Element Dynamics by Human Controllers Internal Model

Thomas Eppenga

Predicting Detection of Changes in Controlled Element Dynamics by Human Controllers Internal Model

by

Thomas Eppenga

to obtain the degree of Master of Science
at the Delft University of Technology.

Student number:	4541677
Project duration:	March 2023-March 2024
Supervisors:	Prof. dr. ir. M. Mulder
	Dr. ir. M. M. van Paassen
	Dr. ir. D. M. Pool
External Examiner:	Dr. O. A. Sharpans'kykh

Delft
University of
Technology

Preface

This report covers my work from the past year, starting with a scientific article and followed by a thesis report. It was a tough project with many challenges, but I'm proud of the result. I want to thank my supervisors, Daan, Max, and Rene, for their guidance and ideas. Without them, I couldn't have done this. Also, a big thanks to my family for supporting me through the tough times.

I hope you enjoy reading my thesis!

Thomas Eppenga
Delft, March 2024

Cover Image: Image generated using ImageFX

Contents

List of Figures

List of Tables

Nomenclature

Abbreviations

Abbreviation	Definition
CE	Controlled Element Dynamics
CDF	Cumulative Distribution Function
DI	Double Integrator
HMI	Human-Machine Interface
K-S test	Kolmogorov-Smirnov Test
MC	Monte Carlo
NASA	National Aeronautics and Space Administration
SI	Single Integrator

Symbols

Symbol	Definition
A_n	Amplitude
G	Maximum Rate of Change
H_m	Forward Model
H_m^{-1}	Inverse Model
H_n	Remnant Transfer Function
H_p	Pilot Transfer Function
K_m	Gain of the Operator’s Internal Model of Controlled Element Dynamics
K_n	Gain (Remnant Filter)
K_p	Inner Loop Gain
K_r	Outer Loop Gain
M	System Output
P_1	Initial Parameter Value
P_2	Final Parameter Value
T_l	Lead Term
T_i	Lag Term
Δc	Change in Control Input
$\Delta \epsilon$	Change in System Error
$\dot{M}$	Output Rate
τ	Time of Maximum Rate of Change
t_c	Time of Transition
t_s	Small Time Value
y	System Output
y^*	Expectation
α	Location Parameter (Log-Logistic Distribution)

Symbol	Definition
β	Scale Parameter (Log-Logistic Distribution)
μ	Mean
μ_w	Mean (Gaussian White Noise)
σ	Standard Deviation
σ_w^2	Variance (Gaussian White Noise)
ω_m	Base Frequency
ω_{nms}	Natural Frequency (Neuromuscular System)
ϕ_n	Phase
τ_e	Effective Time Delay
ζ_{nms}	Damping Ratio (Neuromuscular System)

Part I

Scientific Article

Predicting Detection of Changes in Controlled Element Dynamics by Human Controllers Internal Model

Author: T. Eppenga; Supervisors: M. Mulder, M.M. van Paassen, D.M. Pool,
Control & Simulation Section, Faculty of Aerospace Engineering
Delft University of Technology, Delft, The Netherlands

Limited knowledge exists regarding how human operators detect changes in the dynamics of their controlled element when performing manual control tasks. This paper introduces a new pursuit-tracking model that includes an explicit observer-like internal model for predicting human controllers' detection of a change in controlled element dynamics. The internal model's innovation signal, defined as the difference between an observation and an expectation of the controlled element's response, is investigated for its capacity to predict the detection of a change. The model's performance is tested for different human controller crossover frequencies, remnant power ratio, observer gain, and detection threshold settings, for offline simulations of pursuit-tracking tasks with a controlled element transition from approximately single to double integrator dynamics. The model shows highly accurate detection performance for a wide range in the observer gain, with a true positive rate of approximately one and a false positive of approximately 0.02. Based on comparison with previously collected human-in-the-loop experiment data, an observer gain between 0.1-0.4 is recommended with a detection threshold of 3-4σ, resulting in an average detection time between 0.9-2.2 seconds for different remnant power ratios and human controller crossover frequency settings. Overall, the high true and low false positive rates, combined with average detection times that match prior human-in-the-loop data, show the observer model's ability to accurately predict human controllers' detection of a change in controlled element dynamics. Further research is needed to validate the approach for a wider set of controlled element variations.

Nomenclature

Abbreviations

AMT = Adaptive Model Theory
CE = Controlled Element
FB = Feedback
FF = Feedforward
FN = False Negative
FP = False Positive
HC = Human Controller
MC = Monte Carlo
MRAC = Model Reference Adaptive Control
ROC = Receiver Operating Characteristic
rms = Root-mean-square
SCA = Supervisory Control Algorithm
TN = True Negative
TP = True Positive

Symbols

$A_t[n]$ = Amplitude of the n$^{\text{th}}$ sinusoid (inch)

C = A constant with $C \in \{1, 2, 3..., 10\}$
$e(t)$ = System error (inch)
$\dot{e}(t)$ = System error rate (inch/s)
$f_t(t)$ = Target function (inch)
G = Maximum rate of change (s^{-1})
$H_{CE}(s)$ = Controlled element dynamics transfer function
$H_n(s)$ = Remnant filter transfer function
$H_m(s)$ = Internal model for CE dynamics transfer function
$H_{nm}(s)$ = Neuromuscular and stick dynamics transfer function
$H_p(s)$ = Human controller transfer function
K = Observer gain
K_n = Remnant filter gain
K_{CE} = Controlled element dynamics gain
K_p = Human controller gain
N = Number of sinusoids
$N_m(s)$ = Internal model for neuromuscular and stick dynamics transfer function
k_n = Prime number
P_1 = Initial parameter value
P_2 = Final parameter value
T = Small-time period (s)
T_I = Lag constant (s)
T_L = Lead constant (s)
T_m = Measurement time (s)
t_c = Time of change in CE dynamics (s)
$u(t)$ = Control input signal (inch)
$y(t)$ = System output (inch)
$y^*(t)$ = Expectation signal (inch)
$x(t)$ = Control signal (inch)
$\eta(t)$ = Innovation signal (inch)
$\omega_b(t)$ = Controlled element time-varying break frequency (rad/s)
ω_c = Crossover frequency (rad/s)
ω_{nm} = Natural frequency (rad/s)
ω_m = Fundamental frequency (rad/s)
$\omega_t[n]$ = Frequency of the n^{th} sinusoid (rad/s)
ϕ_m = Phase margin (degrees)
$\phi_t[n]$ = Phase of the n^{th} sinusoid (rad)
σ_η = Innovation signal standard deviation (inch)
σ_n^2 = Variance of the remnant (inch^2)
σ_η^2 = Variance of the innovation signal (inch^2)
σ_u^2 = Variance of the HC control input signal (inch^2)
τ = Time of maximum rate of change (s)
τ_e = Effective time delay (s)
τ_n = Remnant filter time constant (s)

I. Introduction

In recent decades, automation has increased in many human-in-the-loop systems, notably in aircraft and road vehicles. While automation excels in tasks within controlled environments, such as elevators, where precise positioning and preestablished plans prevail, human adaptability remains indispensable in more dynamic situations, such as commercial aviation [1]. Although current automation achieves or exceeds human-level performance in various tasks, understanding how humans adapt their control strategies can inspire advancements in machine learning and automation engineering [2]. This insight not only aids in the development of more adaptable controllers, but also facilitates the design of improved training programs for human controllers (HC) and safer (semi-)automated support systems, ultimately enhancing safety [2, 3], such as mitigation of loss of control, a major contributor to fatal accidents [4].

During the 1960s, Young et al. [1] performed the first experiments on the HC's adaptive processes and came up with the Adaptive Control Theory. The Adaptive Control Theory identified three human adaptive process phases: detection, identification, and modification [1]. Young et al. [1] state that there are four different types of adaptation: 1) Input Adaptation and Prediction, a human's ability to detect familiar/repeating patterns in the input signal; 2) Controlled Element (CE) Adaptation, human's ability to adapt different control strategies in response to changes in the CE dynamics; 3) Task Adaptation, human's ability to optimise the manual control loop based on various control objectives; 4) Programmed Adaptation, human's way of adapting control strategies, which he/she has been trained, appropriate to the environmental factor [5].

Even though proficient adaptive models can cover all three stages of adaptation, this research focuses on the detection phase. Understanding the detection phase is crucial, as it marks the initiation of the adaptive process, and currently, this stage lacks a thorough understanding [1]. In this study, the emphasis lies on human control adaptation concerning changes in controlled element dynamics. The detection phase of a change in CE dynamics from single (SI) to double integrator-like (DI) will be investigated. This aligns with several recent experiments conducted in a pursuit-tracking task [2, 6–9], allowing for a comparison of results with the experiment carried out by Barragan [9]. The change in CE dynamics was chosen to be from SI to DI, to be able to use McRuer's simplified precision model [10], as the literature suggests this is a valid model for SI pursuit-tracking tasks [11].

In compensatory tracking tasks with changing CE dynamics, various models were developed, notably by Miller and Phatak and Bekey [12, 13], which all rely on a threshold based on system error or error rate. These models are grounded in the concept that adept HCs monitor signal statistical properties, identifying abnormalities when they exceed normal steady-state tracking ranges. For this purpose, HCs use an internal model of CE dynamics to predict signal values. Detecting a significant difference between observed and predicted values enables HC to identify changes in controlled element dynamics.

Mulder et al. [11] came up with the innovation signal for pursuit-tracking tasks. The human operator stores a mental model of the CE dynamics which he/she uses to derive their innovation signal, the difference between the HC observation and expectation of the system output. When the innovation signal crosses the steady-state tracking threshold then the HC will detect a change in CE dynamics.

This research aims to assess the feasibility of using the difference between the observed and expected system output to predict the moment an HC detects a change in CE dynamics during pursuit-tracking tasks. A Monte Carlo (MC) analysis, varying HC parameters such as crossover frequency, remnant power ratios, observer gain, and threshold values, 1 to 10σ of the analytically calculated innovation signal standard deviation, was conducted. Average detection times were compared with experimental data from Barragan's study [9], focusing on a pursuit-tracking task with a CE dynamics shift from SI to DI-like.

The structure of the paper is as follows. First, some background information about models for HC detection of a change in CE dynamics is given and a new model based on the work of Mulder et al. [14] is presented in Section II. The simulation method is presented in Section III. The results and discussion are presented in Sections IV and V, respectively. Finally, the conclusions are presented in Section VI.

II. Adaptive control models

There have been models for how humans detect changes in CE dynamics, however, most of these models are for compensatory displays. A compensatory display only shows the system error $e(t)$. In contrast, pursuit displays show the system output $y(t)$ and the target function $f_t(t)$, as schematically represented in Figure 1.

A. Previous models

Adaptive control models for both compensatory and pursuit displays have been proposed, this section summarizes some of these models.

1. Miller and Elkind model

Miller and Elkind [12] proposed a model for the detection of changes in CE dynamics for compensatory tracking tasks. The model states that the HC has an internal model of the CE dynamics and uses this to derive an expected change in error rate $\widehat{\Delta\dot{e}}$ over a small time interval T [12]. The idea for an internal model of the CE dynamics comes from Knoop and Fu [15]. The HC also observed the actual change in error rate $\Delta\dot{e}$ over a small period T [16]. The discrepancy between the observed and expected change in error rate is called the innovation signal rate $\Delta\dot{\eta}$. The HC,

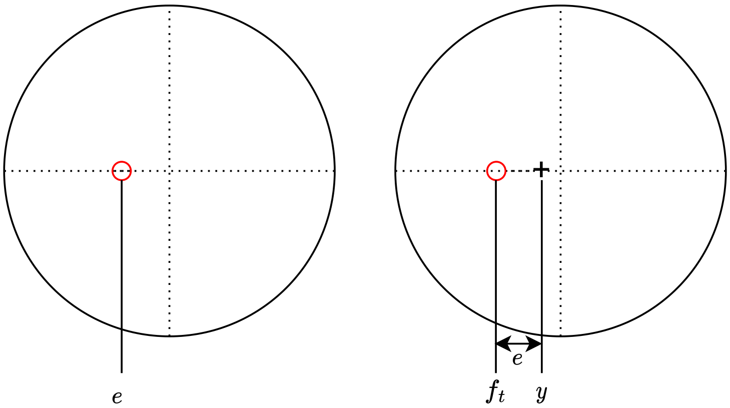

Fig. 1 Schematic overview of a compensatory (left) and a pursuit display (right).

during steady-state tracking, stores thresholds of this change in innovation signal $C\sigma_{\Delta\dot{\eta}}$ with C a multiple of this threshold [12]. When the CE dynamics change and the internal model no longer approximates the real CE dynamics then the change in innovation signal exceeds this threshold. The HC would know that a change in CE dynamics has occurred [12]. The model, however, cannot directly be used for pursuit-tracking tasks as the HC sees the target function $f_t(t)$ and the system output $y(t)$ and must infer the system error $e(t)$, unlike compensatory tracking tasks.

2. Phatak and Bekey model

Phatak and Bekey [13] enhanced a previous model [17] by introducing decision control logic to identify changes in CE dynamics. Their sequential identification model, the Supervisory Control Algorithm (SCA) utilizes pattern recognition of system error $e(t)$ and system error rate $\dot{e}(t)$ to detect changes, with decision regions guiding the process. The human operator is assumed to store maximum system error e_{max} and error rate values $\dot{e}_{\text{max}}$ in steady-state conditions, and when a decision region is surpassed, a change in CE is detected. The decision regions are empirically determined, relying on specific CE dynamics. To validate the model an experiment with a skilled HC simulating time-varying control scenarios demonstrated alignment with expectations [13]. Still, it revealed discrepancies after the second change in system error rate $\dot{e}$. These discrepancies may be attributed to the model's optimality compared to human operators and the stochastic nature of human responses [17].

Van Ham et al. [18] focused on validating Phatak and Bekey's SCA [13] using system error $e(t)$ and system error rate $\dot{e}(t)$. An experiment with six participants revealed that the proposed decision region limits did not align with human adaptive behaviour, prompting the exploration of new detection limits based on standard deviations. Decision region one (DR-1) was originally bounded by $2|\dot{e}_{max}|$ [13], but Van Ham et al. proposed more realistic limits around 3.9σ of system error $e(t)$ or system error rate $\dot{e}(t)$ [18]. The model of Phatak and Bekey also does not carry over for pursuit-tracking tasks, due to being developed for compensatory tracking.

3. Hess's model

Hess's pursuit display model [19] introduces an adaptive pilot control system for multi-axis tracking, focusing on neuromuscular dynamics ($H_{nm}(s)$) and CE dynamics ($H_c(s)$). The model states that the detection of a change in CE dynamics happens based on a trigger function [20]. Hess model [19, 21] works based on a criterion signal x which is the difference between a part of the system error $e(t)$ multiplied with a gain and the system output $y(t)$, all multiplied with a second order transfer function. When the absolute value of the square root of this criterion signal $\sqrt{|x|}$ exceeds three times the root-mean-square (rms) of the absolute value of the square root of the criterion signal $3\text{rms}\left[\sqrt{|x|}\right]$ then the HC would know that a change in CE dynamics has occurred [19, 22].

Jakimovska's assessment of Hess's adaptive pilot model [23] involved analyzing and validating the model's representation of human operator dynamics during pursuit-tracking tasks with time-varying controlled element dynamics, utilizing human-in-the-loop experiments with transitions between single and double integrator CE dynamics. The experiments revealed successful predictions of human adaptation during transitions from a single to a double integrator. However, the reliability of the triggering logic depends on participants' pre-transition crossover frequency. Importantly, the model falls short in predicting behaviour adaptation during transitions from double to single integrator dynamics.

4. *Model Reference Adaptive Control*

Terenzi et al. [2] investigated the prospect of Model Reference Adaptive Control (MRAC) in capturing human adaptive control during a pursuit-tracking task with changes in CE dynamics. MRAC, inspired by predictive coding in neuroscience, includes a feedforward and feedback controller with an internal model from McRuer and Jex's crossover model [2]. Despite accurately predicting transitions from single to double integrator dynamics, MRAC faces challenges in the reverse transition, suggesting its effectiveness in situations requiring significant rate feedback adaptation [2]. The model requires a lot of tracking data and is highly dependent on the HC.

5. *Mulder et al. model*

Mulder et al. [11] proposed a model for the human adaptive process during pursuit-tracking tasks, drawing inspiration from the Adaptive Model Theory (AMT) of Nielson. AMT is defined by Neilson et al. [24] as "*A computational theory of the information processing performed by the human nervous system in control movement*". The theory is characterized by three stages [25]: 1) Sensory analysis; 2) Response planning; 3) Response execution. Neilson et al. [24] state that the 3-stages run sequentially, in parallel and independently from each other communicating through memory buffers.

In alignment with Nielson et al.'s AMT, Mulder et al.'s model [11] is shown in Figure 2 and consists of a feedforward (FF), feedback (FB) response and internal models (N_m and H_m). The neuromuscular plus stick dynamics is given by $H_{nm}(s)$, $H_{CE}(s)$ is the CE dynamics, $N_m(s)$ and $H_m(s)$ are the internal models for the neuromuscular plus stick dynamics and the CE dynamics, respectively, $f_t(t)$ is the target function, $n(t)$ the remnant, $f_d(t)$ a disturbance signal, $u(t)$ the stick position, $m(t)$ the motor command, the innovation signal $\eta(t)$, $y(t)$ and $\dot{y}(t)$ the system output and system output rate, respectively. The Adaptive Circuity is based on both the innovation signal $\eta(t)$ and the stick position $u(t)$. The innovation signal $\eta(t)$ is the difference between the HC observation and expectation of the system output $y(t)$ or output rate $\dot{y}(t)$. The FF component includes an inverse model of the HC's internal representation of the neuromuscular and CE dynamics in series [11]: $N_m^{-1}H_m^{-1}$. The FB component works on the system error $e(t)$, such that integrator-like open loop dynamics of the crossover model are established [11]: $N_m^{-1}H_m^{-1}\omega_c e^{-j\omega\tau_e}/(j\omega)$. This integration of Nielson's theoretical framework into Mulder et al.'s model provides a comprehensive model of the human adaptive process during pursuit-tracking tasks.

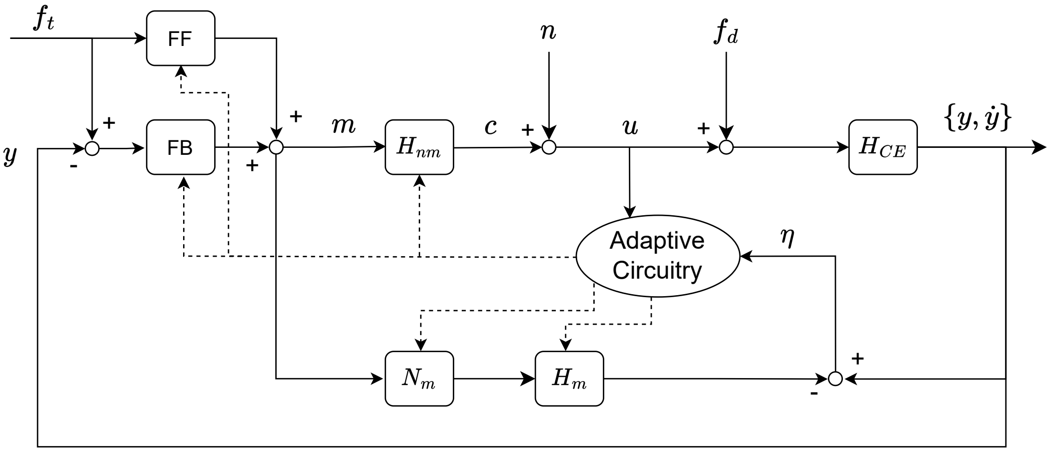

Fig. 2 Mulder et al. readjusted model based on the adaptive model theory of Nielson et al. (Mulder et al., Figure 4 [11]).

The model of Mulder et al. [11] integrates the idea of an internal model of task variables. It operates on the premise that skilled HCs notice changes in task variables when their expectation doesn't match with their observation [11]. Proficient HCs can infer the statistical characteristics of the desired signal, the disturbances impacting the system, and changes in the CE dynamics [11]. The mismatch between the observation and expectation is the innovation signal $\eta(t)$. The model shows promise for predicting the moment an HC detects a change in CE dynamics, therefore, the model is investigated further in this paper.

B. Proposed model

This section proposes a new adjusted model based on the pursuit-tracking model of Mulder et al. [14] and explains its scheme to model human detection of changes in CE dynamics. The new model is proposed to mitigate random walk behaviour of the innovation signal.

1. New model

For this paper, Figure 2 is adjusted to yield a new model omitting the feedforward response. According to Mulder et al., [14] explicit feedforward response is not necessary to add to a model for pursuit-tracking when the HC controls a single integrator-like CE dynamics as the FF acts like a pre-filter involving at least scaling of the target function $f_t(t)$. The gain for the pre-filter, when HC controls a single integrator-like CE dynamics, is according to Van der El et al. [26], approximately one. Therefore, in the new model, the feedforward response is omitted.

The HC deduces the innovation signal by observing the result of their input during pursuit-tracking tasks, restricting the model's applicability to pursuit displays. The deduction of the innovation signal relies on the HC being able to see the result of their input.

The model states that when the innovation signal $\eta(t)$ exceeds C times, where C$\in \{1, 2, 3...., 10\}$, the standard deviation of steady-state tracking $|\eta(t)| > C\sigma_\eta$ then the human operator detects a change in CE dynamics. Figure 3 shows the new model. Where $H_n(s)$ is the remnant filter, $H_p(s)$ is the HC model, $H_{nm}(s)$ the neuromuscular plus stick dynamics, $H_{CE}(s)$ the CE dynamics, $H^*_{CE}(s)$ the internal model of the CE dynamics, K the observer gain and $\eta(t)$ the innovation signal.

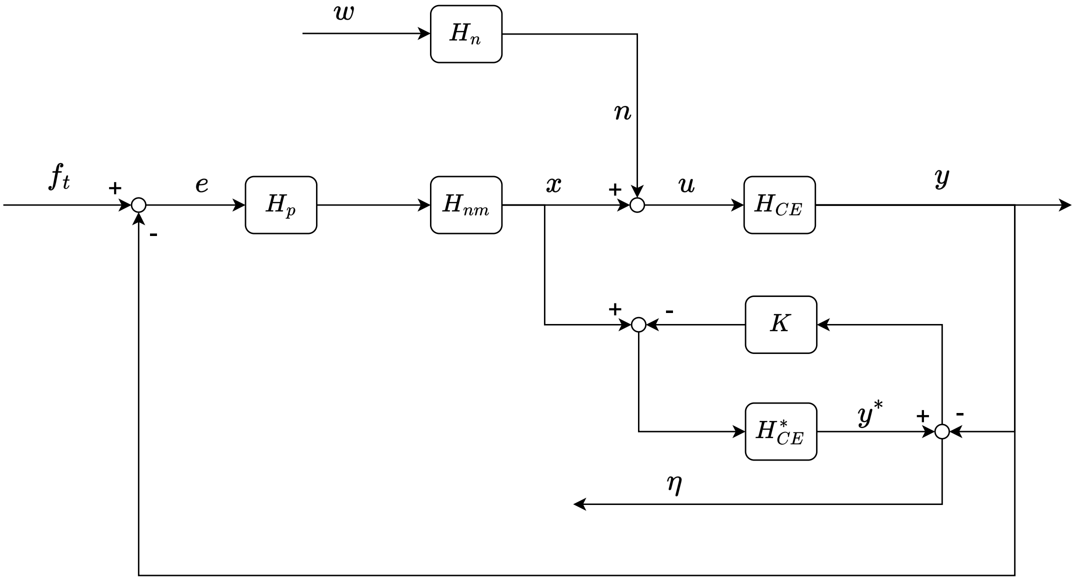

Fig. 3 Mulder et al. model adjusted, with removed FF mechanism and added observer gain K.

The analytical expression for the innovations signal $\eta(t)$ can be derived from Figure 3 and is given in the following equation:

$$\eta = \frac{H_p H_{nm}(H_{CE} - H^*_{CE})}{(1 + H_p H_{nm} H_{CE})(1 + K H^*_{CE})} F_t + \frac{H_{CE}(1 + H_p H_{nm} H^*_{CE})}{(1 + H_p H_{nm} H_{CE})(1 + K H^*_{CE})} N \tag{1}$$

Where $f_t(t)$ is the target function, $n(t)$ the remnant, $H_{CE}(s)$ the CE dynamics, $H_{nm}(s)$ the neuromucular plus stick dynamics, $H^*_{CE}(s)$ the internal model for the CE dynamics and K the observer gain. When the internal model matches the true CE dynamics, $H^*_{CE}(s) = H_{CE}(s)$, which is the case in steady-state tracking with no changes in CE dynamics, then Eq. (1) becomes the following equation, where $H_{CE}(s)$ is the CE dynamics, K the observer gain and $n(t)$ the remnant given by $H_n\omega(t)$:

$$\eta = \frac{H_{CE}}{1 + KH_{CE}} N \tag{2}$$

From Eq. (2), the analytical bounds are derived by calculating the variance of the innovation signal σ^2_η. For single integrator-like CE dynamics of the form $H_{CE}(s) = K_{CE}/(s(s+\omega_b))$, the following equation can be used to calculate the σ^2_η, with K the observer gain, K_{CE} the CE dynamics gain, K_n is the remnant filter gain, ω_b the cut-off frequency of the CE dynamics and τ_n the remnant filter time constant [27]:

$$\sigma^2_\eta = \frac{a_4 b_0^2 (a_1 a_4 - a_2 a_3)}{2 a_0 a_4 \left(a_0 a_3^2 + a_1^2 a_4 - a_1 a_2 a_3\right)} \tag{3}$$

$$\begin{array}{lcclcl}
a_0 & = & KK_{CE} & b_0 & = & K_{CE}K_n \\
a_1 & = & \omega_b + 2\tau_n KK_{CE} & b_1 & = & 0 \\
a_2 & = & 1 + 2\tau_n\omega_b + KK_{CE}\tau_n^2 & b_2 & = & 0 \\
a_3 & = & 2\tau_n + \tau_n\omega_b & b_3 & = & 0 \\
a_4 & = & \tau_n^2 & b_4 & = & 0
\end{array}$$

The model has an added observer gain K. Observer models estimate a system's present state using available measurements [28]. This estimation provides a more precise depiction of the real system state, encompassing any persisting aftereffects [28]. The observer model updates the expectation signal $y^*(t)$ with a scaled system output $Ky(t)$. Figure 4 shows the analytically calculated variance of the innovation signal for observer gains between 0.01 and 1. It can be seen that when the observer gain K approaches zero, there is asymptotic behaviour. Meaning that the analytical variance would spike to infinity when the observer gain $K = 0$. The graph of the analytically calculated variance is of the form $1/x$, as can be expected from Eq. (3).

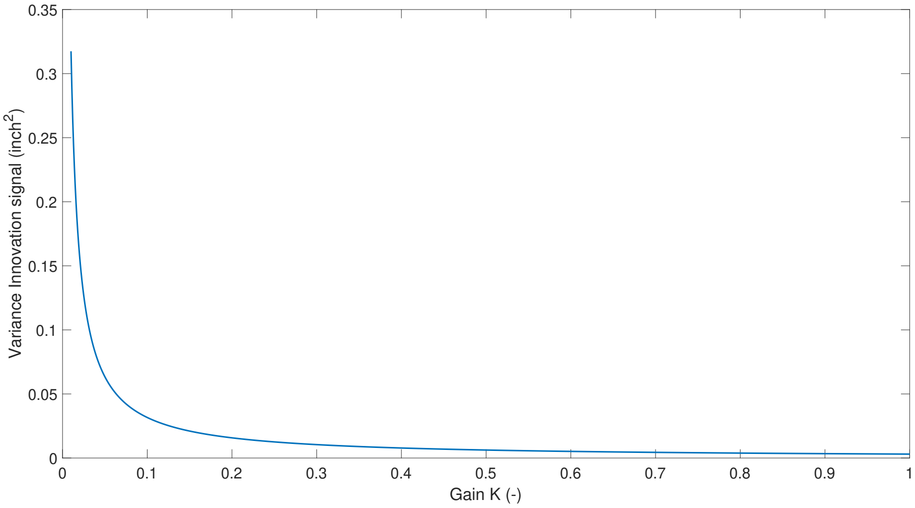

Fig. 4 Analytically calculated variance of the innovation signal σ^2_η for observer gains K from 0.01 to 1.

A very low observer gain, below 0.01, yields a very large innovation signal $\eta(t)$. Therefore, a low observer gain is not recommended, as the innovation signal will be large compared to the target signal $f_t(t)$, rms= 0.5 inch, and control input signal $u(t)$, rms= 0.84 inch, as can be seen from Table 1. As the observer gain increases, the innovation signal decreases.

An observer gain of 0.01 has a root-mean-square value of the innovation signal that is 4 and 2.5 times as small as the rms of the control and target functions, respectively. When the observer gain is large, 0.9, the rms of the innovation signal is fifteen and ten times as small as the rms of the control and target function, respectively. Therefore, an observer gain between 0.1 and 0.5 seems reasonable.

An overview of four realisations of the innovation signal $\eta(t)$ for different observer gain K is given in Figure 5. It is important to note that in the figure for the four different realisations of the innovation signal $\eta(t)$, the target functions $f_t(t)$ are the same.

Table 1 Root mean square values of the innovation signal $\eta(t)$ for different observer gain K values in inches.

rms(signal)	$K = 0.01$	$K = 0.1$	$K = 0.5$	$K = 0.9$
rms($\eta(t)$)	0.211	0.137	0.071	0.054

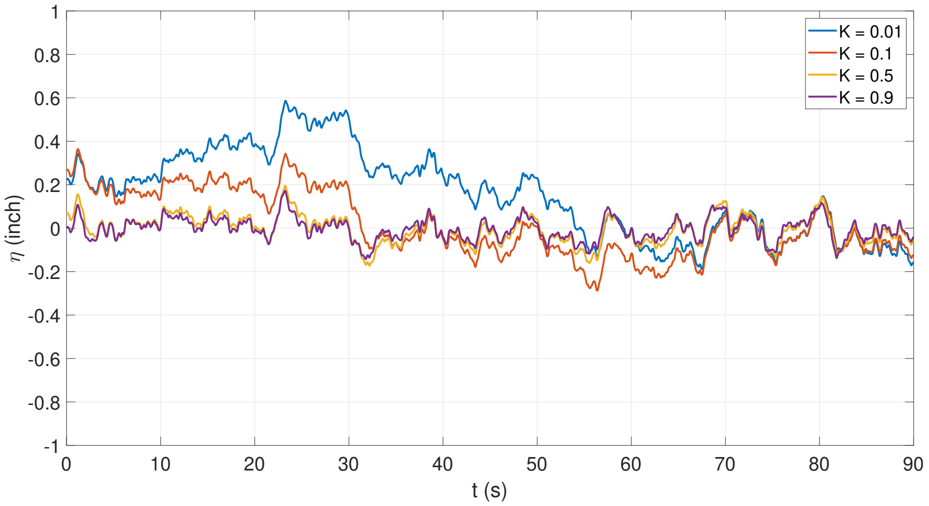

Fig. 5 Innovation signal $\eta(t)$ for different values of the observer gain K, with an HC gain of 5.5 and a remnant power ratio of 0.05. All realisations have the same target function $f_t(t)$.

Although it is mathematically calculable, an observer gain greater than one seems impractical. A gain of one implies that the innovation signal is predominantly driven by observation rather than expectation, rendering the internal model of the HC ineffective. Figure 4 illustrates that at an observer gain of one, σ_η^2 is 0.003 inch^2, approximately 0.008 centimetre^2, and tends toward zero as $K \to \infty$, albeit not reaching it. Existing literature indicates that a detection model based on the system output lacks consistency in HC detection results [9]. Therefore, observer gains greater than 0.9 are not considered.

It can be seen from Eq. (3) that, through b_0^2, the remnant filter K_n is related to the innovation signal variance σ_η^2 proportionally. A higher remnant power ratio, obtained by taking a higher remnant filter K_n value, increases the innovation signal variance σ_η^2 proportionally. From Figure 6 it can be seen that an increase in the remnant power ratio also increases the innovation signal $\eta(t)$.

2. *Detection scheme*

The model states that when the innovation signal $\eta(t)$ surpasses the steady-state threshold, $|\eta(t)| > C\sigma_\eta$, then an HC detects a change in CE dynamics. Therefore, both the constant C and the observer gain have to be determined. To make this trade-off a Receiver Operating Characteristic (ROC) curve will be constructed. A ROC curve plots the true positive

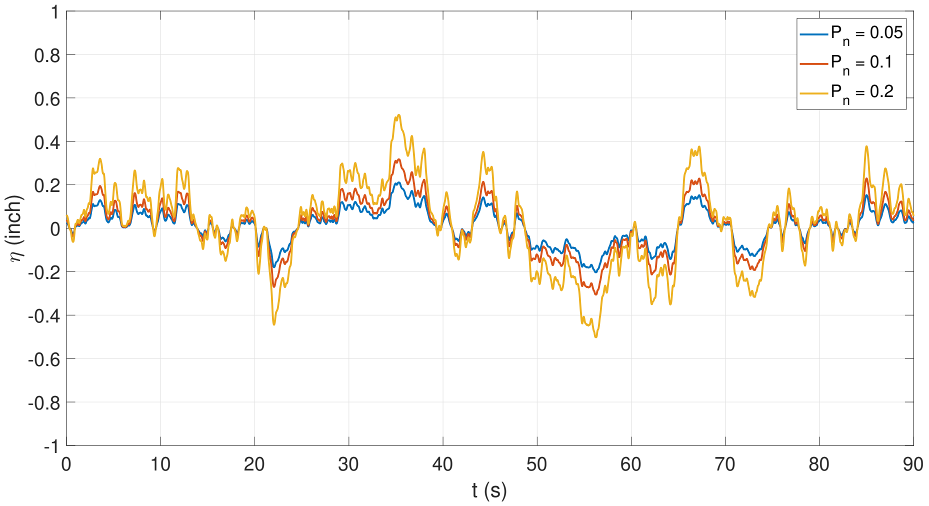

Fig. 6 Innovation signal $\eta(t)$ for different values of the remnant power ratio P_n with an HC gain of 5.5 and an observer gain of 0.5. All realisations have the same target function $f_t(t)$.

(TP) rate against the false positive (FP) rate with the TP rate given by Equation 4 and the FP rate given by Equation 5 for different values of C. With TP is a true positive, FN is a false negative, FP is a false positive and TN is a true negative.

$$\mathrm{TP}_{\mathrm{rate}} = \frac{\mathrm{TP}}{\mathrm{TP}+\mathrm{FN}} \tag{4}$$

$$\mathrm{FP}_{\mathrm{rate}} = \frac{\mathrm{FP}}{\mathrm{FP}+\mathrm{TN}} \tag{5}$$

The ROC curve is constructed based on TP and FP rates, determined when the innovation signal $\eta(t)$ surpasses a threshold defined as a constant multiple C of the standard deviations of the steady-state analytical innovation signal $|\eta(t)| > \mathrm{C}\sigma_\eta$. A TP occurs when $|\eta(t)|$ exceeds the analytical threshold after a change in CE dynamics has occurred; an FN occurs when $|\eta(t)|$ remains below the threshold after a change in CE dynamics occurred. An FP is recorded when $|\eta(t)|$ surpasses $\mathrm{C}\sigma_\eta$ before a change in CE dynamics, and a True Negative (TN) is when $|\eta(t)|$ is below the threshold before a change in CE dynamics. If $|\eta(t_c)| > \mathrm{C}\sigma_\eta$ at the time of a change in CE dynamics (t_c), a TP is only counted if the innovation signal $\eta(t)$ had already crossed the boundary before the change in CE dynamics, see Figure 7. Figures 8a-8d illustrate TP, FP, TN, and FN, respectively.

III. Method

A. Monte Carlo Analysis

This research conducted a Monte Carlo (MC) analysis to investigate if the innovation signal $\eta(t)$ could predict the moment an HC detects a change in CE dynamics. For the MC analysis, 3,000 realisations of both the target function $f_t(t)$ and remnant $n(t)$ were used. These 3,000 realisations are unique and randomly generated for the remnant. For every realisation in the MC two simulations are run with identical $f_t(t)$ and $n(t)$. One without a change in CE dynamics, to calculate the FPs and TNs and one with a change in CE dynamics, for the TPs and FNs.

The change in CE dynamics was set at 95 seconds, five seconds before the simulation's end (with a ten-second run-in time). This choice is informed by experimental data, showing that in pursuit-tracking tasks, most human controllers (HCs) exhibit a detection lag of 0.6-5 seconds [9]. Similarly, experiments on compensatory displays indicate that trained HCs typically detect changes in CE dynamics within three seconds [1, 16]. Therefore, a five-second time window for detection is considered sufficient.

The MC is run for both an HC with a low $\omega_c = 2.6$ rad/s and with a high $\omega_c = 4$ rad/s crossover frequency. This is done to better understand the influence of the HC gain K_p on the innovation signal $\eta(t)$. An HC with a lower ω_c would

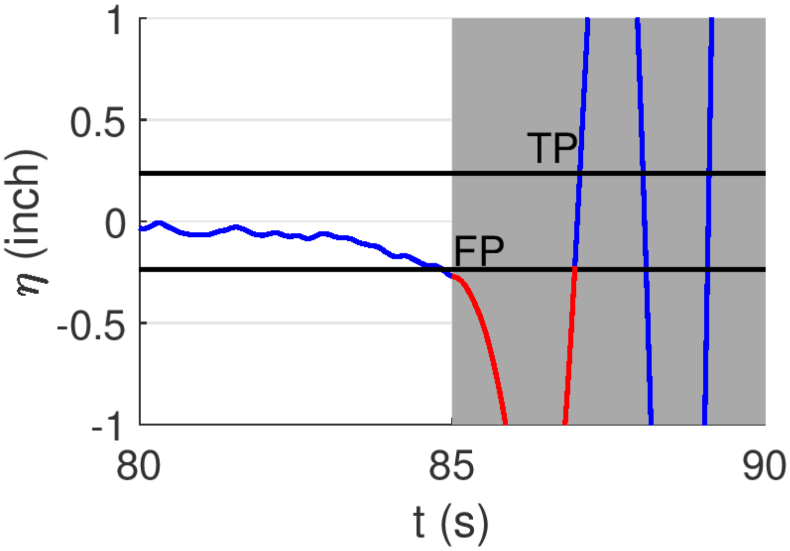

Fig. 7 Visual representation of the innovation signal $\eta(t)$, exceeding the $3\sigma_\eta$ bounds resulting in a false positive after 85 seconds and a true positive after 87 seconds, the grey area is the post-transition dynamics. With an HC gain of 5.5, an K of 0.5 and a P_n 0f of 0.05.

control with a lower HC gain K_n than an HC with a larger crossover frequency. The HC does not adapt within five seconds and their internal model does not change. So the HC model $H_p(s)$ and internal model of the CE dynamics $H^*_{CE}(s)$ do not change throughout the simulation. The decision to keep the HC constant is intentional, as this research specifically concentrates on the HC's detection of a change in CE dynamics rather than the adaptive process itself. The HC is characterized as an ideal HC with no variations in gain or time delay throughout the simulation.

An HC with a higher crossover frequency exhibits more aggressive control compared to an HC with a lower ω_c. Consequently, the control input signal amplitude of the HC with a higher ω_c is larger than that of the HC with a lower ω_c. To maintain a constant remnant power ratio for both HCs, the remnant gain K_n of the HC with higher ω_c needs to be larger. As the remnant gain increases, so does the σ^2_η leading to larger theoretical thresholds. The HC with higher ω_c will have faster detection of the change in CE dynamics due to the larger control input signal amplitude. However, there will also be more FPs due to the larger innovation signal $\eta(t)$.

The observer gain K is varied from 0.01 to 0.9. This is done because an observer gain of zero would lead to a random walk and the analytical variance could not be calculated. The observer gain stays below one otherwise it would negate the use of the internal model. Then, the innovation signal $\eta(t)$ would only be driven by the observation of the system output $y(t)$ and not the expectation anymore.

When the observer gain K decreases, the innovation signal $\eta(t)$ exhibits behaviour closer to a random walk. This behaviour leads to a significant increase in variance, as illustrated in Figure 4. While a lower observer gain diminishes false positives, it also reduces true positives. Consequently, the innovation signal becomes less accurate in detecting changes in CE dynamics, even with larger thresholds. The σ^2_η will be larger for the lower values of K. For lower values of the observer gain, K<0.1, the transfer function $H_{CE}/(1 + KH_{CE})$ becomes more equal to H_{CE}, amplifying the lower frequencies.

The MC is repeated for different values of remnant power ratios namely 0.05, 0.1 and 0.2. From literature [8, 29], it can be seen that the average remnant power ratios from experimental data are around 0.15. The range or remnant power ratios will help with a better understanding of the influence of P_n on the innovation signal $\eta(t)$ to predict when an HC detects a change in CE dynamics.

As can be seen from Equation 2, when the internal model $H^*_{CE}(s)$ matches the actual CE dynamics $H_{CE}(s)$, the innovation signal $\eta(t)$ is entirely defined by the remnant $n(t)$, the CE dynamics $H_{CE}(s)$ and the observer gain K. Hence, the remnant power ratio directly influences the innovation signal $\eta(t)$. A higher remnant power ratio of 0.2 compared to

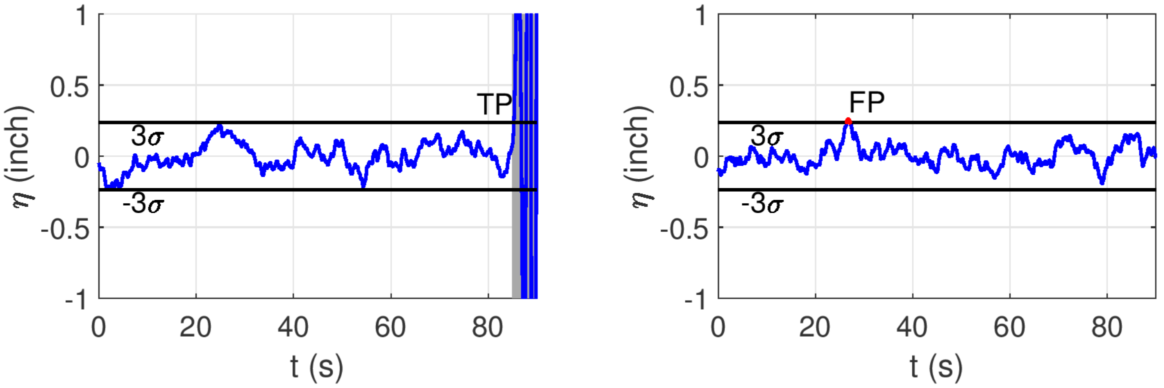

(a) Visual representation of the innovation signal exceeding $3\sigma_\eta$ at $t = 86$ after a change in CE dynamics at 85 seconds, resulting in a TP, the grey area is the post-transition dynamics.

(b) Visual representation of the innovation signal exceeding $3\sigma_\eta$ at $t = 26$ where no change in CE dynamics is simulated, resulting in an FP.

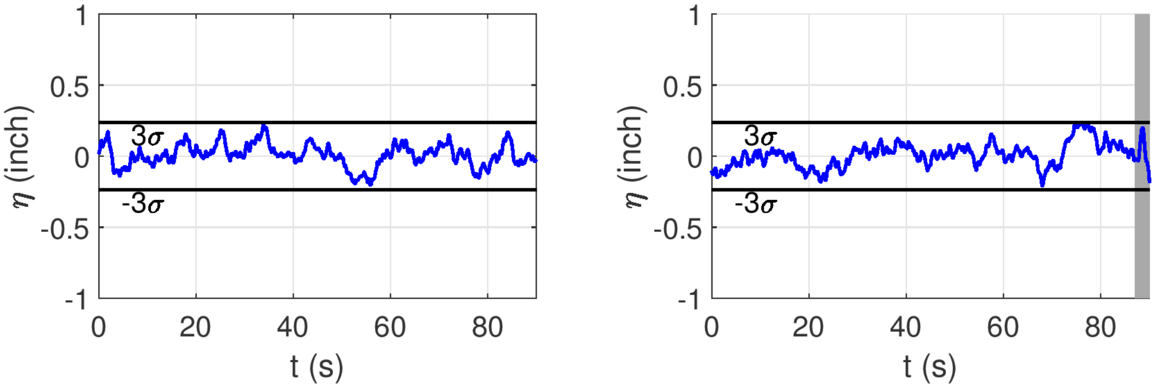

(c) Visual representation of the innovation signal not exceeding $3\sigma_\eta$ where no change in CE dynamics is simulated, resulting in a TN.

(d) Visual representation of the innovation signal not exceeding $3\sigma_\eta$ after a change in CE dynamics at 87 seconds, resulting in an FN, the grey area is the post-transition dynamics.

Fig. 8 Visual representation of the innovation signal to result in a TP, FP, TN and FN. With an HC gain of 5.5, an K of 0.5 and a P_n 0f 0.05.

0.05 results in a larger, ≈ 60% greater, variance in the innovation signal σ_η^2 for the same observer gain $K = 0.5$. As the remnant power ratio increases, the variance of the remnant, σ_n^2, increases compared to the variance of the control input signal, σ_u^2, as $P_n = \sigma_n^2/\sigma_u^2$. This increase in the remnant power ratio implies an increased remnant filter gain K_n, which is directly proportional to the variance of the innovation signal, σ_η^2.

The larger the remnant power ratio the slower the detection will be. The number of TPs and FPs will also be lower. This is because after the change in CE dynamics, $\eta(t)$ is given by part the target function $f_t(t)$ and part remnant $n(t)$, Eq. (1). When the remnant is larger, bigger P_n, the relative influence of the target function is smaller on $\eta(t)$ than for lower remnant power ratios. The target function part of $\eta(t)$ after the change in CE dynamics is independent of the remnant filter. So the relative impact of the target function on the innovation signal after the change in CE dynamics will be smaller for larger remnant power ratios.

Cresting the target function $f_t(t)$ serves to mitigate extreme fluctuations in the innovation signal following a change in CE dynamics. This becomes crucial because, during a change in CE, the innovation signal is influenced not only by the remnant but also by the target function. Substantial fluctuations in the target function $f_t(t)$ correspondingly lead to an increase in the control input signal $u(t)$. As $P_n = \sigma_n^2/\sigma_u^2$, an increase in the variance of the control input signal $u(t)$ necessitates an increase in the variance of the remnant to maintain the same remnant power ratio. This, in turn, raises the remnant gain K_n, resulting in an increased variance of the innovation signal. Therefore, a higher remnant power ratio amplifies the influence of the remnant on the innovation signal, leading to a larger variance. This, in turn, diminishes the impact of the target function $f_t(t)$ on the innovation signal $\eta(t)$ during a change in CE dynamics.

Then for the different multiples, C$\in \{1, 2, 3..., 10\}$, of the $\sigma_{\eta(t)}$, the true and false positive rates were determined. The range is chosen to better understand how the detection of changes in CE dynamics by HC with the innovation signal $\eta(t)$ is influenced by the detection thresholds. The detection threshold also plays an important role in the average detection time. A larger threshold would mean a longer detection time and a probable decrease in FP but too large of a threshold will also decrease the amount of TPs. Therefore, there is an optimal C for every K.

The simulation with a change in CE dynamics at 95 seconds went from a single integrator-like to a double integrator-like CE dynamics. To create a change in CE dynamics a sigmoid activation function is used, given in Equation 6. Where P_1 is the initial parameter value, P_2 is the final parameter value, τ is the time of maximum rate of change and G is the maximum rate of change. The sigmoid activation function is used elsewhere to introduce a change in CE dynamics [2, 9, 23]. The sigmoid activation function can represent a step input when G the maximum rate of change is very big, ≥ 10. In this research, the maximum rate of change was set to 100 s^{-1} meaning the sigmoid changes from its starting value to the final value in about 0.1 seconds. This value was chosen based on research from Barragan [9] on changes in CE dynamics for pursuit-tracking tasks.

$$P(t) = P_1 + \frac{P_2 - P_1}{1 + e^{-G(t-\tau)}} \tag{6}$$

B. Pursuit HC model

The HC was modelled based on the simplified precision model for compensatory tracking from McRuer et al. [10] plus the neuromuscular and stick dynamics from van Paassen et al. [30]. From literature [26, 31, 32] it can be seen that when an HC controls a single integrator-like CE dynamics for a pursuit-tracking task then the extended simplified precision model would be a good model.

The values in Table 2 are used for the simulations, the HC model and neuromuscular dynamics do not change during the simulations even when there is a change in CE dynamics. It can be seen that the HC controls with no lead, causing the simulation to become unstable after the change in CE dynamics. The values are taken from Barragan [9]. The full HC model is given by the following equation, where K_p is the HC gain, T_L is the HC's lead constant, T_I is the HC's lag constant, τ_e is the HC's effective time delay, ω_{nm} is the natural frequency and ζ_{nm} the damping ratio of the system [26]:

$$H_{HC} = K_p \frac{1 + T_L j\omega}{1 + T_I j\omega} \frac{\omega_{nm}^2}{\omega_{nm}^2 + 2\zeta_{nm}\omega_{nm}s + s^2} e^{-j\omega\tau_e} \tag{7}$$

Table 2 HC model values used during the simulations.

HC	K_p (-)	ω_c (rad/s)	ϕ_m (deg)	T_L (s)	T_I (s)	τ_e (s)	ω_{nm} (rad/s)	ζ_{nm} (-)
$\omega_{c_{low}}$	3.5	2.6	55.1	0	0	0.09	15	0.7
$\omega_{c_{high}}$	5.5	4	35.6	0	0	0.09	15	0.7

C. Controlled Element Dynamics

The CE dynamics are single integrator-like during pre-transition tracking and double integrator-like post-transition. The reason for going from single integrator-like to double integrator-like in the simulation is to be able to use the aforementioned HC model and to mimic one of the experimental conditions from Barragan for pursuit-tracking with changes in CE dynamics [9]. The following equation is the time-varying transfer function of the CE dynamics, with $K_{CE}(t)$ the time-varying CE gain and $\omega_b(t)$ the time-varying break frequency [2, 9, 23].

$$H_{CE}(s,t) = \frac{K_{CE}(t)}{s(s + \omega_b(t))} \tag{8}$$

The CE dynamics start as single integrator-like by having a high break frequency, this causes the CE dynamics to approximate a single integrator around the open loop crossover frequency, 1-5 rad/s. Then the sigmoid activation function is used at $t = 95$ seconds to make the CE dynamics double integrator-like. This is achieved by reducing the gain of the CE dynamics and lowering the break frequency, without HC adaptation.

Table 3 CE dynamics model values used during the simulations.

Dynamics	K_c (-)	ω_b (rad/s)
Pre-transition	15	20
Post-transition	2	0.2

D. Target Function

The target function is a quasi-random signal given by a sum of sinusoids in Equation 9. Where $A_t[n]$ is the amplitude, $\omega_t[n]$ the frequency and $\phi_t[n]$ the phase of the sinusoid of the n^{th} sinusoid. N is the number of sinusoids, chosen to be 10 for this research.

$$f_t(t) = \sum_{n=1}^{N} A_t[n]\sin(\omega_t[n]t + \phi_t[n]) \tag{9}$$

The target function $f_t(t)$ is crested for the MC analysis. Signals with high crest factors have large peaks compared to their average value, while signals with low crest factors have smaller variations between their peaks and average values. The target functions are crested to make sure no large or small variations are present in the MC analysis. Equation 10 is used to find the crest factor of the target function. Then 10,000 target functions were created and the 3,000 closest to the mean crest factor of 2.6 were chosen to be used in the MC analysis. The crest factor is calculated by taking the maximum of the absolute values of the target function $f_t(t)$ and dividing it by the root mean square.

$$\text{CF} = \frac{\max(|f_t(t)|)}{\text{rms}(f_t(t))} \tag{10}$$

To avoid spectral leakage, the fundamental frequency of the target function has to be $\omega_m = 2\pi/T_m$, with T_m being the measurement time. For this research, a measurement time of 90 seconds was taken, which means the fundamental frequency is $\omega_m \approx 0.0698$ rad/s. The frequency of the n^{th} sinusoid is calculated by multiplying the fundamental frequency with a prime number k_n, so $\omega_t[n] = k_n\omega_m$.

Table 4 Target function parameters with an example of phase shifts which would result in a crested target function.

n (-)	k_n (-)	ω_t (rad/s)	ϕ_t (rad)	A_t (inch)
1	3	0.209	5.323	0.286
2	5	0.349	5.496	0.286
3	9	0.628	5.151	0.286
4	11	0.768	2.469	0.286
5	17	1.187	1.343	0.286
6	27	1.885	0.888	0.286
7	43	3.002	2.514	0.029
8	71	4.957	3.969	0.029
9	131	9.146	1.365	0.029
10	233	16.267	3.894	0.029

To avoid significantly large sudden peaks in the function, the target function $f_t(t)$ was carefully designed. This involved generating 10,000 realizations of the target function $f_t(t)$ and calculating the crest factor for each one. The mean crest factor was then determined based on these 10,000 values. Subsequently, the target functions were compiled into a list and sorted based on their crest factors. From this sorted list, 1,499 target functions with crest factors below the mean were selected, along with 1,500 target functions above the mean crest factor. Additionally, the target function with the mean crest factor was included, resulting in a total of 3,000 carefully crafted target functions. This selection process ensured that the generated functions maintained stability without exhibiting excessively large sudden peaks.

E. Remnant

The remnant $n(t)$ reflects the non-linear part of the HC [10]. It is modelled as filtered zero-mean Gaussian white noise [8]. Which was randomly generated for every realisation of the MC analysis. So 3,000 unique remnant realisations were created. The remnant filter is a second-order filter for the single integrator-like CE dynamics given in the following equation, with K_n the remnant filter gain and τ_n the remnant filter time constant [8, 9]:

$$H_n(s) = \frac{K_n}{(1+\tau_n s)^2} \tag{11}$$

The remnant power ratio P_n, remains consistent across all 3,000 realizations in the MC simulation. This is achieved by adjusting the remnant gain individually for each realization. This is important to keep the influence of the remnant on the innovation signal $\eta(t)$ constant for every realisation of the MC. The Eq. (12) adjusts the remnant gain K_n for every realisation to keep it within ±1% of the remnant power ratio setting, P_n is 0.05 or 0.1 or 0.2, with σ_n^2 the variance of the remnant and σ_u^2 the variance of the HC control input.

$$P_n = \frac{\sigma_n^2}{\sigma_u^2} \tag{12}$$

F. Independent variables MC

The MC is run for three different remnant settings, twelve different observer gains, and two different HC gains. For a total of 72 MC runs, each having 3,000 realisations. For every realisation the TP and FP were calculated for the different multiples C, as the threshold is defined as Cσ_η, to come up with a TP and FP rate per observer gain. Then ROC curves were constructed per remnant power ratio and HC gain for a total of six different curves. So the remnant power ratios were run per HC gain. The following table has all the different settings for the MC analysis.

Table 5 MC settings for the different HC gain K_p, remnant power ratio P_n Observer gain K and multiples of the threshold C.

K_p (-)	P_n (-)	K (-)	C (-)
3.5	0.05	{0.01 0.025 0.05 0.1 0.2 0.3 0.4 0.5 0.6 0.7 0.8 0.9}	1-10
	0.1	{0.01 0.025 0.05 0.1 0.2 0.3 0.4 0.5 0.6 0.7 0.8 0.9}	1-10
	0.2	{0.01 0.025 0.05 0.1 0.2 0.3 0.4 0.5 0.6 0.7 0.8 0.9}	1-10
5.5	0.05	{0.01 0.025 0.05 0.1 0.2 0.3 0.4 0.5 0.6 0.7 0.8 0.9}	1-10
	0.1	{0.01 0.025 0.05 0.1 0.2 0.3 0.4 0.5 0.6 0.7 0.8 0.9}	1-10
	0.2	{0.01 0.025 0.05 0.1 0.2 0.3 0.4 0.5 0.6 0.7 0.8 0.9}	1-10

IV. Results

A. Effect of HC gain

Figures 9a-9f show the ROC curves for the innovation signal exceeding $C\sigma_\eta$. The y-axis shows the TP rate, based on 3,000 realisations and the x-axis shows the FP rate.

From the figures, it can be seen that the TP and FP rates for the HCs with a low and high crossover frequency are not significantly different for high observer gains $K > 0.5$, with C>3 and $P_n = 0.05$, the TP rate is 1 and the FP rate is zero for both HCs.

Small differences ±1% start occurring at higher remnant values, $P_n = 0.2$. The HC with higher crossover frequency has a 0.3% lower TP rate. These differences are so marginal that when the amount of MC realisations would be increased the difference would slowly decrease. The lower observer gain $K < 0.5$ has around 1% smaller TP rate and around a 0.9% smaller FP rate. These differences will also be decreased with increased MC realisations. So even though small variations in the TP and FP rates for the HC with low and high crossover frequency are found, it is hard to see the full effect K_p has on the detection of changes in CE dynamics with the innovation signal for different C.

B. Effects of the observer gain

From Figures 9a-9f, it becomes clear that a lower observer gain results in fewer TPs and FPs for every C. For lower observer gains in the range of 0.01-0.1, the variance of the innovation signal σ_η^2 increases, causing a larger innovation signal $\eta(t)$ and more low-frequency behaviour.

The slower movement of the innovation signal through the threshold results in a decrease in FPs compared to larger observer gain values (0.5-0.9) for C<2. Although the actual TP rate for C=2 is larger for higher observer gains, the FP rate is also higher. When C>2 the number of TPs and FPs for the lower observer gain decreases, due to the slow behaviour of the innovation signal $\eta(t)$, as low K values result in low-pass behaviour.

Higher observer gain values result in more FPs per realisation (90 seconds) compared to lower observer gains for every C. However, only one false positive per realisation is counted, meaning that the increased false positives per realisation do not impact the ROC curve. The higher frequency behaviour causes more FPs per realisation but also a higher TP rate after the change in CE dynamics.

C. Effects of C

From Figures 9a-9f it can be seen that the choice of the value for C impacts the TP and FP rates. The lower the value, C≤2, the more FPs there are. It also causes an increase in TP rate, resulting in almost always a detection, for any observer gain, see Table 6. The high FP rate means that the lower values of C are not desired for the detection of changes in CE dynamics. The higher bounds C>4 cause very few FPs but also very few TPs as can be seen for the lower observer gain. From the table, it can also be seen that for lower observer gains, K<0.1 the value of C has to be lower 2 ≥C≤ 3. For the K around 0.1 C values between three and four are preferable. For the higher values of K of 0.9, the C values of between four and five are preferable. The choice of the value for C is influenced by the observer gain.

Table 6 TP and FP rate for different values of C, with $K_p = 5.5$, $P_n = 0.2$ and for observer gains 0.01, 0.1, 0.5 and 0.9

K (-)		C=1	C=2	C=3	C=4	C=5	C=6
0.01	TP rate	0.997	0.950	0.885	0.803	0.706	0.489
	FP rate	0.497	0.008	0	0	0	0
0.1	TP rate	0.998	0.999	0.992	0.984	0.970	0.936
	FP rate	1	0.552	0.035	0	0	0
0.5	TP rate	1	1	1	1	1	0.999
	FP rate	1	0.988	0.265	0.006	0	0
0.9	TP rate	1	1	1	1	0.999	0.996
	FP rate	1	0.999	0.397	0.015	0	0

D. Effects of the Remnant power ratio

As can be seen from Figures 9a-9f the increase in remnant power ratio decreases the number of TPs and increases the number of FPs. Resulting in a lower TP and a higher FP rate for all the different observer gain values. At the larger observer gain values $K > 0.5$ the differences between the low 0.05, medium 0.1 and high 0.2 remnant power ratio are not significant as all observer gains have a TP rate of approximately one. It can also be seen that the multiples of the bounds C have a higher TP and lower FP rate for lower remnant power ratios. For the lower values of $K < 0.5$ the increase in P_n decreases the number of TPs and FPs as the relative effect of the target function on the innovation signal is smaller post-transition. The decrease in FPs is due to the larger analytical bounds σ_η.

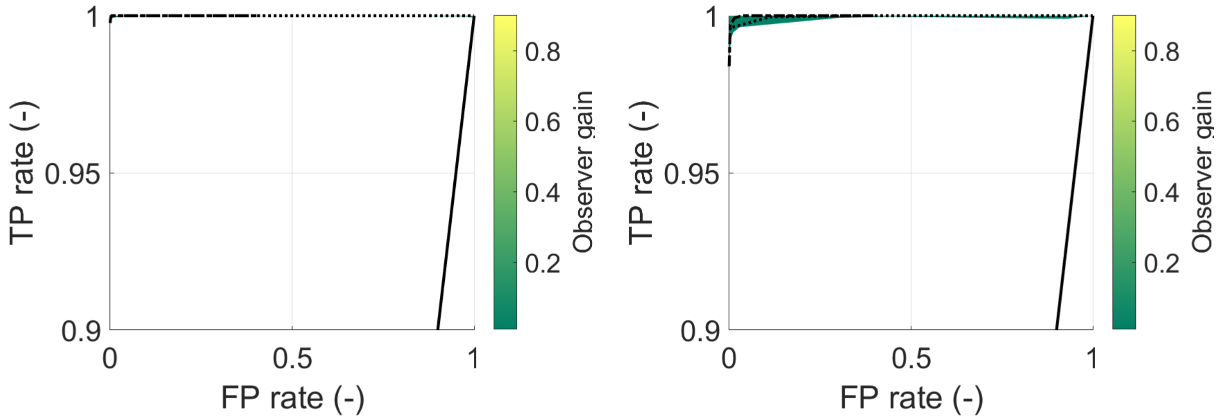

(a) ROC curve for an HC with a ω_c = 2.6 rad/s and P_n = 0.05. **(b) ROC curve for an HC with a ω_c = 4 rad/s and P_n = 0.05.**

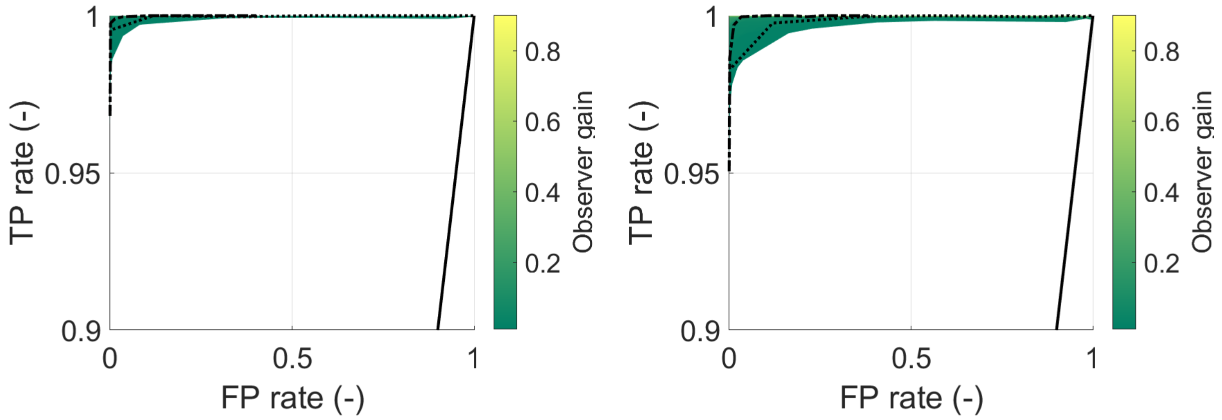

(c) ROC curve for an HC with a ω_c = 2.6 rad/s and P_n = 0.1. **(d) ROC curve for an HC with a ω_c = 4 rad/s and P_n = 0.1.**

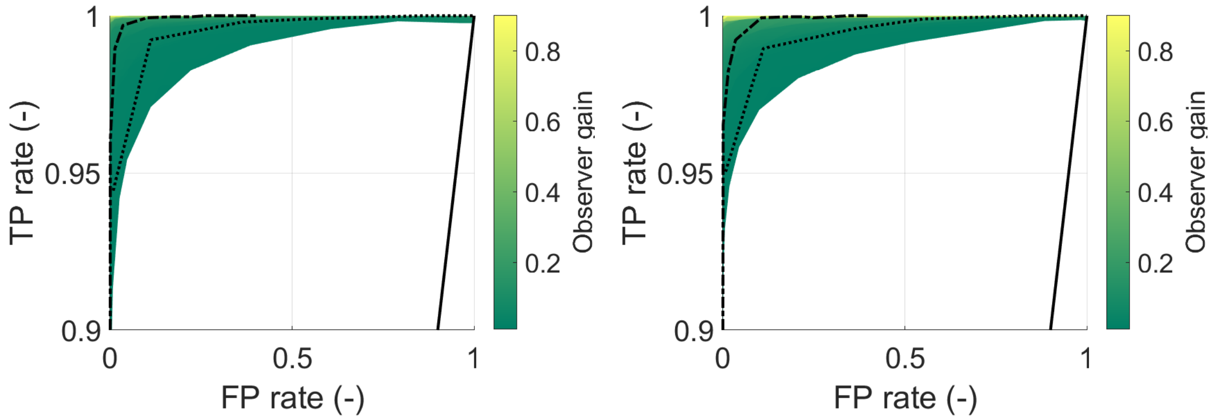

(e) ROC curve for an HC with a ω_c = 2.6 rad/s and P_n = 0.2. **(f) ROC curve for an HC with a ω_c = 4 rad/s and P_n = 0.2.**

Fig. 9 ROC curves with the TP against the FP rate, for $C\sigma_\eta$, with C from 1 to 10, calculated with 3,000 target and remnant realisations for various remnant power ratios P_n and observer gain K from 0.01-0.9. With the dash dotted line $3\sigma_\eta$ and the dotted line $2\sigma_\eta$. Note the y-axis is from 0.9 to 1.

E. Average detection times

Figures 10a-10f illustrate the average detection times for various observer values, 0.01 to 0.9, across different thresholds $C\sigma_\eta$, with the fastest, average and slowest detection times from the experiment from Barragan [9]. The detection time is the first instance when the innovation signal $\eta(t)$ crosses the boundary. The average detection time was calculated from 3,000 realizations with a change in CE dynamics.

From the results, it becomes evident that the detection time decreases with increasing observer gain, increases with smaller observer gain and increases with a higher value of C. For the smaller values of K, smaller than 0.1, the detection time increases almost linearly with a larger value of C. For the larger values of K≥0.5 the detection time between one and two σ_η first decreases and then increases linearly but less fast than for the lower K. The reason for the initial decrease is due to the calculation of the detection time. If the threshold is already exceeded before the change in CE dynamics then the detection is only counted when the innovation signal $\eta(t)$ is bounded and then unbounded again. So for C=1, the change of an FP right before detection with K≥0.5 is quite large. Therefore, detection can take longer as the innovation signal first needs to fall below C=1 to be counted as a detection.

For the lower remnant ratio, 0.05 the detection is faster than for a higher remnant power ratio, 0.2. It can also be seen that the detection times increase more quickly for higher remnant power ratios, with increasing values of C than for the lower remnant power ratios. The HC with higher ω_c has a shorter detection time than the HC with a larger crossover frequency. This is because of the larger control input signal for the HC with higher ω_c.

Table 7 is constructed using the ROC curves by looking at the value of C that results in the lowest FP and largest TP rate for K is 0.01, 0.1, 0.5 and 0.9 for both the HCs and P_n is 0.05, 0.1 and 0.2. Where C is between 2-3 for K=0.01, 3-4 for K=0.1 and 4-5 for K=0.9.

Table 7 Average detection times for different K_p, P_n and K, for two different values of C.

K_p	P_n	K (-)	Average detection time (s)
3.5	0.05	0.01	1.69-2.24
		0.1	1.09-1.30
		0.5	0.91-0.99
		0.9	0.76-0.86
	0.1	0.01	2.18-2.99
		0.1	1.33-1.60
		0.5	1.06-1.22
		0.9	0.92-1.05
	0.2	0.01	2.94-3.84
		0.1	1.73-2.11
		0.5	1.32-1.54
		0.9	1.16-1.32
5.5	0.05	0.01	1.66-2.26
		0.1	1.06-1.27
		0.5	0.83-0.94
		0.9	0.73-0.85
	0.1	0.01	2.21-3.00
		0.1	1.31-1.60
		0.5	1.01-1.15
		0.9	0.88-1.01
	0.2	0.01	2.95-3.61
		0.1	1.73-2.17
		0.5	1.30-1.51
		0.9	1.09-1.28

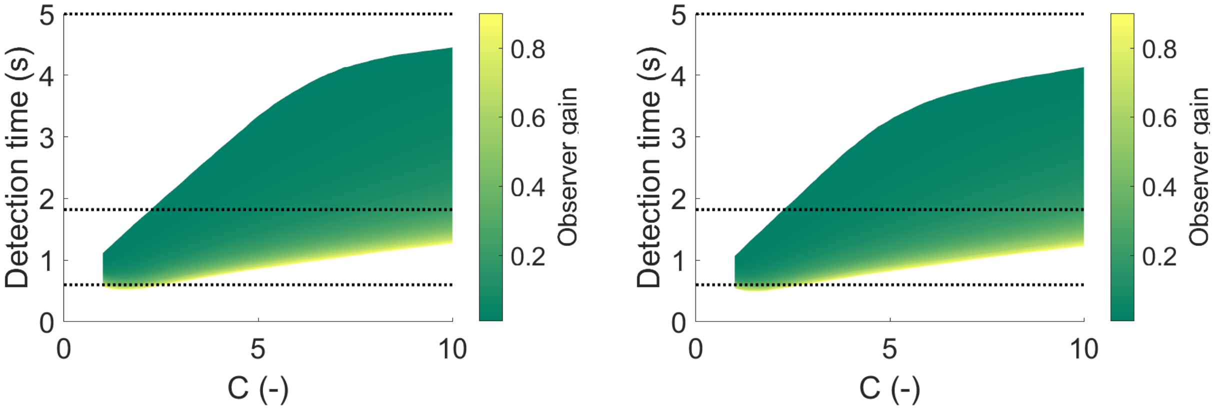

(a) **Average detection times against C for an HC with a** $\omega_c = 2.6$ **rad/s, a** $P_n = 0.05$.

(b) **Average detection times against C for an HC with a** $\omega_c = 4$ **rad/s, a** $P_n = 0.05$.

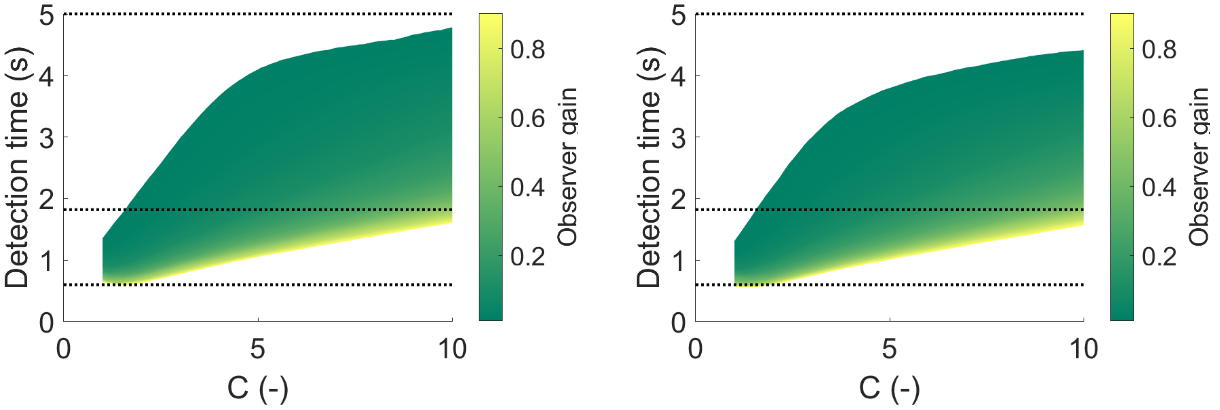

(c) **Average detection times against C for an HC with a** $\omega_c = 2.6$ **rad/s, a** $P_n = 0.1$.

(d) **Average detection times against C for an HC with a** $\omega_c = 4$ **rad/s, a** $P_n = 0.1$.

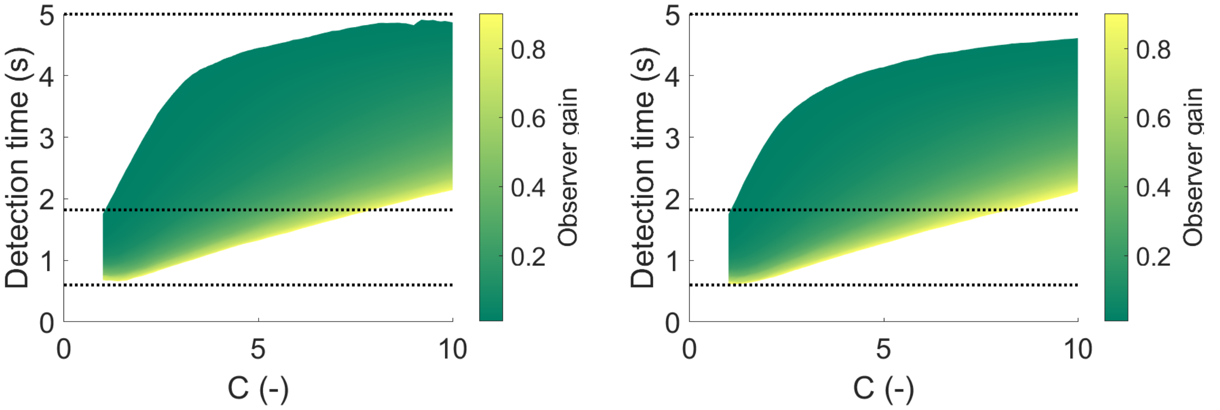

(e) **Average detection times against C for an HC with a** $\omega_c = 2.6$ **rad/s, a** $P_n = 0.2$.

(f) **Average detection times against C for an HC with a** $\omega_c = 4$ **rad/s, a** $P_n = 0.2$.

Fig. 10 Average detection time against $C\sigma_\eta$**, with C from 1 to 10 for various remnant power ratios** P_n **and observer gain** K **from 0.01-0.9. With the fastest, average and slowest detection from the experiment data from Barragan [9] indicated.**

From Table 7 it can be seen that the average detection time varies for the HC gain K_p. The higher K_p decreases the detection time because the control signal has a larger amplitude than for a smaller K_p. The remnant power ratio increases the detection time due to a reduced influence of the target function on the post-transition innovation signal $\eta(t)$. The lower observer gains cause a slower detection due to the low-frequency behaviour of the innovation signal $\eta(t)$ with $K < 0.1$.

From Table 7 it can be seen that the detection window, the lower and upper limit of the average detection time, is also much shorter for higher observer gains, $K = 0.9$ compared to the lower $K = 0.01$. For $K = 0.9$ the detection window is 0.1 seconds for the lower remnant ratio of 0.05 and 0.2 seconds for $P_n = 0.2$, while for $K = 0.01$, the detection window is 0.5 and 0.9 seconds, respectively.

It is important to note that the provided detection time does not incorporate any human computation delays or human reaction time.

V. Discussion

The goal of this research was to better understand if the new model, using an observer model and the innovation signal $\eta(t)$, could be used to determine the moment an HC detects a change in CE dynamics in pursuit-tracking tasks. An MC analysis was performed for two different K_p, three P_n, twelve K and ten C.

The HC with a higher ω_c controls with a higher gain K_p, meaning they control more aggressively. The variance of the control signal σ_u^2 is thus bigger than for an HC with a lower crossover frequency. The bigger variance increases the remnant filter gain because the remnant power ratio is kept at a constant level. This increase in remnant filter gain then causes the variance of the innovation signal σ_η^2 to be larger as it is proportionally related to the remnant filter gain $\sigma_\eta^2 \propto K_n^2$. So the σ_η for an HC with higher ω_c, is larger than for the HC with lower ω_c. The more aggressive control causes more true positives but also more false positives.

Barragan's experiment [9] on changes in CE dynamics for pursuit-tracking reveals that there is no significant difference in detection times between human controllers with lower crossover frequencies and those with higher crossover frequencies. This would imply that when a change in CE dynamics happens from SI to DI both the HCs can detect the change in CE dynamics at roughly the same time. The difference in detection time between the HCs is not significant. So it seems that the crossover frequency of the HC does not significantly impact the detection of changes in CE dynamics when using the innovation signal. When looking at the average detection times this can also be seen; however, the detection is a bit slower for every C. This seems in line with the research from Barragan [9]. For both HCs the same C values can be used, however, this will result in slightly slower detection of changes in CE dynamics using the innovation signal. The HC with a lower ω_c might have slightly lower FPs but no significant correlation was found.

The remnant power ratio significantly influences the innovation signal $\eta(t)$. The innovation signal $\eta(t)$ is primarily driven by the remnant $n(t)$ when the internal model of the CE dynamics matches the actual CE dynamics. According to [10, 33], the remnant models the quasi-linear part of the HC, with sources for the remnant in descending order: time-varying control behaviour, pure noise injection (e.g., perception and motor variability), and nonlinear control behaviour. An increase in the remnant power ratio implies changes in the HC's control behaviour or increased pure noise injection, such as motor variability or more nonlinear behaviour.

The variance of the innovation signal σ_η^2 is directly and quadratically related to the remnant filter gain $\sigma_\eta^2 \propto K_n^2$. Therefore, an increase in remnant power ratio, and consequently the remnant filter gain, results in the squared variance of the innovation signal σ_η^2 assuming constant remnant filter time-constant, CE dynamics, and observer gain. This increased variance causes higher thresholds for detecting changes in CE dynamics. The innovation signal must be significantly large to surpass these thresholds, and when a change in CE dynamics occurs, the innovation signal is influenced by both the target function $f_t(t)$ and the remnant $n(t)$. Before the change in CE dynamics, the innovation signal $\eta(t)$ was entirely given by the remnant $n(t)$.

The change in CE dynamics introduces the target function, see Eq. (1) to the innovation signal and the part of the remnant of the innovation signal scales with $\propto H_{CE}^*(s)/H_{CE}(s)$ compared to steady-state tracking. If the variance of the innovation signal σ_η^2 is small during steady-state tracking (indicating low remnant power ratio), the influence of the target function $f_t(t)$ on the innovation signal is greater when a change in CE dynamics occurs. Consequently, the innovation signal exceeds the thresholds more quickly, as evidenced by the lower true positive rate for higher remnant power ratio values.

The increased P_n leads to a slower detection of the change in CE dynamics, as the detection threshold must be raised to avoid many false positives. An HC with a high remnant power ratio, such as a tired or inattentive HC, would logically experience an increase in false positives and detection time. The fact that the number of false negatives increases aligns with expectations, indicating that the HC may not detect the change in CE dynamics, possibly due to distraction or fatigue introducing more remnant into their control behaviour.

The detection threshold must be set to minimize false positives during steady-state pre-transition tracking. Research into both compensatory [18] and Pursuit-tracking [9] experiments revealed that most HCs detect changes in CE dynamics when, for compensatory-tracking, the system error rate $\dot{e}(t)$ exceeds $3.9\sigma_{\dot{e}}$, and for pursuit-tracking, $\ddot{y}(t)$ exceeds 3.6-$4\sigma_{\ddot{y}}$ of the steady-state tracking. This suggests that HCs typically employ a relatively high threshold for detection. From the MC, it was found that the value of C needs to be adjusted for every observer gain K. For $0.01 < K < 0.1$ a threshold of $2 - 3\sigma_{\eta}$, for $0.1 < K < 0.5$ $3 - 4\sigma_{\eta}$ and for $0.5 < K < 0.9$ $4 - 5\sigma_{\eta}$ is proposed. With these thresholds, the FPs of the HC with larger ω_c would be slightly higher than for the HC with lower crossover frequency.

The detection time for the change in CE dynamics for the different observer gains at different C was found. The detection times are highly dependent on the chosen observer gain K. The detection time decreases with increasing observer gain. This detection time excludes any human computational time or reaction time. From literature [1, 34] it is clear that human operators need around 200 milliseconds to react, so from the moment the human operator detects the change in CE dynamics to the moment the operator signals the detection is around 200 milliseconds.

Barragan [9] found during his study on changes in CE dynamics for a pursuit-tracking task that the mean detection time was 1.82 seconds for a change from single integrator-like to double integrator-like dynamics, with the faster detection times of around 0.6 seconds and the slowest detection times of around 5 seconds. This includes the time it took the participant to press a button once they detected the change in CE dynamics. So, subtracting this time for pressing the button from the detection time leaves an average detection time of around 1.62 seconds.

There is, in the data from Barragan [9], however, quite a lot of variability in the detection data; some participants took over 5 seconds for the detection, and some participants took around 0.6 seconds to detect the change in CE dynamics and press the button. The new model shows that the higher the remnant power ratio, the longer the detection takes; for a remnant power ratio of 0.2, the average detection time varies from 1.09 to 3.61 seconds for a K between 0.01 and 0.9 with the proposed values for C, which seems very much in line with the data found by Barragan [9]. The model seems to determine the average detection time using the innovation signal well. However, it would be important to determine the average remnant power ratio of the HC.

From the data from Barragan [9], it seems that the detection threshold of around 3-$4\sigma_{\eta}$ with an observer gain of around 0.1-0.5 would yield results similar to the found detection times for changes in CE dynamics. The experiment from Barragan [9] showed that two participants made a mistake in detecting a change in CE dynamics while controlling single integrator-like dynamics when no change in CE dynamics had occurred. Therefore, during the experiments, two false positives were made. A total of 17 participants did six trials each for the single integrator-like dynamics for a total of 102 trials with two false positives. This leaves a false positive rate of 0.02, while no false negatives were recorded. At this false positive rate for the highest possible true positive rate, the observer gain would be between 0.1-0.5 with C between 3-4. Both the detection time and the false positive rate would suggest that humans indeed can use the innovation signal to detect changes in CE dynamics, with a threshold of around 3-4 sigma with an observer gain of around 0.1-0.5.

The next step in this research would be to analyse the innovation signal $\eta(t)$ for a change in CE dynamics for different CE dynamics as proposed in other literature [1, 2, 9], e.g. DI to SI, or CE dynamics more similar to each other. It has to be noted that for a change from DI to SI the HC model for the MC cannot be used [11, 33]. This change would be harder to detect due to the HC not being required to introduce any lead themselves when controlling SI, but they were already tracking with lead when controlling the DI dynamics [35]. This would mean that the innovation signal $\eta(t)$ would cross the thresholds less quickly, taking longer to detect the change in CE dynamics. If the HC introduces a test input, some arbitrary stick movement, then the HC might be able to detect the change in CE dynamics more quickly using the innovation signal $\eta(t)$ [11]. This would be because the innovation signal is given when the internal model of the CE dynamics is not the same as the actual CE dynamics, part of the target function $f_t(t)$ and the remnant $n(t)$. The model then can be validated using experiments with different CE dynamics.

Another point of further research would be to analyze the derivative of the innovation signal $\dot{\eta}(t)$. From literature [1, 9, 10, 12, 14, 34, 36, 37] it is clear that the human operator can "see" the derivative of a signal. So the operator would be able to deduce the rate of change of the innovation signal, just like Miller and Elking proposed [12]. The $\dot{\eta}(t)$ then can be tested against analytically derived multiples of the steady-state threshold $C\sigma_{\dot{\eta}}$. This new model could help more accurately predict the moment an HC detects a change in CE dynamics for pursuit-tracking tasks.

The sigmoid activation function used in this research approximates a step input, due to the high value of the rate of change G. Another interesting point of research would be to analyze the innovation signal for slower change in CE dynamics. When the sigmoid activation function changes the CE dynamics more slowly then this would also affect the innovation signal $\eta(t)$. Therefore, the simulations can be run for different values of G to understand the effect of the sigmoid activation function on the detection of changes in CE dynamics using the innovation signal.

The last point of future research would be determining the innovation signal for participants of experiments. This would be quite tricky as the internal model of the participant would have to be known. It would have to be assumed that then during steady-state tracking the internal model approximates the real CE dynamics, as proposed by Miller and Elkind for their model on compensatory tracking [16]. The remnant of the participant would also have to be estimated.

The idea of an internal model has been fundamental in research on changes in CE dynamics [2, 12, 13, 19]. The internal model to drive the innovation signal has never been researched for pursuit-tracking tasks [14]. The innovation signal with the proposed model, however, seems to provide a solid basis for predicting how and when humans detect changes in CE dynamics during pursuit-tracking tasks. The model unlike MRAC [2] or detection methods based on $y(t)$, $\dot{y}(t)$ [9], $e(t)$ or $\dot{e}(t)$ [18], does not need a lot of reference data. It uses the HC control signal, allowing the HC to test whether a change in CE dynamics occurred by using a test input, which the other models do not allow. When the HC model and remnant approximate the real HC then using the innovation signal can predict well when the HC detects the change in CE dynamics. These recommendations could be used to further the research on the innovation signal and better help understand how humans detect changes in CE dynamics.

This model can help better understand the human adaptive process. This can help better understand how humans detect changes in CE dynamics during pursuit-tracking tasks. Understanding the human adaptive process can help better automate by predicting whether a human will or will not detect when a change in CE dynamics happens.

VI. Conclusion

The analysis of the innovation signal $\eta(t)$ for changes in CE dynamics offers valuable insights into human detection during pursuit-tracking tasks. The paper iterates the fact that the proposed model with the observer gain proves to be a promising model for detecting changes in CE dynamics using the innovation signal. The impact of the remnant power ratio on the variance of the innovation signal, influencing detection thresholds and subsequently true and false positive rates, has to be noted. The true and false positive rates decreased with increasing remnant power ratio due to the relatively smaller impact of the target function on the innovation signal post-transition. The influence of the HC gain on the true and false positive rates was negligible, however, there was a slightly slower detection for lower crossover frequency HCs around 0.03-0.4 seconds. The proposed model for observer gain 0.1-0.5 with thresholds 3-4σ, compared well with experimental data from Barragan, with a true positive rate of 0.99 and a false positive rate of 0.04. Higher values of the observer gain in the model would suggest the HC adjust their innovation signal based on the system output $y(t)$, resembling previous attempts to model the moment an HC detects a change in CE dynamics. Thereby, decreasing the average detection time. These findings enhance our understanding of how humans leverage the innovation signal to detect changes in CE dynamics. The identified factors and recommendations offer a solid foundation for future research, advancing our comprehension of human adaptive control mechanisms in dynamic environments by proposing a new model for the detection of changes in CE dynamics.

References

[1] Young, L. R., "On Adaptive Manual Control," *IEEE Transactions on Man-Machine Systems*, Vol. 10, No. 4, 1969, pp. 292–331. https://doi.org/10.1109/TMMS.1969.299931.

[2] Terenzi, L., Zaal, P. M. T., Pool, D. M., and Mulder, M., *Adaptive Manual Control: a Predictive Coding Approach*, 2022. https://doi.org/10.2514/6.2022-2448, URL https://arc.aiaa.org/doi/abs/10.2514/6.2022-2448.

[3] Drop, F. M., "Control-Theoretic Models of Feedforward in Manual Control," *Delft University of Technology*, 2016. https://doi.org/https://doi.org/10.4233/uuid:7c1f62db-9a5a-4e02-8f11-488d6a299500.

[4] "Loss of Control In-flight (LOC-I)," https://www.iata.org/en/programs/safety/operational-safety/loss-of-control-inflight/, 2023. Accessed: 2024-02-05.

[5] Young, L. R., Green, D. M., Elkind, J. I., and Kelly, J. A., "Adaptive Dynamic Response Characteristics of the Human Operator in Simple Manual Control," *IEEE Transactions on Human Factors in Electronics*, Vol. HFE-5, No. 1, 1964, pp. 6–13. https://doi.org/10.1109/THFE.1964.231648.

[6] Plaetinck, W., Pool, D. M., van Paassen, M. M., and Mulder, M., "Online Identification of Pilot Adaptation to Sudden Degradations in Vehicle Stability," *IFAC-PapersOnLine*, Vol. 51, No. 34, 2019, pp. 347–352. https://doi.org/https://doi.org/10.1016/j.ifacol.2019.01.020, URL https://www.sciencedirect.com/science/article/pii/S2405896319300229, 2nd IFAC Conference on Cyber-Physical and Human Systems CPHS 2018.

[7] Zaal, P. M. T., "Manual Control Adaptation to Changing Vehicle Dynamics in Roll–Pitch Control Tasks," *Journal of Guidance, Control, and Dynamics*, Vol. 39, No. 5, 2016, pp. 1046–1058. https://doi.org/10.2514/1.G001592.

[8] van Grootheest, A., Pool, D. M., van Paassen, M. M., and Mulder, M., "Identification of Time-Varying Manual-Control Adaptations with Recursive ARX Models," *American Institute of Aeronautics and Astronautics Inc. (AIAA)*, 2018. https://doi.org/10.2514/6.2018-0118.

[9] Barragan, M., "Modeling the Human Operator's Detection of a Change in Controlled Element Dynamics," *Delft University of Technology*, 2023. https://doi.org/http://resolver.tudelft.nl/uuid:5d9f79a5-6686-4767-a01d-01dc341fa990.

[10] McRuer, D. T., and Jex, H. R., "A Review of Quasi-Linear Pilot Models," *IEEE Transactions on Human Factors in Electronics*, Vol. HFE-8, No. 3, 1967, pp. 231–249. https://doi.org/10.1109/THFE.1967.234304.

[11] Mulder, M., Pool, D. M., van der El, K., and van Paassen, M. M., "Neuroscience Perspectives on Adaptive Manual Control with Pursuit Displays," *IFAC-PapersOnLine*, Vol. 55, No. 29, 2022, pp. 160–165. https://doi.org/https://doi.org/10.1016/j.ifacol.2022.10.249, 15th IFAC Symposium on Analysis, Design and Evaluation of Human Machine Systems HMS 2022.

[12] Miller, D. C., and Elkind, J. I., "The Adaptive Response of the Human Controller to Sudden Changes in Controlled Process Dynamics," *IEEE Transactions on Human Factors in Electronics*, Vol. HFE-8, No. 3, 1967, pp. 218–223. https://doi.org/10.1109/THFE.1967.233971.

[13] Phatak, A. V., and Bekey, G. A., "Decision processes in the adaptive behavior of human controllers," *IEEE Transactions on Systems Science and Cybernetics*, Vol. 5, No. 4, 1969, p. 339–351.

[14] Mulder, M., Pool, D. M., van der El, K., Drop, F. M., and Van Paassen, M. M., "Manual Control with Pursuit Displays: New Insights, New Models, New Issues," *IFAC-PapersOnLine*, Vol. 52, 2019, pp. 139–144. https://doi.org/10.1016/j.ifacol.2019.12.125.

[15] Fu, K. S., and Knoop, D. E., "An adaptive model of the human operator in a control system," *Control and Information Systems Laboratory, School of Electrical Engineering*, Vol. 64-15, 1964.

[16] Miller, D. C., and Elkind, J. I., "The Adaptive Response of the Human Controller to Sudden Changes in Controlled Process Dynamics," *IEEE Transactions on Human Factors in Electronics*, Vol. HFE-8, No. 3, 1967, pp. 218–223. https://doi.org/10.1109/THFE.1967.233971.

[17] Weir, D. H., and Phatak, A. V., "Model of human operator response to step transitions in controlled element dynamics." *NASA CR-671. NASA Contract Rep NASA CR.*, 1967, pp. 1–33. https://doi.org/10.1037/e506122009-007.

[18] van Ham, J., Pool, D. M., and Mulder, M., "Predicting Human Control Adaptation from Statistical Variations in Tracking Error and Error Rate," *IFAC-PapersOnLine*, Vol. 55, 2022, pp. 166–171. https://doi.org/10.1016/j.ifacol.2022.10.250.

[19] Hess, R., "A model for pilot control behavior in analyzing potential loss-of-control events," *Proceedings of the Institution of Mechanical Engineers, Part G: Journal of Aerospace Engineering*, Vol. 228, 2014, pp. 1845–1856. https://doi.org/10.1177/0954410014531218.

[20] Hess, R., "Modeling Pilot Control Behavior with Sudden Changes in Vehicle Dynamics," *Journal of Aircraft*, Vol. 46, 2009, pp. 1584–1592. https://doi.org/10.2514/1.41215.

[21] Hess, R., "Modeling the Pilot Detection of Time-Varying Aircraft Dynamics," *Journal of Aircraft*, Vol. 49, 2012, pp. 2100–2104. https://doi.org/10.2514/1.C031805.

[22] Hess, R., "Modeling Human Pilot Adaptation to Flight Control Anomalies and Changing Task Demands," *Journal of Guidance, Control, and Dynamics*, Vol. 39, 2015, pp. 1–12. https://doi.org/10.2514/1.G001303.

[23] Jakimovska, N., M., P. D., van Paassen, M. M., and Mulder, M., *Using the Hess Adaptive Pilot Model for Modeling Human Operator's Control Adaptations in Pursuit Tracking*, 2023. https://doi.org/10.2514/6.2023-0541, URL https://arc.aiaa.org/doi/abs/10.2514/6.2023-0541.

[24] Neilson, P. D., and Neilson, M. D., "A neuroengineering solution to the optimal tracking problem," *Human Movement Science*, Vol. 18, 1999, pp. 155–183.

[25] Neilson, P. D., Neilson, M. D., and O'Dwyer, N. J., "Adaptive Optimal Control of Human Tracking," *Motor Control and Sensory Motor Integr.: Issues and Directions,*, Vol. In D.J. Glencross and J.P. Piek (eds.), 1995, p. 97–140.

[26] van der El, K., Pool, D. M., Van Paassen, M. M., and Mulder, M., "Effects of Preview on Human Control Behavior in Tracking Tasks With Various Controlled Elements," *IEEE transactions on cybernetics*, Vol. PP, 2017. https://doi.org/10.1109/TCYB.2017.2686335.

[27] Newland, D. E., *An Introduction to Random Vibrations and Spectral Analysis*, 2^{nd} ed., Longman Scientific and Engineering, New York, 1984.

[28] Vinodh, E., Jovitha, J., and Ayyappan, S., "Comparison of four state observer design algorithms for MIMO system," *Archives of Control Sciences*, Vol. 23, 2013. https://doi.org/10.2478/acsc-2013-0015.

[29] Zaal, P. M. T., Pool, D. M., Chu, Q. P., Van Paassen, M. M., Mulder, M., and Mulder, J. A., "Modeling Human Multimodal Perception and Control Using Genetic Maximum Likelihood Estimation," *Journal of Guidance, Control, and Dynamics*, Vol. 32, No. 4, 2009, pp. 1089–1099. https://doi.org/10.2514/1.42843.

[30] van Paasen, M. M., van der Vaart, J. C., and Mulder, J. A., "Model of the Neuromuscular Dynamics of the Human Pilot's Arm," *Journal of Aircraft*, Vol. 41, No. 6, 2004, pp. 1482–1490. https://doi.org/10.2514/1.14434.

[31] Laurense, V. A., Pool, D. M., Damveld, H. J., Paassen, M. M. v., and Mulder, M., "Effects of Controlled Element Dynamics on Human Feedforward Behavior in Ramp-Tracking Tasks," *IEEE Transactions on Cybernetics*, Vol. 45, No. 2, 2015, pp. 253–265.

[32] Mulder, M., Pool, D. M., van der El, K., and van Paassen, M. M., "Probabilistic Perspective on Compensatory, Pursuit and Preview Manual Control," *IFAC-PapersOnLine*, Vol. 55, No. 29, 2022, pp. 154–159. https://doi.org/https://doi.org/10.1016/j.ifacol.2022.10.248, 15th IFAC Symposium on Analysis, Design and Evaluation of Human Machine Systems HMS 2022.

[33] van der El, K., Pool, D. M., and Mulder, M., "Analysis of Human Remnant in Pursuit and Preview Tracking Tasks," *IFAC-PapersOnLine*, Vol. 52, No. 19, 2019, pp. 145–150. https://doi.org/https://doi.org/10.1016/j.ifacol.2019.12.165, 14th IFAC Symposium on Analysis, Design, and Evaluation of Human Machine Systems HMS 2019.

[34] Elkind, J. I., and Forgie, C. D., "Characteristics of the human operator in simple manual control systems," *IRE Transactions on Automatic Control*, Vol. AC-4, No. 1, 1959, pp. 44–55. https://doi.org/10.1109/TAC.1959.6429402.

[35] Mulder, M., Pool, D. M., van der El, K., Drop, F. M., and Van Paassen, M. M., "Manual Control with Pursuit Displays: New Insights, New Models, New Issues," *IFAC-PapersOnLine*, Vol. 52, 2019, pp. 139–144. https://doi.org/10.1016/j.ifacol.2019.12.125.

[36] Mulder, M., Pool, D. M., Abbink, D., Boer, E., and Van Paassen, M. M., "Fundamental Issues in Manual Control Cybernetics," *IFAC-PapersOnLine*, Vol. 49, 2016. https://doi.org/10.1016/j.ifacol.2016.10.429.

[37] Mulder, M., Pool, D. M., Abbink, D., Boer, E., Zaal, P. M. T., Drop, F. M., van der El, K., and Van Paassen, M. M., "Manual Control Cybernetics: State-of-the-Art and Current Trends," *IEEE Transactions on Human-Machine Systems*, Vol. PP, 2017, pp. 1–18. https://doi.org/10.1109/THMS.2017.2761342.

Part II

Preliminary Thesis Report

*This part has been assessed for the course AE4020 Literature Study.

1

Introduction

Evidence from aircraft accident reports emphasizes that control system failures, such as gain changes and stability augmentation issues, have resulted in crashes despite pilots potentially being capable of maintaining control [1]. These accidents, often occurring during take-off, underscore the critical need to better understand the human adaptive process to prevent future mishaps. This awareness of human adaptability gained significance during the 1960s space race when NASA heavily invested in understanding human operator involvement in dynamic systems [2]. McRuer and Jex [3] played a pioneering role in this research by developing the crossover model, which provided insights into modelling pilot behaviour for various controlled element dynamics. Their work remains the basis of human-in-the-loop control element research.

Young et al. [1, 2] expanded on the research of McRuer and Jex and started doing experiments on adaptive human control. During their experiments, Young et al. [1, 2] came up with the adaptive control theory of how humans adapt to changes in the controlled element dynamics, changes in displays, but also polarity shifts, or input spectra. The theory, however, does not provide a model to accurately determine human detection of changes in controller element dynamics.

Subsequent research started working with the idea of human expectation, where the human has an internal model, which drives their expectation and when this internal model output does not match the observation then a change in controlled element dynamics might have occurred. Miller and Elkind [4] proposed the idea that a human has a certain threshold for these internal models and when the change in expected error rate and observed error rate, over a small period T, exceeds a steady-state threshold a human will detect the change in controlled element dynamics. However, most of the research into the human adaptive process focused on a compensatory display, which depicts the difference between the target signal f_t and the system output y, in other words, the error e.

Most tracking in the world is done on pursuit displays, which show the target signal f_t and the system output y. Models for pursuit-tracking tasks have not yet been successful. Mulder et al., [5], proposed a model aimed at better understanding human expectation and the internal cognitive model that underlies it. This model based on the difference between human observation and expectation is aimed at providing a model for pursuit tracking tasks. This model will be used to answer the main research question proposed as follows:

How does the difference between human observation and expectation of the controlled system output determine the detection of changes in controlled element dynamics during pursuit-tracking tasks?

Understanding the factors that underlie human expectation and the influences on the difference between observation and expectation is crucial for answering the research question. Equally important is recognizing variations among human operators. Some may control ambitiously while others may lean toward lazier tracking. These individual differences can notably impact the difference between what is expected and what is observed by the human controller.

In Chapter 2 the model of Mulder et al. is explored, where the model's intricacies and significance are discussed and a deeper understanding of the human adaptive process is provided. In Chapter 3, the framework used for simulations is detailed, providing insights into the chosen model and the intricate simulation process, along with verification steps for each component of the simulation. In Chapter 4, the preliminary simulation results are explained, offering an analysis of the data and identifying the influence of the remnant and controlled element dynamics on the simulation. In Chapter 5, key findings are summarized, along with a critical evaluation of their implications within the broader context of human adaptation in dynamic environments. Finally, in Chapter 6, further research steps based on the study's insights are presented, offering valuable guidance for future research and potential enhancements to the simulation model.

2

Adaptive Manual Control

This chapter provides a detailed review of previous literature on adaptive manual control. More detailed information on the experiments performed, the difference between compensatory and pursuit displays and the different models proposed to better understand adaptive human behaviour pursuit control tasks. The chapter will then wrap up with a summary of the model used to answer the research question.

2.1. Adaptive Control Theory

According to Young et al [2], adaptive manual control is about how and when humans detect a change in either input spectra, controlled element gain, polarity and/or dynamics, display modality, and the limits of controllability under a variety of situations. Young et al. classified different kinds of adaptability under four different types namely [1, 2]:

- Input adaptation and prediction
- Controlled element adaptation
- Task adaptation
- Programmed adaptation

A schematic overview of these four different types of adaptation is given in Figure 2.1. According to Draper et al. [6], there are also slow adaptations such as fatigue, but this does not apply to the current research. Young et al. [1, 2] state that input adaptation and prediction is a human's ability to detect familiar/repeating patterns in the input signal, the human then can track these in a predictive or open loop fashion. Controlled element adaptation is the ability of humans to adapt different control strategies in response to changes in the controlled element dynamics [2].

Young [2] defines task adaptation as the matter of optimization of the manual control loop based on various control objectives. Thus, humans adapt their strategy for identical inputs and controlled elements, depending on the relative penalties linked to system errors, vehicle accelerations, the time required to reach a terminal state, fuel consumption penalties, or control effort. Programmed adaptation is defined as the human's way of adapting control strategies, which he/she has been taught, appropriate to the environmental factor [1].

The primary focus of this research revolves around controlled element adaptation, which is particularly intriguing. The aim is to understand better when humans detect changes in the dynamics of the controlled element. Hence, it is crucial to minimize the impact of other types of adaptation as much as possible. To tackle input adaptation and prediction, a viable approach is creating quasi-random input signals humans cannot easily predict [7]. However, it remains challenging to eliminate the human ability to comprehend signal distributions and expectations, even with quasi-random signals. The level of predictability in the signal significantly influences the degree of control the human operator can exert in an open-loop manner. Additionally, researchers have observed that human operators employ different control strategies when dealing with varying bandwidths in input signals [8]. This phenomenon is quantitatively described in the crossover model, McRuer and Jex [3]. As for task adaptation, its effects can be reduced by providing clear instructions [2].

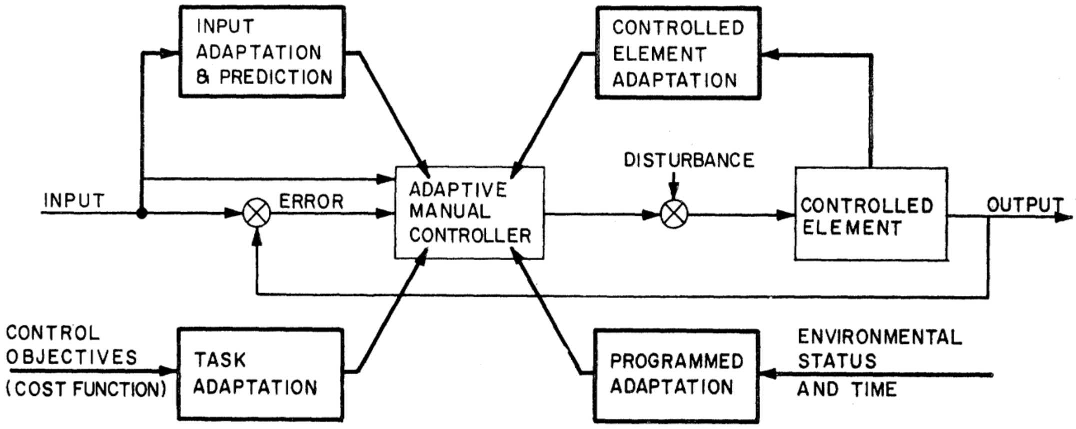

Figure 1. **Major adaptive functions in manual control.**

Figure 2.1: Major adaptive functions in manual control, Young Fig. 1 [1].

2.1.1. Compensatory vs. Pursuit displays analysis

Most research on the adaptive human process was performed using a compensatory display. A compensatory display shows only the system error e to the human controller as defined in Equation 2.1. With f_t the target signal and system output y.

$$e = f_t - y \tag{2.1}$$

A compensatory display only shows this system error e, the human controller cannot see the system output y or the target signal f_t. Pursuit displays present two symbols: the target signal f_t and the system output y. The system error e is the offset between the target signal f_t and system output y, which the human controller must minimize using control inputs. The different displays are given schematically in Figure 2.2 with e, f_t and y given in Figure 2.3.

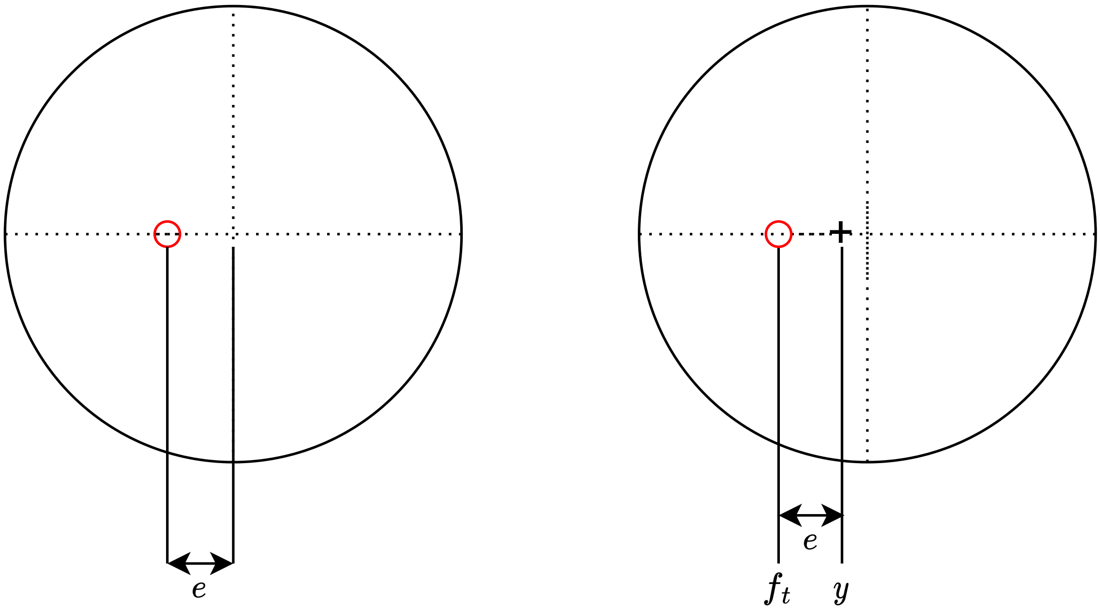

Figure 2.2: Schematic overview of a compensatory display (left) and a pursuit display (right).

Mulder et al. [9] argue that the research community has overly focused on modelling the exception in human control, which is feedback-only compensatory tracking. They suggest that more efforts should be

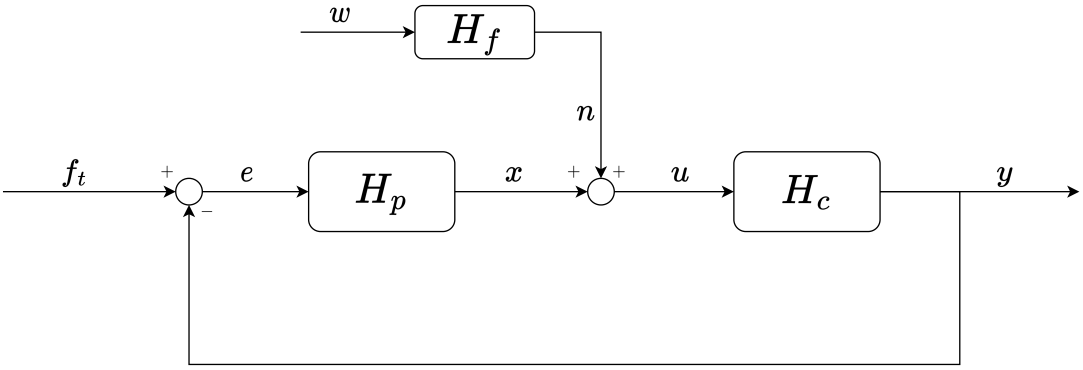

Figure 2.3: Simple negative feedback system with target function f_t and system output y.

directed toward understanding the broader concept of human control, involving pursuit and preview displays [9]. These displays are more versatile and realistic, reflecting the adaptability of the human biological system [9]. Harnessing this adaptability could lead to improved support systems and more human-like automation. Pursuit displays yield superior performance compared to the feedback-only compensatory display [9]. A comprehensive human control model for these pursuit displays has not been developed yet.

Modelling pursuit tasks is more complex than compensatory tracking due to the advantages offered by pursuit displays [9]:

- Enhanced Eye-Hand Coordination: Pursuit displays allow the human controller to observe both the system's output y and the target signal f_t, improving coordination.
- Exploration of System Dynamics: With explicit output feedback, controllers can explore the characteristics of the controlled element's dynamics, including derivatives, making it easier to control complex dynamics.
- Predictability: Displaying the target signal f_t separately enables learning and prediction of its properties, even in quasi-random signals.
- Target Anticipation: Separation of the target signal f_t and system output y allows controllers to anticipate target signal movement, offering a wide range of control strategies.

Overall, pursuit displays enable a more extensive exploration of control strategies compared to feedback-only compensatory tracking, making mathematical modelling of human behaviour in pursuit tasks much more challenging. Past attempts have not resulted in universally accepted adaptive human control models. Therefore, firstly this chapter will dive into the research done for compensatory displays, and then later explain the newer proposed models for pursuit displays.

2.2. Adaptive Manual Control Experiments

This section summarises the early research and experiments done on adaptive manual control. It is important to note the experiments were all performed using compensatory displays, which show the difference between the target signal f_t and the system output y, in other words, the system error e.

2.2.1. Young, Elkin and Draper's research on gain and polarity reversal and adaptation

Young et al. [2], in 1964, pioneered the research in adaptive manual control and did the first experiments on adaptive human behaviour. It is important to note that the exact number of subjects was not given, only the results of two subjects were discussed. Both subjects were highly trained and prepared for changing controlled element dynamics. The experiment was performed on a compensatory display. The experiment was mostly done on sudden polarity and controlled element gain changes. The controlled element itself was a pure simple gain. Young et al. [2] wanted to figure out how fast humans adapt to these changes and which factors play a role in human adaptive behaviour. This would then be used to better understand the human adaptive process.

According to Young et al. [2], well-trained human controllers can switch from pre-transition to post-transition in a more or less discrete mode-switching fashion, during rapid changes in gain or controlled element dynamics. Slow changes to controlled element dynamics may be treated as a quasi-stationary sequence of time-invariant dynamics [2]. Young et al. [2] state that some levels of adaption are below the human controllers' level of conscience and therefore come naturally to the human controller.

Young and Elkind started doing the aforementioned experiments with sudden controlled element gain switches without any external cues provided to the human controller [1]. The human controller was performing his control task on a compensatory display so only the system error e could be used to determine if the controlled element dynamics had changed suddenly and that he had to adapt. The controlled element gain doubled between the two time steps in a step-input fashion. This caused the human controller to overshoot following a gain increase, and then the system error e returned to zero after the human controller adapted their gain. The responses after subsequent identical steps showed almost perfect adaptation to the new gain level, as seen in Figure 2.4 [1].

From Figure 2.4 it can be seen that the human controller following an increase of the controlled element gain adapts their control strategy after around 300-400 ms.

Draper et al. [6], experimented with a sudden polarity switch of the controlled element dynamics of a simple gain control. This turned the stable closed-loop negative feedback system into an unstable positive feedback system. Therefore, to get the system stable again the human controller needed to change their polarity. It was found that for approximately 0.5 seconds, the response was divergent, after which the human controller changed their polarity [6]. The tracking resumed like normal after around 1 second after the transition. A gain change accompanied by a change in the polarity of the controlled element dynamics showed many signs of an adaptation to a polarity change and a gain change separately [6].

It was found from these experiments that major control adaption generally occurs in 0.4 to 0.8 seconds following the change in controlled element dynamics, as can be seen in Figure 2.5 [2]. The resulting system error e is corrected within the next 1 to 3 seconds. There was an indication that a human first adapts to a polarity change and then to the gain change when both are present. So stability is most important for the human controller and then next the adjustment of the open loop gain.

From these experiments Young et al. [2], determined that the human adaptive process consists of three phases: the detection, identification and modification phase. In the detection phase, the human controller would detect a change in controlled element dynamics, during the identification phase the new system dynamics would be identified, and during the modification phase the control law would be updated and the human controller would optimise their control parameters.

2.2.2. Miller and Elkind model for detecting a change in controlled element dynamics

Miller and Elkind [4], described the process of adaptation by doing experiments with well-trained human operators doing their control task on a single integrator-controlled element. They separated the phases of human adaptation into detection, identification, modification (mode-switching adjustment, and parameter optimization [4]. Miller and Elkind [4] added the idea that a human controller has an internal model of the controlled element dynamics. The idea of internal models came from Knoop and Fu [10] and was implemented into the model of Miller and Elkind. The model of Miller and Elkind will be adjusted to fit the convention used in the previous sections. This section will also use the innovation signal η which is defined as the difference between human observation and expectation.

The model of Miller and Elkind was made for a compensatory display, therefore, the human controller could only see the system error e. The human controller's task is to keep $f_t(t) = y(t)$ or in other words $e(t) = 0$ [4], the human controller does this by making control inputs $u(t)$. Miller and Elkind [4] used the fact that the system error e is the difference between the target function f_t and the system output y and that the system output derivative can be written as Equation 2.2 for single-integrator controlled element dynamics given by $\frac{K_c}{s}$.

$$\dot{y} = K_c u(t) \tag{2.2}$$

This means that the derivative of the system error $\frac{de(t)}{dt}$ can now be given as Equation 2.3. With $\frac{dy(t)}{dt}$ given in Equation 2.2. Miller and Elkind [4] then rewrote Equation 2.3 by looking over a short control

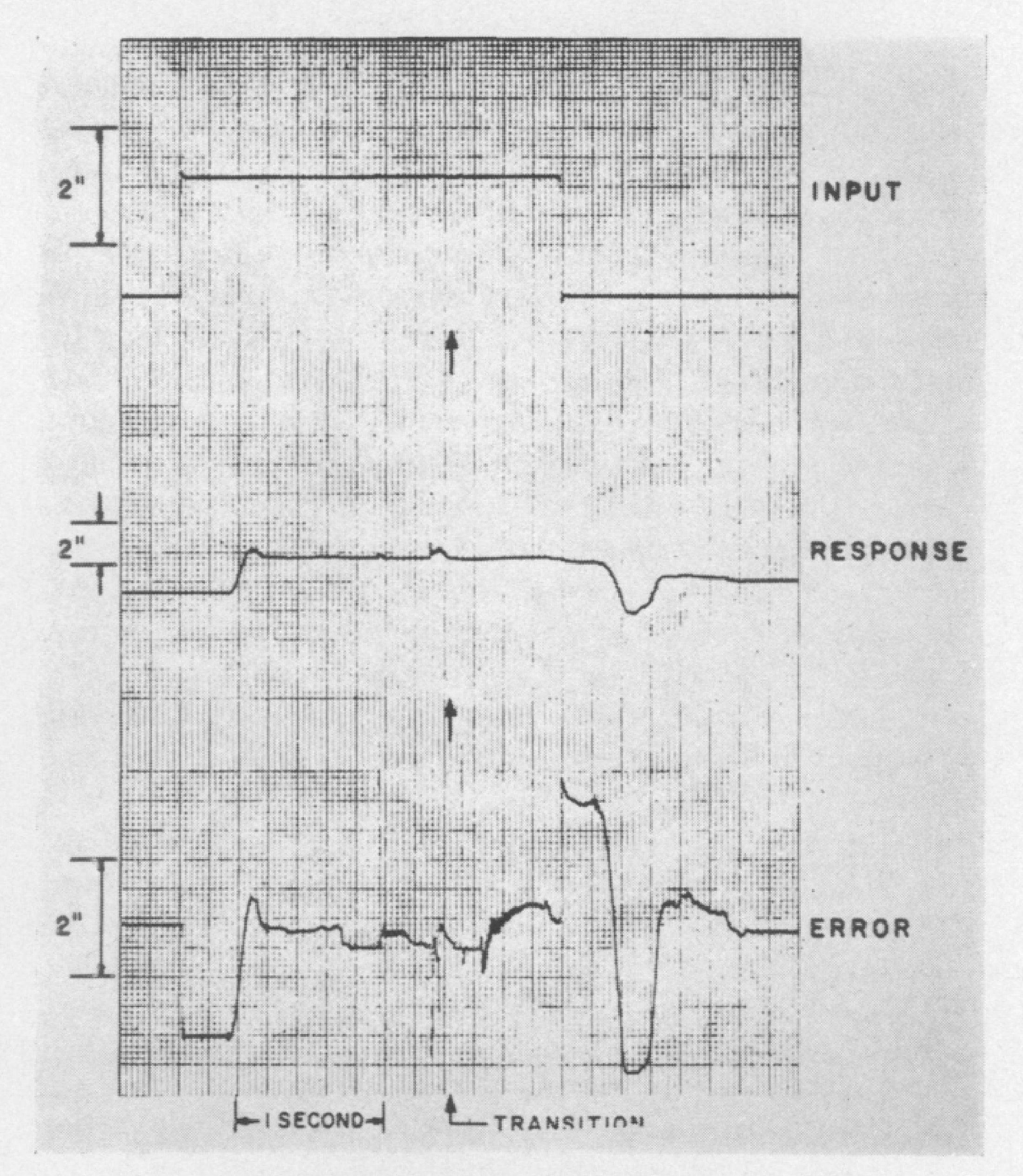

Figure 2.4: Step response before and after a gain increase, Young et al. Fig. 3 [2]. Where INPUT is the controlled element gain. The RESPONSE is the human controller's control output u and ERROR is the system error e.

interval of time T resulting in Equation 2.4. This gives the equation for the change in system error rate $\dot{e}$ during a control interval with time T given that the controlled element dynamics are time-invariant over this control interval. So if T is defined by t_1 and t_2 then Equation 2.4 is the same as Equation 2.5. This change in system error rate $\Delta\dot{e}$ is the human controller's change in the system error rate observation.

$$\dot{e}(t) = \dot{f}_t(t) - K_c u(t) \tag{2.3}$$

$$\Delta\dot{e} = \Delta\dot{f}_t - K_c \Delta u \tag{2.4}$$

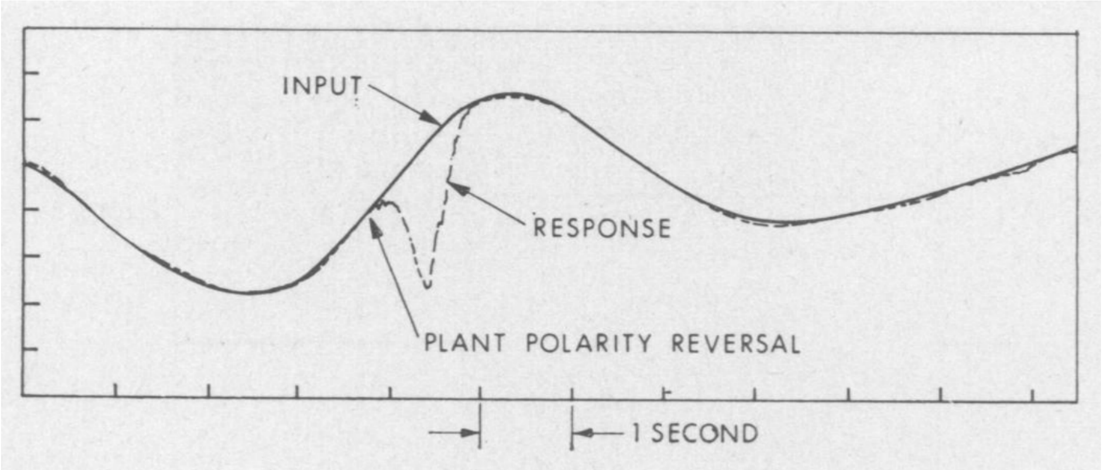

Figure 2.5: Pilot adaptation to control reversal, Draper et al. Fig. 4 [6]. Where INPUT is a low frequency continuous random target signal f_t and response is the system output y.

$$\dot{e}(t_2) - \dot{e}(t_1) = \dot{f}_t(t_2) - K_c u(t_2) - (\dot{f}_t(t_1) - K_c u(t_1)) \tag{2.5}$$

Miller and Elkind [4] state that the human controller has an internal model for this change in system error rate $\Delta\dot{e}$, this is the human controller change of the system error rate expectation. With a compensatory display, the human controller cannot see target signal f_t and thus the human controller can also not see $\Delta\dot{f}_t$. Therefore, the change of system error rate expectation is given by Equation 2.6 [4]. When the human controller is well-trained, the operator's internal model approaches the true model $K_{internal} \approx K_c$. The $K_{internal}$ is the gain of the internal model of the human controller of the controlled element dynamics.

$$\widehat{\Delta\dot{e}} = -K_{internal}\Delta u \tag{2.6}$$

Miller and Elkind [4] then define the discrepancy which is the difference between the actual and expected change in system error rate $\Delta\dot{e} - \widehat{\Delta\dot{e}}$. This will be redefined as the change of the innovation signal rate $\Delta\dot{\eta}$, with it being the difference between the change of the system error rate observation $\Delta\dot{e}$ and the change of the system error rate expectation $\widehat{\Delta\dot{e}}$, over a small control interval of time T. So this change of the innovation rate is defined in Equation 2.7

$$\Delta\dot{\eta} = \Delta\dot{e} - \widehat{\Delta\dot{e}} \tag{2.7}$$

Miller and Elkind [4] state that the human controller will compare the change of the innovation rate $\Delta\dot{\eta}$ with the time-invariant standard deviation of the change of the innovation rate $\sigma_{\Delta\dot{\eta}}$.

Miller and Elkind [4] define the variable Z in Equation 2.8 and when this variable exceeds C times the standard deviation of the change of the innovation rate $C\sigma_{\Delta\dot{\eta}}$, the acceptable limit, then the human controller will know that a change in controlled element has occurred.

$$Z \equiv \frac{\Delta\dot{\eta}}{\sigma_{\Delta\dot{\eta}}} \tag{2.8}$$

For the time-invariant case, the change of the innovation rate $\Delta\dot{\eta}$ is distributed with zero mean and variance given by Equation 2.9 [4]. The variance has two components one part is the variance due to the change in the target signal rate $\dot{f}_t$ and the second part may be treated as if it were the variance due to the model gain [4]. This second part includes all the perceptual and memory limitations of a human controller [4]. σ_m^2 is the variance that would be observed if the human controller had a unity gain internal model [4]. From Equation 2.6 it can be seen that $K_{internal}\Delta u$ is the expected change of the system error rate $-\widehat{\dot{e}}$, leading to Equation 2.10.

$$\sigma^2_{\Delta\dot{\eta}} = \sigma^2_{\dot{f}_t} + (K_{internal}\Delta u)^2\sigma^2_m \tag{2.9}$$

$$\sigma^2_{\Delta\dot{\eta}} = \sigma^2_{\dot{f}_t} + (\widehat{\Delta\dot{e}})^2\sigma^2_m \tag{2.10}$$

If a control movement deviates by more than C standard deviations of the change of the innovation rate $\Delta\dot{\eta}$, the human controller must conclude that there has been a change in the dynamics of the controlled element [4]. The magnitude of the required deviation before change detection increases with the expected change in system error rate. In other words, the human controller will only perceive a change when the deviation surpasses the set acceptability limits [4]. These limits can never be less than C times $\sigma_{\Delta\dot{f}_t}$. Beyond this threshold, they should grow in proportion to the expected change of the system error rate $\widehat{\Delta\dot{e}}$, where the constant of proportionality is C times σ_m [4].

After detection, the human controller will move into the identification phase. Here the human controller has to identify the new controlled element dynamics to recover the system error e within acceptability limits. For the experiment of Miller and Elkind [4] the three participants were well-trained in all the different possible controlled element dynamics. Therefore, the participants had good internal models and were able to identify them quickly. According to Miller and Elkind [4], the participants internally calculate the change of the innovation rate $\Delta\dot{\eta}_i$ for every different controlled element dynamics (i) and try to find the controlled element dynamics in which $\Delta\dot{\eta}$ is within the acceptable limits [4].

If none of the systems $\Delta\dot{\eta}_i$ fits within the acceptable limits then the detection of the change in controlled element dynamics might have occurred during the transition. In this case, it is important to also take the transition into account when identifying the correct new system. This is achieved by considering the change in system gain during the interval and incorporating this change when calculating $\Delta\dot{\eta}_i$. If this still doesn't yield a suitable system then the whole process will be repeated in another time interval. Figure 2.6 is a visualisation of the whole detection, identification, modification and optimization process as described by Miller and Elkind [4]. During the modification and optimization phase, the human controller adjusts his system control parameter to the new controlled element dynamics, making sure the system error e gets back into the acceptable thresholds [2, 11, 4]. To test their model Miller and Elkind [4] did some experiments with the three well-trained participants controlling a single integrator dynamics during a compensatory tracking task. When the participants recognised the change in controlled element dynamics they were to press a button on the joystick. It was found that adding this extra task did not influence the tracking performance [4].

Miller and Elkind [4] started by investigating the detection phase, the reaction time of an operator was assumed to be around 200 ms. Therefore, it was assumed that the transition was detected 200 ms before the human controller pressed the button on the joystick. Using the difference between the expected system error rate $\Delta\widehat{\dot{e}}$ and the observed system error rate $\Delta\dot{e}$ at the moment of detection the acceptability limits could be determined.

From this investigation, it was discovered that there was a considerable variation in detection times during system transitions that led to instability (characterized by gain increases and polarity reversals) [4]. This variation occurred due to the system error rate $\dot{e}$ rising too rapidly. On the other hand, transitions involving gain decreases provided more stable outcomes, as the system error$e$ built up more gradually [4]. Based on these results, the acceptability limits were deduced and subsequently employed to predict detection times, which were then compared to the measured detection times.

Figure 2.7 shows the time the button was pressed versus the time the change of the innovation rate $\Delta\dot{\eta}$ exceeds the acceptable limits. A line is plotted at 400 ms which would be the time the human needs to detect and calculate the correct internal model. The figure shows data from one participant but is typical of all the results [4]. It can be seen that the human controller never signals a detection until at least 200 ms after the model predicts the human controller would detect the change in controlled element dynamics [4]. It can be seen that the stable transitions a gain decrease would take much longer to detect than the unstable ones such as a gain increase or polarity reversal. This means that the detection time of a change in controlled element dynamics is highly dependent on the kind of change in CE dynamics.

Miller and Elkind [4] then checked if the model could effectively predict the correct system after a transition and whether it could provide insights into why participants made mistakes. During gain increase

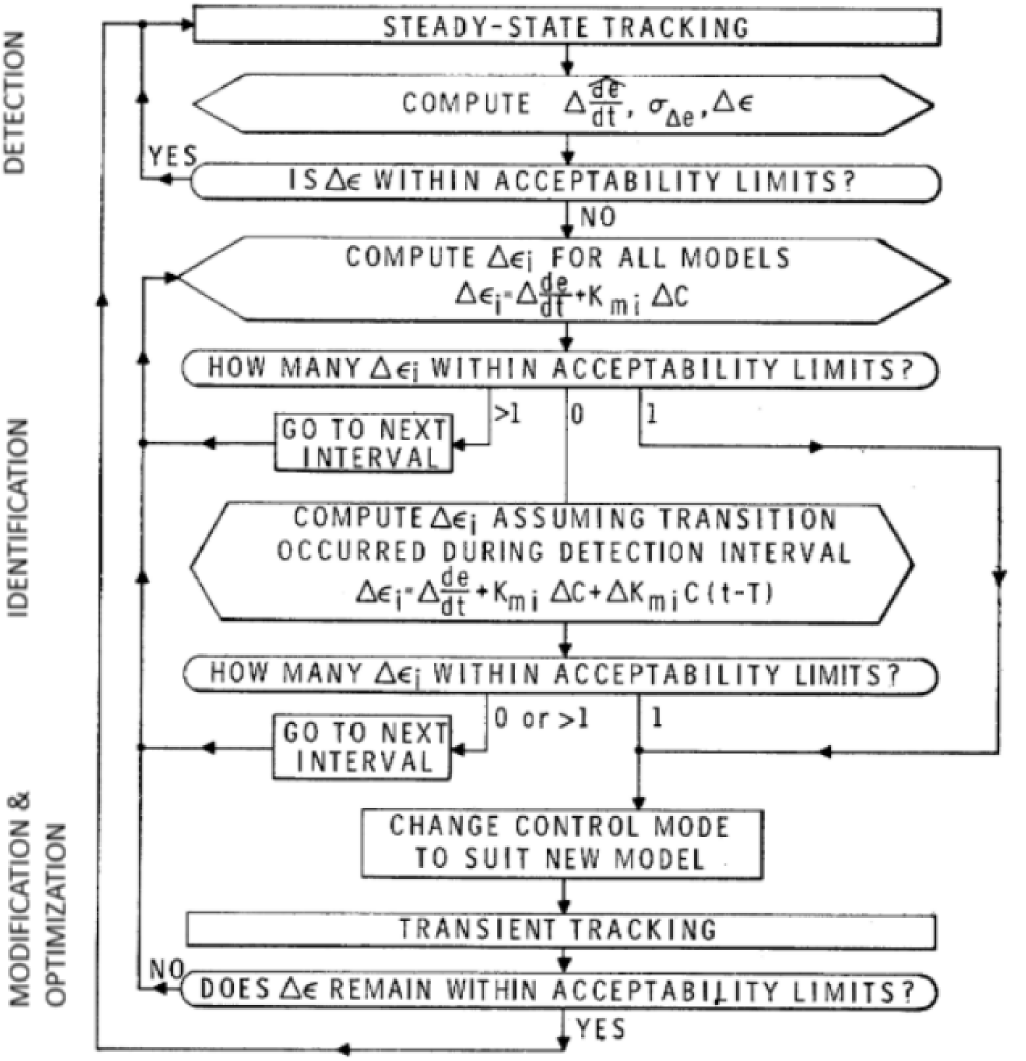

Figure 2.6: Identification, modification and optimization process as described by Miller and Elkind Fig 2. [4].

or polarity reversal transitions, participants consistently and accurately identified the correct system. The model's predictions were also quite close to the experimental data, except for a few corner cases where participants possibly made decisions based on probability calculations. In these cases, multiple potential options fell within the acceptability limits, leading to some ambiguity. However, when the transition involved a gain decrease, participants faced more challenges in correctly identifying the system, often mistaking it for a polarity reversal about half of the time [4]. Interestingly, the model also predominantly labelled these instances as polarity reversals, indicating its ability to anticipate situations where humans struggle to identify the correct system.

Elkind et al. [8] also experimented with introducing double integrator dynamics when the controlled element experienced a gain and polarity switch. During this experiment, the human controller corrected the polarity reversal within 1 second and then needed 20 seconds to adjust to the new double integrator dynamics. One of the two cycles of oscillatory behaviour was attributed to the gain increase the other cycle was attributed to the human operator trying to optimize their lead term [8, 2]. This experiment showed the great time and effort a human controller takes to identify the post-transition dynamics.

Elkind et al. [8], then experimented with an auditory cue when the controlled element dynamics would change, this did not affect the identification phase but did shorten the detection phase of the human

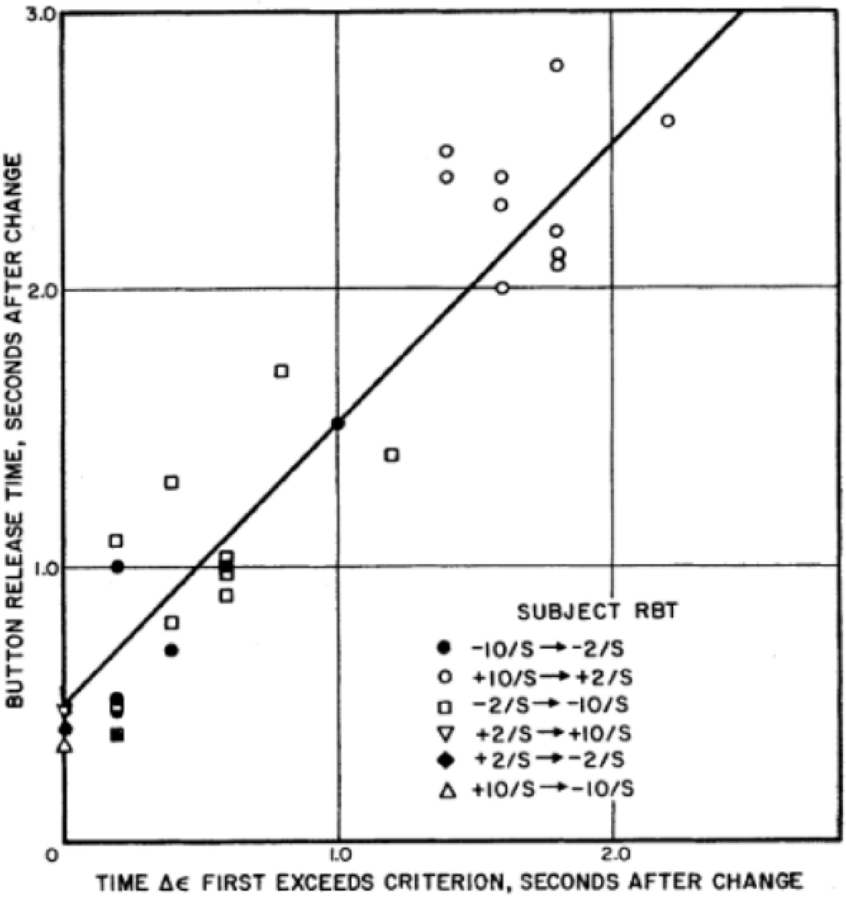

Figure 2.7: Results from the experiment by Miller and Elkind of the actual vs predicted detection data Fig 4. [4].

controller. Miller [4] found that unstable transitions, which lead to the largest system error e, have the shortest detection time. He implemented a detection criterion model based on comparing the actual change in system error with the expected one and the statistics of the input.

2.2.3. Weir and Phatak optimal controller theory

Weir and Phatak [12], used Elkind's data to calculate the maximum system error for a given failure, by tabulating the time spent tracking with pretransition dynamics. They simulated well-damped second-order vehicle dynamics with an augmentation system. Then the augmentation system would fail, causing the system to become unstable requiring rapid pilot adaptation [12]. At the time of failure, the controlled element dynamics would become double integrator-like dynamics. Even though these double integrator-like dynamics could be controlled relatively easily in the steady-state, the transient response following the failure would go through an oscillatory period, damping out after 6 seconds [12].

From this data Weir and Phatak [12], came up with their theory about optimal controller. This model consists of three phases. The first phase is the pretransition retention phase, the human controller controls, in this phase, as if the controlled element is still in the pretransition dynamics. After detection, the human controller would behave like a time-optimal controller to decrease the system error e as quickly as possible to acceptable levels. In earlier work from Young and Meiry [13], it was found that humans tend to control like time-optimal controllers in difficult control tasks. The last phase of the optimal controller is the posttransition steady-state, in this phase the system error e and system error rate $\dot{e}$ are within acceptable bounds again. The human controller switches back to the steady-state quasi-linear control for the new controlled element dynamics. The model does not present a strategy for identification but merely that the human operator can identify and adjust to the new controlled element dynamics.

Weir and Phatak [12] mostly focused on transitions which would yield an unstable system during the pretransition retention phase. These unstable systems would yield the best time-optimal controller type of trajectories as the participant would have to react quickly to retain control over the system. It has to be noted, however, that sometimes the human operator would correct for a polarity reversal which did not happen. This was most likely due to the high penalty given for not reacting to the change in controlled element dynamics.

2.2.4. Phatak and Bekey sequential identification model

Phatak and Bekey [14] expanded on the earlier model [12], by adding decision control logic to it. The sequential identification model works based on that the identification process happens in a sequential order using pattern recognition of the system error e and system error rate $\dot{e}$. A change in controlled element dynamics would be identified when the system error e and system error rate $\dot{e}$ pass a decision region. The new controlled element dynamics can then be identified by the human controller once the system error e and system error rate $\dot{e}$ enter the next decision region.

It is proposed that a human operator can store maximum absolute values of system error values of the system dynamics in pre-failure steady-state conditions [14]. Once these values surpass certain limits defined by decision regions, the operator will detect a failure. Figure 2.8 illustrates a phase plane with system error e and system error rate $\dot{e}$ on the axes, displaying the decision regions. During changes in the dynamics of the controlled element, typically both system error e and system error rate $\dot{e}$ increase. Upon crossing the first decision region (DR-1), the supervisory control algorithm advances to the next step in the decision tree.

In Figure 2.8 the decision regions are shown. Phatak and Bekey [14] state that the decision regions come from the human controller stored maximum system error e and maximum system error rate $\dot{e}$ during pre-failure steady-state tracking. The bounds of the decision region 1 (DR-1) are 2 times the maximum system error rate $\dot{e_{Max}}$. Decision region 2 (DR-2) is bounded by 4 times the maximum system error rate $\dot{e_{Max}}$ and slopes of on the line $\dot{e} = -e$. The reason for this is that the system error is convergent in these regions as $e < 0$ but $\dot{e} > 0$ and $e > 0$ but $\dot{e} < 0$. Decision region 3 (DR-3) is located in a divergent region as $e < 0$ but $\dot{e} < 0$ and $e > 0$ but $\dot{e} > 0$.

Once the human controller has detected a change in controlled element dynamics utilizing the system error e and system error rate $\dot{e}$ exceeding the first decision region (DR-1) then the human operator model is adjusted [14]. The HC operator model is adjusted based on the new controlled element dynamics [14]. Consequently, if the system error rate $\dot{e}$ changes sign and enters decision region 2 (DR-2) then the current model for the human operator is already capable of handling the new system. Otherwise, the next step in the decision tree is reached, and the human operator model undergoes further adjustments.

This process continues until the system stabilizes, and the system error e values return to normal levels. The decision regions were empirically determined and relied on the specific dynamics of the controlled element under consideration. As a result, there is no definite basis to formulate a strategy for determining these regions without conducting experiments first.

To validate their model, Phatak and Bekey [14] conducted an experiment with one skilled pilot and compared its model results with the experiment data obtained. To simulate a time-varying control scenario, they utilized the failure of the stability augmentation system in an aircraft. This augmentation system involved two feedback loops, with either one or both capable of failing, thereby introducing the time-varying element.

The pilot involved in the experiment was well-trained in all possible system dynamics, but he was not provided with any prior information about the specific dynamics or given any indication of when a failure might occur. Each run of the experiment lasted three to four minutes, during which the failure was introduced randomly at some point within the run.

Figure 2.9 shows the results of one of the test runs, TF is the time of failure when the change in controlled element dynamics happens. During the aforementioned run, both feedback loops failed. Both trajectories in the experiment rapidly cross the first decision region (DR-1) and also pass the second decision region (DR-2) on their way back, resulting in the reduction of both system error e and system

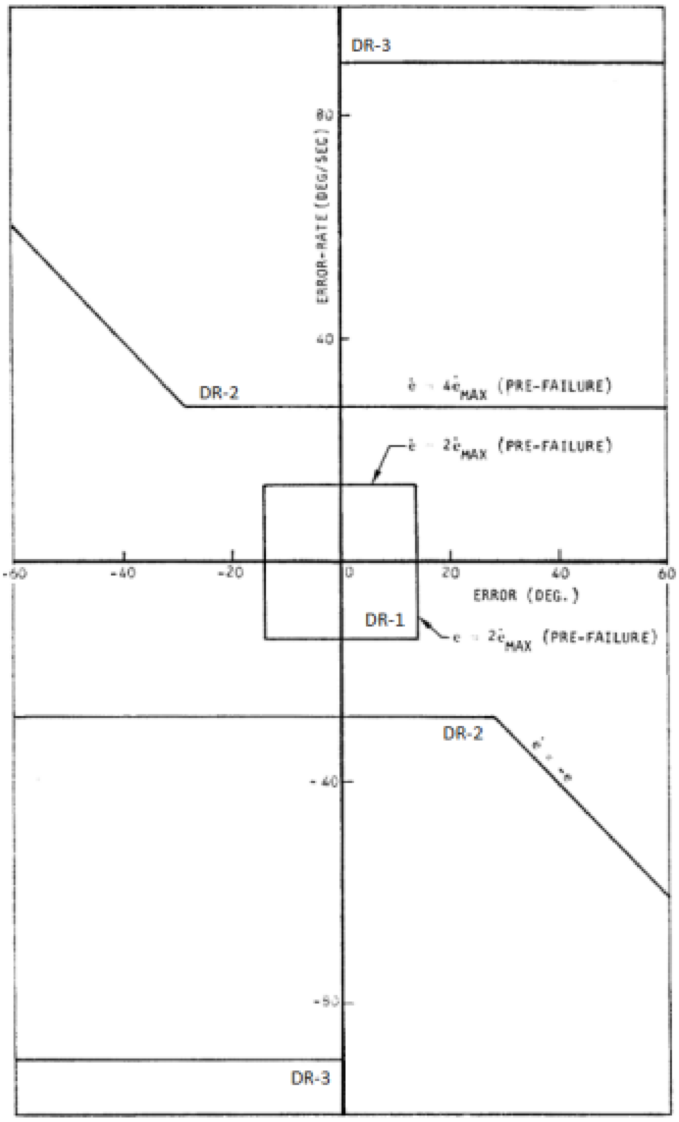

Figure 2.8: Decision regions in the model of Phatak and Bekey Fig 5. [14].

error rate $\dot{e}$ to zero. This trajectory pattern aligns with expectations, as the operator model is adjusted to accommodate the controlled dynamics without the need for an augmentation system.

However, after the second change of sign of the system error rate $\dot{e}$, discrepancies arise between the model and experimental data. This discrepancy can be attributed to the model being a more optimal controller compared to a human operator, leading to a slightly higher delay in human responses. Additionally, the stochastic nature of human responses to failure further complicates the analysis. Consequently, further experiments are necessary to draw conclusive insights regarding the validity of the model.

2.2.5. Van Ham experiment on validation the supervisory control algorithm

Van Ham [15] focused on validating the supervisory control algorithm of Phatak and Bekey [14], their model aimed at understanding human adaptive control behaviour in response to sudden changes in controlled element dynamics. The model uses binary decision moments based on ssystem error e and system error rate $\dot{e}$ signals at specific decision region limits [14]. Van Ham [15] conducted an experiment at Delft University of Technology involving six participants tasked with a compensatory pitch tracking task with change in controlled element dynamics. The participants were instructed to press a button once they

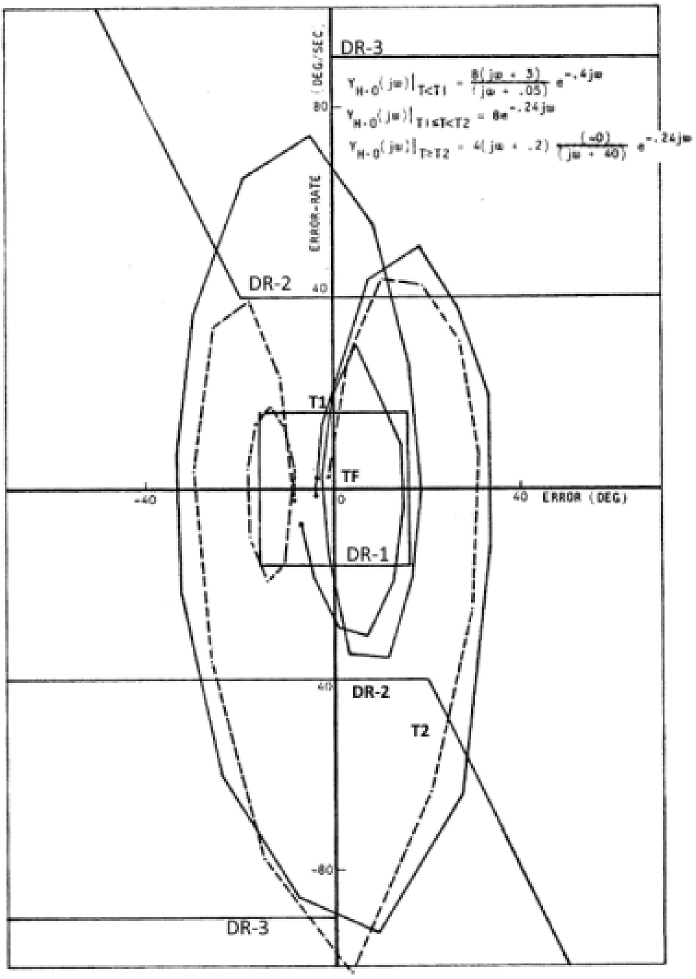

Figure 2.9: The dashed line is the model and the solid line is the experimental data of a run during the experiment of Phatak and Bekey Fig 15. [14].

detected a change in controlled element dynamics. The key finding from this experiment is that the original decision region limits (DR-1) proposed by the supervisory control algorithm do not align with how human operators adapt in this specific task, as only one detection, when the participant pressed the button, fell outside the proposed decision region limit (DR-1) [15].

Decision region one (DR-1) is bounded by $2|\dot{e}_{max}|$, which corresponded to 18 σ system error e and 9 σ system error rate $\dot{e}$ of the pre-failure steady-state tracking in the experiment. To address this mismatch, Van Ham explored new detection limits based on standard deviations of system error e and system error rate $\dot{e}$ in the pre-failure tracking data [15]. The research suggests that a detection limit of around 3.9σ of the system error e or system error rate $\dot{e}$ yields more realistic results [15]. Interestingly, both the individual standard deviation and average standard deviation produced similar outcomes, indicating the potential for a universally applicable detection limit [15]. This finding challenges the initial assumptions made in the supervisory control algorithm.

Van Ham highlights the importance of training participants thoroughly in recognizing and adapting to different controlled element dynamics [15]. It also acknowledges the subjectivity of button press data as a detection method and suggests separating tracking and detection tasks for better results. Additionally, Van Ham emphasizes the need for a more realistic pilot model in control input analysis and suggests combining binary decision models with continuous modelling for a more comprehensive understanding of human adaptation [15].

The findings reveal discrepancies between the algorithm's predictions and actual human behaviour, prompting the exploration of new detection limits based on standard deviations [15]. The study also underscores the importance of participant training, the subjectivity of detection methods, and the potential for more complex modelling to enhance the understanding of the human adaptive control process.

2.2.6. Niemela and Krendel detection time of changes in controlled element dynamics

Niemela and Krendel [16] wanted to better determine and understand the detection time of a human operator during a change in controlled element dynamics. To come up with a model for this they started doing two-minute compensatory tracking tasks experiments. The participants had to track a low-pass filtered white noise target function f_t with a statistical bandwidth of 1.5 rad/s with double integrator-like controlled element dynamics. During the task, the controlled double integrator controlled element dynamics would suddenly experience a polarity switch. Niemela and Krendel [16] also experimented with auditory cues when the system error e and system error rate $\dot{e}$ would pass predetermined boundaries.

During the run without the auditory cue, it was clear that after detection the system error e would increase significantly as also found by [2, 8, 14]. For some of the participants, the system error e and system error rate $\dot{e}$ did not get out of bounds, caused by the system error rate $\ddot{e}$ pushing the system error e back into the bounds, here the participants did not notice the change in controlled element dynamics. The experiments yielded the same results and conclusion as previous experiments [8, 14], that the detection was only done when the system error e and system error rate $\dot{e}$ were relatively large. Niemela and Krendel [16] found that the subjects did not detect the change in controlled element dynamics if both the system error e and system error rate $\dot{e}$ were not of the same sign.

During the second run with the auditory cues, the detection boundaries were determined. Niemela and Krendel [16] would vary the time of the auditory cue to determine when it would be useful and reduce the average peak system error. The alert was useful when the human did not detect the change yet and the average peak system error would be lower. When the participant had already detected the change the alert would not be useful in reducing the average system peak error. The boundaries in Figure 2.10 are based on the root mean square steady-state system error e and system error rate $\dot{e}$ and show left when the auditory cue was useful and right when it was not in lowering the average system peak error.

The transition region for detection is in between the shaded shape of the left and right graph in the Figure 2.10. Therefore, the peak system error and peak system error rate would be decreased when the system error e or system error rate $\dot{e}$ would be below 1 σ steady-state tracking system error e or system error rate $\dot{e}$ after a change in controlled element dynamics happened. When the system error e or system error rate $\dot{e}$ would be larger than 3 σ steady-state system error e or 2 σ steady-state system error rate respectively then the peak system error and peak system error rate would not be decreased because the subjects had already detected the change in controlled element dynamics. The detection of the change in controlled element dynamics for the experiments of Niemela and Krendel [16] happens system error e and system error rate $\dot{e}$ move outside the steady-state tracking regions, so at the boundary where the auditory cue would not help decrease the peak system error and peak system error rate.

2.2.7. Compensatory tracking conclusion

The studies focus on compensatory tracking tasks. The pioneering work by Young et al. laid the foundation for understanding the principles of adaptive manual control, with a focus on controlled element adaptation. Miller and Elkind extended this understanding by delving into the detection, identification, and modification phases of human adaptation in tasks involving single integrator-controlled elements. They proposed a model assuming that humans have an internal model of the controlled element dynamics and when their innovation signal, the difference between the observation of the system error e and their expectation of the system error $\widehat{e}$, exceeds steady-state tracking threshold then the human controller will detect the change in controlled element dynamics.

Weir and Phatak's research explored optimal control strategies during transitions, emphasizing rapid adaptation in unstable scenarios following system failures. Phatak and Bekey introduced a sequential identification model with decision control logic. Van Ham's research challenged the existing supervisory control algorithms by proposing new detection limits based on standard deviations of the system error e and system error rate $\dot{e}$. Niemela and Krendel emphasized the significance of system error e magnitude and system error rate $\dot{e}$ in human operator detection of changes in controlled element dynamics.

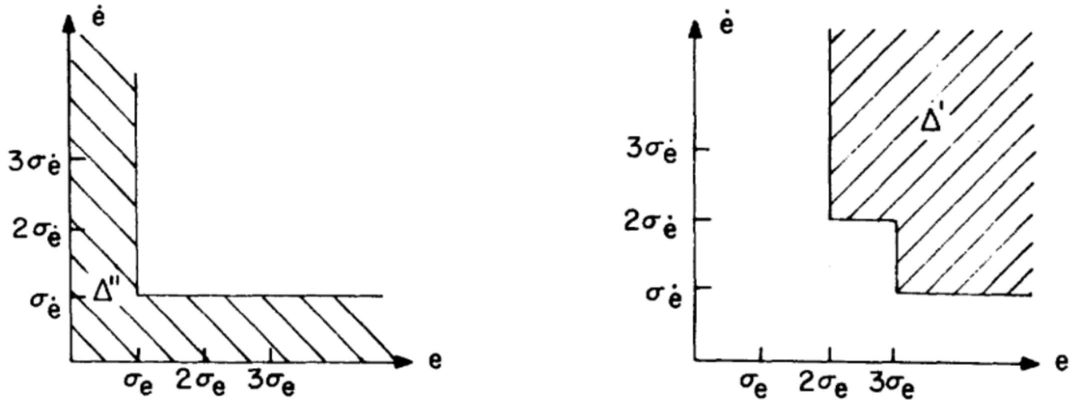

Figure 2.10: Auditory cue boundaries which in the left graph would decrease the average system peak error and right would not decrease it [17].

Most researchers use the fact that humans have some sort of expectation, where when the system error e and system error rate $\dot{e}$ exceeds the difference between their expectation and observation a change in a controlled element must have happened. A human can consciously or subconsciously adjust their control behaviour, following an exceeding of the steady-state tracking threshold. The human adaptive process is quick, however, detection sometimes takes quite a long time or does not even happen. However, most of the models do have their limitations and do not carry over to pursuit tracking due to compensatory being a feedback-only display. The models do shed insight into the human adaptive process and some of the lessons learned can be carried over to pursuit tracking models. These studies collectively contribute to our understanding of how humans adapt to dynamic changes in compensatory tracking tasks. They also validate certain models and highlight the importance of training and complex modelling approaches in improving our grasp of human adaptation in control systems. However, these models do not carry over to pursuit displays and most of the real-world tracking is done on pursuit displays. Therefore, new models had to be theorised to adapt to this display.

2.3. Adaptive manual control models for pursuit displays

In this section, some preceding models that guided as inspiration for the model of Mulder et al. will be explained. The model of Mulder et al. for human adaptation will be explained to get a better understanding of the expectations of human controllers.

2.3.1. Frith et al. model

Frith et al.'s [18], came up with the comparator model, which is a conceptual model used to explain possible processes in the brain and body of a human controller. Mulder et al. [5] adapted the model to apply to a pursuit display see Figure 2.11. The comparator model includes components assumed to be working together in the body and brain of the human controller, as in the end moving your hand is a means to an end [5]. In the model, the human controller, based on a desired state (the function to be tracked for example), uses an inverse model to generate a motor command to the arm to move the stick [18].

Frith et al.[18] model does not have a disturbance signal acting on the controlled element, so the actual state the human controller outputs is the reafference (defined as 'the effect on an organism's sensory mechanism due to the organism's own actions', according to Mulder et al. [5]). If there were a disturbance working on the controlled element then the perceived state would be both the reafference and the exafference (defined as 'the effect on an organism's sensory mechanism due to factors external to the organism', according to Mulder et al. [5]).

So the input to the central nervous system thus is the reafference and the exafference combined [18, 5]. The inverse model should include both the dynamics of the human controller and the controlled element because the human wants to track the desired state, therefore, the desired state minus the actual state

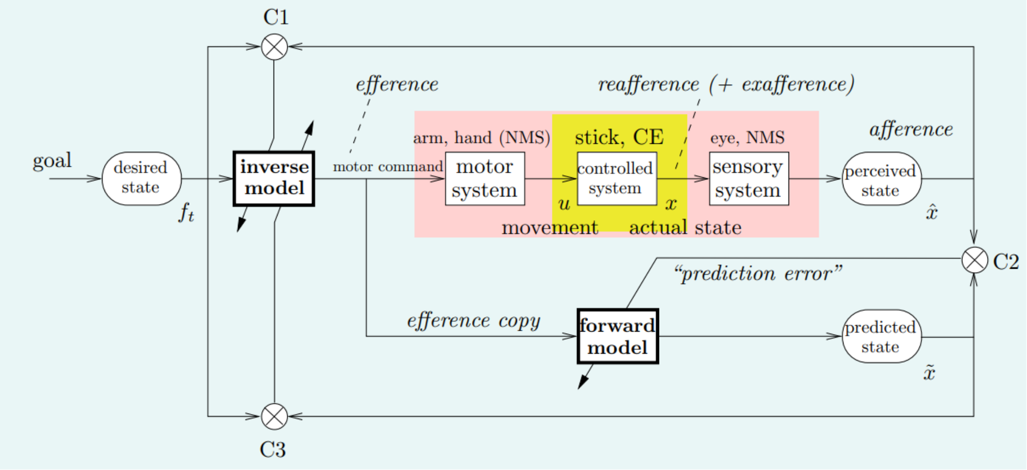

Figure 2.11: Comparator model, interpretation of (Frith et al.), adapted to pursuit tracking. The CE is the Controlled Element, NMS for the Neuromusculoskeletal system and C1, C2, and C3 for the three 'comparators' (Mulder et al., figure 2 [5]).

should be zero $e = f_t - y$ [5].

The first comparator C1, see Figure 2.11, compares the difference between the perceived state and the desired state. This comparator is used to improve the performance of the inverse model. A copy of the motor command, the efference copy is sent to the forward model, which is used to predict the consequences of the action of the motor unit [5]. The forward model is the inverse of the inverse model, it also includes both the dynamics of the human and the controlled element.

The second comparator C2 compares the predicted state with the perceived state and the difference is used to update the forward model [5]. The C2 error is how the central nervous system disentangles the effects on the controlled element due to the human controller and the exafference [5]. The third comparator C3 compares the predicted state with the actual desired state. The error is used to update the inverse model.

The model poses some issues from an engineering sense. Firstly, there is no feedback loop, it does have error loops, but nothing that feeds the system error back to the system. Secondly, the inverse and the forward models seem to be separate models and updated by two different comparators even though both have the same dynamics as discussed earlier in this chapter. Lastly, the prediction error only updates the forward model and not the inverse model, again, even though they have the same dynamics.

2.3.2. Neilson et al. model

Neilson came up with the adaptive model theory, which is a term used for the research conducted by Neilson and his team [5]. It is defined by Neilson et al. [19] as "A computational theory of the information processing performed by the human nervous system in control movement". Neilson et al. model [19] is characterized by a three-stage model of movement. The stages are:

- Sensory analysis
- Response planning
- Response execution

These stages, as proposed by Neilson et al. [19], run sequentially, in parallel and independently from each other communicating through memory buffers. Neilson et al. model is adjusted by Mulder et al. to get to Figure 2.12 [5]. The model is adaptive and alters its behaviour with changes in the controlled element dynamics, variations of the statistical properties of the target and disturbance signal [19]. Neilson et al.'s [19] model, still has the inverse and forward model as proposed by Frith et al., it also still has the efference and afference copies.

The sensory system is omitted in the model and the human controller output and the input, which now has a disturbance element, are known by the human controller. Also, the comparator C3 is no longer

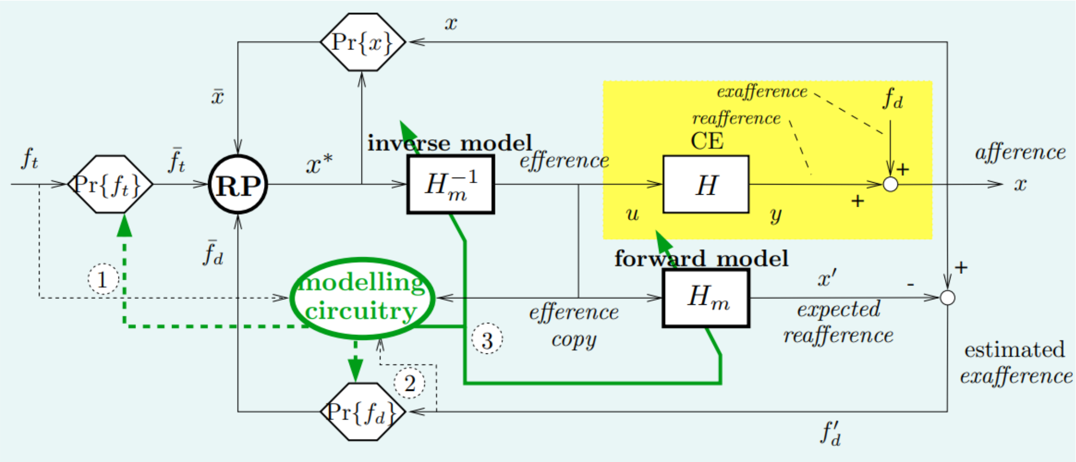

Figure 2.12: Neilson et al. model adjusted by Mulder et al. (Mulder et al., figure 3 [5]). RP stands for Response Planning, and CE for controlled element.

existing in this model. Comparator C2 now compares the expected reafference with the afference and feeds, unlike in the Frith et al. model, the difference back into the modelling circuitry [5]. One, Two, and Three are adaptive self-tuning filters [19]. One and Two are driven by the autocorrelations of these signals to generate the predictions [19]. Three is filtered automatically to maintain an accurate internal model of the controlled element and the human controller [19].

According to Neilson et al., [19], ”any change in the dynamic response characteristics of the tracking system H leads to an automatic adaptive retuning of the forward model H_m and of the inverse model H_m^{-1} employed using response execution”. This model was used to mimic experimentally measured human controller behaviour, which proved to successfully show the effects of adaptation to controlled element dynamics, and prediction of target and disturbance signals [5]. Neilson et al. model does not include any neuromuscular dynamics, and the model needs more neurobiological data for proper verification [19].

2.3.3. Hess model

Hess [20] developed a model of adaptive human pilot control for multi-axis tracking. He based his model on previous research on human behaviour in loss-of-control situations [21, 22, 23]. Hess [20] used a pursuit display where the pilot used both the system output y and the output rate $\dot{y}$ to perform the tracking task. Figure 2.13 is an adjusted schematic overview to fit the nomenclature used in this literature study of the model where K_p is the pilot gain in the position loop and K_r the pilot gain in the rate loop, H_{nm} are the neuromuscular dynamics of the pilot and H_c is the controlled element dynamics. The adaptive logic is there to update the two gain terms (K_p, K_r) once a change in controlled element dynamics is detected. This adaptive logic uses the system output rate $\dot{y}$ and the desired rate of change r. The core principle of this model revolves around the idea that adaptation primarily takes place through alterations in the gain of the inner loop (K_r). On the other hand, fine-tuning the overall performance is better achieved by modifying the gain of the outer loop (K_p).

Hess [20] outlined four guidelines for the model. The first guideline is that K_p and K_r, the inner and outer loop gains, have to stay within realistic bounds for human controllers. The second guideline is that the detection of a change in the controlled element dynamics can only occur based on the system error e and system output rate $\dot{y}$. The third guideline uses the crossover model of McRuer [3], in which the pre-and post-transition operator parameters are in line with the crossover model. The fourth and final guideline is that adaptation occurs relatively shortly after detection by the human operator of the change in controlled element dynamics.

The detection and then adaptation happens in the adaptive logic block of the model. According to Hess [21], changes in the inner loop gain K_r are hypothesized to be caused by sensed changes in the sign and magnitude of $r - \dot{y}$. So the change in controlled element dynamics is detected due to the human controller sensing a change in the difference between the system error rate $\dot{y}$ and outer loop gain $r = eK_p$ and the

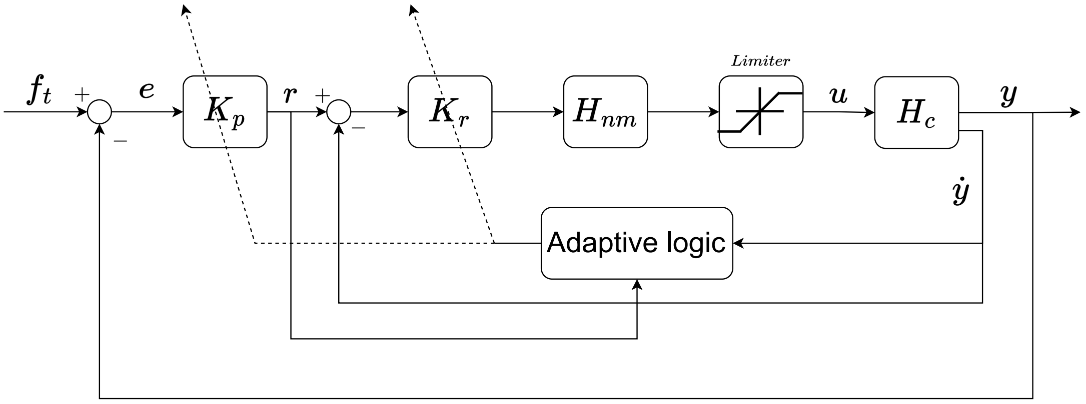

Figure 2.13: Hess' simplified model of adaptive human control in pursuit display [20], adjusted for the nomenclature used in this literature study.

system output rate $\dot{y}$. Equation 2.11 [20] is the signal perceived by the human in the adaptive logic to use as a criterion in Equation 2.12 [20] to determine if adaptation is necessary. The signal has a second-order filter which is the way the human smoothes the function and introduces a lag. The decision logic uses the square root of the signal with a comparison if the square root is smaller than 3 times the root of the mean square of the signal during previous tracking without a transition. In the decision logic, t_c is the time of transition and t_s is a small time value to not take the run-in time into account [21].

$$x = sgn\left\{|r| - |\dot{y}|\right\} \cdot \left[|r| - |\dot{y}|\right]^2 \cdot \left(\frac{1.5^2}{s^2 + 2(1.5)s + 1.5^2}\right) \tag{2.11}$$

$$K_{trigger} = \begin{cases} 0 & \text{if} \quad \sqrt{|x|} < 3 \cdot \left[\overline{\sqrt{|x|}}\right] \quad \text{or} \quad t < t_c \\ 1 & \text{if} \quad \sqrt{|x|} \geq 3 \cdot \left[\overline{\sqrt{|x|}}\right] \quad \text{or} \quad t \geq t_s \end{cases} \tag{2.12}$$

The change in the inner loop gain is given in Equation 2.13 [20]. The x_n term is given by Equation 2.14 [20] and is a normalised and filtered version of the signal. There is again a second-order filter to simulate human smoothing and lag. In the equation N is the number of variables the human operator is controlling, this is used because a human operator will control less aggressively when there is multi-axis control [23].

$$\Delta K_r = x_n K_{trigger} \frac{1.5^2}{s^2 + 2(1.5)s + 1.5^2} \tag{2.13}$$

$$x_n = \frac{x}{rms\left[r^2\right]} \frac{1.5^2}{s^2 + 2(1.5)s + 1.5^2} \frac{1}{N} \tag{2.14}$$

The outer loop of the model is then adapted by using the decision logic of Equation 2.15 [20]. According to Hess [20], when K_r is reduced this does not mean the stability of the systems is compromised, so K_p does not necessarily be changed. However, when K_r increases the phase margin might become smaller and K_p has to be adjusted to stay within acceptable phase limit bounds. Both K_p and K_r cannot exceed 2 and 10 times their original value respectively [20].

$$\Delta K_p = \begin{cases} 0.35\Delta K_r & \text{if} \quad \Delta K_r > 0 \\ 0 & \text{if} \quad \Delta K_r \leq 0 \end{cases} \tag{2.15}$$

2.3.4. Experimental validation of Hess' model

Jakimovska aimed to evaluate and validate the ”adaptive pilot model” proposed by Hess [24]. The research utilized experimental data obtained from a pursuit tracking task. In this task, participants were tasked with tracking a moving target, which served as a surrogate for a controlled system with dynamics that varied over time. These dynamics of the controlled element (CE) were intentionally manipulated to transition between a single integrator system (DYN1) and a double integrator system (DYN2).

The initial step of the analysis involved a meticulous examination of the inner- and outer-loop gain settings that participants require to effectively control the system in both the pre-transition (DYN1) and post-transition (DYN2) phases. The findings of this analysis reveal a critical observation: as the system transitions from DYN1 to DYN2, participants need to reduce their gain K_p and increase the rate gain K_r [24]. This adjustment aligns with theoretical expectations, as double integrator CE dynamics necessitate more lead (increased K_r) and reduced low-frequency response magnitude (reduced K_p) [24].

However, it's crucial to note that the existing adaptive model logic, as outlined in prior research, can only account for increases in human operator control gains. This realization underscores the necessity to adapt the model's logic to accurately capture scenarios where not only post-transition human operator gain increases are expected but also reductions [24]. This is essential for accurately modelling human behaviour in dynamic control systems.

The second step involved the process of fitting the adaptive pilot model to the experimental data collected from participants. The primary goal was to establish how well the model could replicate human behaviour under these dynamic conditions. The analysis revealed interesting insights: the model is highly successful in modelling the data for DYN1 conditions across all participants. However, it encounters considerable challenges when attempting to achieve a satisfactory fit for the DYN2 conditions, particularly for three of the participants.

To evaluate the model's performance, a metric known as Variance Accounted For (VAF) was utilised. This metric provides a measure of how well the model aligns with the experimental data, with average VAF values of 0.63 for DYN1 and 0.5 for DYN2 conditions [24]. It's worth noting that in previous experiments, a different human control model achieved higher VAF values for DYN2 data compared to DYN1 data. This suggests that there is room for improvement in the adaptive pilot model to better capture the dynamics of human control behaviour in these scenarios.

The third step delved into a detailed analysis of the model's sensitivity to key parameter settings. A significant enhancement introduced to the model is the inclusion of a human time delay (τ_e). This delay represents the lag in human perception and response. Notably, the analysis demonstrated that adding a time delay of 0.2 seconds substantially improves the model's ability to match the experiment data [24].

Moreover, the researchers investigated how this added time delay affects the adaptive Triggering and Adaptation mechanisms within the model. While the delay's impact on triggering is relatively minor, it substantially influences the magnitude of modelled gain adaptations. To address this, the researchers propose introducing ”adaptation constants” (K_{a_r} and K_{a_p} as additional parameters to fine-tune the model's response [24].

Crucially, these adaptation constants would need to be individually selected for each participant, similar to how the proportional and rate gains (K_p and K_r) are customized. The ultimate aim is to attain a closer alignment between the model's predictions and the actual changes in gain observed during CE transitions, improving the model's predictive accuracy.

Additionally, the analysis involved an examination of the low-pass filters integrated into the model's adaptive logic [24]. These filters are essential for accounting for delays in human detection and parameter adjustments. For example, three different second-order low-pass filters were applied to the x-signal ($H(s)$), the x_n signal, and the ΔK_r signal ($J(s)$). The analysis highlighted the significance of tuning the break frequency of the $H(s)$ filter, as it significantly affects the model's adaptive logic [24]. The proposed break frequency of 1.5 rad/s is deemed too low for certain CE transition scenarios, particularly for participants with a low crossover frequency ω_c. Consequently, the break frequency of $H(S)$ emerges as a crucial parameter that may require adjustment to enhance the model's adaptive capabilities in different CE transition scenarios [24].

The fourth and final step entailed the validation of the adaptive pilot model using data from all participants in various time-varying conditions, namely DYN12 and DYN21. For DYN12, the model demonstrates effectiveness in replicating human adaptation behaviour when transitioning from a single integrator to a double integrator system [24]. However, an intriguing observation emerges: the model's triggering mechanism's reliability is highly contingent on participants' pre-transition crossover frequencies. It activates most consistently for participants with higher crossover frequencies, which can reach up to 1.5 rad/s. In contrast, for participants with lower crossover frequencies below 0.9 rad/s, the triggering mechanism often remains inactive, even with parameter adjustments [24].

In the case of DYN21, where the transition was from a double integrator to a single integrator system, the adaptive pilot model struggles to predict human adaptation effectively [24]. This challenge arises because the transition to more stable dynamics does not negatively impact tracking performance. Consequently, the model's adaptive logic remains dormant, and significant adaptation does not occur.

The research concluded that while the adaptive pilot model exhibits promise in simulating human adaptive control behaviour, it is not without its limitations [24]. To enhance its accuracy and applicability, further research and experimentation are essential. Key areas for improvement include considering individual-specific parameters such as neuromuscular dynamics and time delay, refining the model's triggering mechanism to accommodate a broader range of CE transitions, and potentially exploring structural extensions to the adaptive logic to account for other factors like changes in control activity or phase margin.

2.3.5. Model Reference Adaptive Control for Modeling Human Adaptive Control Behavior

Model Reference Adaptive Control (MRAC) is a control technique that integrates an internal reference model [25]. This internal model serves as a reference for desired system performance. MRAC then adapts control parameters based on discrepancies between the internal model's predictions and the actual system behaviour. It is widely used in control engineering due to its adaptive nature, allowing it to handle dynamic variations effectively [25].

Researchers have explored MRAC's effectiveness in capturing steady-state control behaviour exhibited by human operators [25]. In experiments simulating controlled element dynamics transitions, MRAC achieved median Variance Accounted For (VAF) values of the control output u of 0.64 for certain conditions [25]. While slightly lower than other models, the adaptive nature of MRAC still provided satisfactory predictions of human control behaviour under steady-state conditions.

MRAC's applicability extends to predicting transient control adaptation during dynamic changes in controlled systems [25]. When the system transitions from a less stable dynamic (approximating a single integrator) to a more stable dynamic (approximating a double integrator), MRAC effectively matches human control behaviour [25]. In this scenario, significant discrepancies between the reference model and the control loop enabled MRAC to provide accurate predictions [25].

However, MRAC faced challenges when predicting human adaptation in the inverse transition, where the system shifted from a double integrator to a single integrator dynamic [25]. In this case, MRAC's predictive accuracy dropped significantly. This limitation stemmed from the model's slower adaptation in scenarios with smaller prediction errors due to transitions to more stable dynamics [25]. The current implementation of MRAC utilizes a fixed internal reference model. While suitable for modelling adaptation to achieve invariant open-loop system dynamics, it does not account for cases where open-loop dynamics parameters change [25].

MRAC, while valuable, provides only a limited perspective on human adaptive control behaviour [25]. More advanced approaches like ”model-based optimal control” or ”inverse reinforcement learning” may be necessary to capture the complexity of human control strategies in various dynamic settings. These approaches can potentially model intricate control behaviours observed in tasks such as obstacle avoidance, open-loop planning, and adapting to diverse disturbances [25].

Model Reference Adaptive Control (MRAC) offers a promising framework for modelling human adaptive control behaviour in response to dynamic changes in controlled systems. While it demonstrates success in certain scenarios, MRAC faces limitations, particularly in inverse transitions [25]. The inclusion of control effort prediction errors and the exploration of adaptive internal models hold promise for enhancing MRAC's predictive capabilities [25]s. Additionally, more advanced modelling techniques may be required to fully capture the richness of human control strategies in complex dynamic settings. Further research in these directions can significantly contribute to our understanding of human-machine interaction and control system design.

2.3.6. Mulder et al. model

Mulder et al. [5], proposes an adjusted model of Nielson et al.'s adaptive model theory. The new model incorporates the concept of internal representation of task variables. The model works by assuming that proficient human controllers detect changes in task variables because their expectation, in the internal representation, does not line up with their observation [5]. Therefore, the proficient human controller can deduce the statistical properties of the target signal, the disturbance acting on the system and possible changes in the controlled element dynamics [5, 19].

The human controller creates an innovation signal due to the difference from what he/she expects with different control outputs of the controlled element [26]. Therefore, the changes noticed between the two trigger adaptations in the control behaviour of the human and their internal representation given in the feedforward and feedback models [26]. There will also be physiological changes in the neuromuscular system of the human [27]. The complete model is given in Figure 2.14 [5].

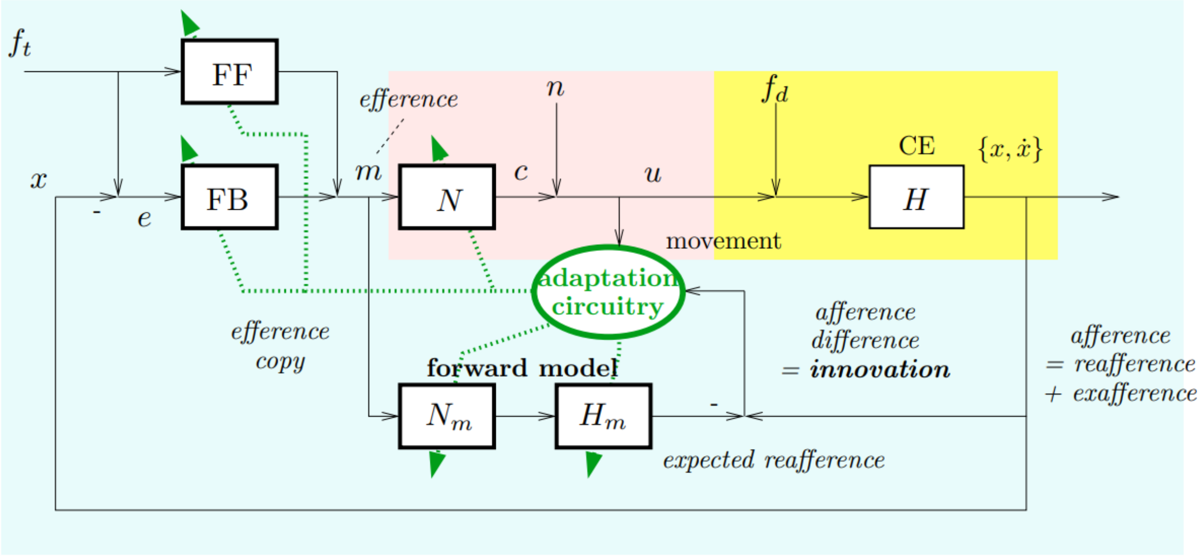

Figure 2.14: Mulder et al. readjusted model based on the adaptive model theory of Nielson et al. (Mulder et al., figure 4 [5]).

According to Mulder et al., [5, 26], a human controller will predict the target signal f_t and adapt their internal representation using the statistical properties of this target signal. Magdaleno et al.[28], Drop et al. [29] and Mulder et al. [30], can be used to come up with nonlinear human controller pursuit tracking strategies.

Furthermore, the feedforward and feedback scheme, used in both the neuroscience work of Wolpert et al. [31] and the cybernetics work of Drop et al. [29], is adopted. Van der El. [26] used a simpler scheme without the feedforward path based on the inverse controlled element dynamics.

2.4. Conclusion literature study

A series of studies have explored models of human adaptive control behaviour in compensatory and pursuit-tracking tasks. Many of the lessons learned for compensatory tracking were carried over into the work on pursuit-tracking tasks. Frith et al. introduced the comparator model, adapted by Mulder et al. for pursuit tracking. This model involves an inverse model generating motor commands based on a desired state. Neilson et al. developed an adaptive model characterized by three stages: sensory analysis, response planning, and response execution, with a focus on communication through memory buffers. Hess proposed a model for adaptive human pilot control in multi-axis tracking, emphasizing the adjustment of inner and outer loop gains upon detecting changes in controlled element dynamics.

The adaptive pilot model, however, faces challenges in accurately modelling human behaviour during CE transitions. Jakimovska attempted to validate the model and identified areas for improvement. The model exhibited success in some scenarios but struggled in others, particularly when transitioning to more stable dynamics. Key findings include the need to adapt the model's logic to account for both gain increases and reductions in human operator control, the introduction of a human time delay, and fine-tuning adaptation constants. Additionally, the model's triggering mechanism's reliability depends on participants' pre-transition crossover frequencies. Overall, while these models offer valuable insights into human adaptive control, further research is necessary to refine and extend them, considering individual-specific parameters, improving triggering mechanisms, and exploring structural extensions to enhance accuracy and applicability.

Model Reference Adaptive Control (MRAC) emerged as a promising framework for modelling human adaptive control behaviour, effectively capturing steady-state and transient control adaptation. However, MRAC faces challenges in scenarios with inverse transitions and fixed internal models.

The model proposed by Mulder et al. builds upon previous research and aims to address certain limitations of existing models while incorporating the concept of internal representation of task variables. By introducing the concept of internal representation and considering both feedback and feedforward mechanisms, the model aims to address limitations and provide valuable insights into the complexities of human control behaviour in pursuit-tracking tasks. In control systems, both feedback and feedforward control strategies are combined to achieve robust and effective regulation of a system's behaviour. Feedback control corrects system errors that were not anticipated by the feedforward control, providing a layered approach to control system design.

The models of Mulder et al. will be used to determine the moment a human detects a change in controlled element dynamics. However, the feedforward and feedback models are omitted in the subsequent research, because the detection process itself doesn't rely on these control models. Detecting a change in controlled element dynamics is primarily a function of human perception and cognitive processes. It involves the human controller's ability to sense differences between their internal representation of the task and the actual observed behaviour of the system. The moment a human detects a change, they might not consciously apply feedforward or feedback control mechanisms. Instead, this detection often happens at a cognitive level, where the individual realizes that what they expected or predicted doesn't match what is happening.

Humans have internal models or representations of the task and the controlled element dynamics. These models are not always explicitly related to feedforward or feedback control models. Changes in these internal models trigger the detection of variations in system behaviour. In essence, when discussing the moment a human detects a change in controlled element dynamics, the emphasis is on the cognitive and perceptual aspects of human control rather than the technical details of feedforward and feedback control models. These models are more relevant when describing how humans might respond to such detections or adjust their control strategies in light of changes.

The idea that humans have an expectation was introduced by Miller and Elkind for a compensatory display, they proposed that when a human controller's observation does not match this expectation then adaptation is needed. The innovation signal, which is the difference between human observation and expectation, is used to determine when a change in controlled element dynamics must have occurred when this signal exceeds a steady-state threshold. Mulder et al. expanded on the idea of human expectation and made a model adapted for pursuit-tracking tasks. This innovation signal and steady-state tracking threshold will be used in this research to determine when a human detects a change in controlled element dynamics.

3

Simulations

The model of Mulder et al. is used for further research into the human adaptive process. To determine the moment a human detects a change in a controlled element a threshold for detection in changes of controlled element dynamics must be determined. This will be done by simulating the innovation signal for different target functions and remnant signals. This chapter goes more into depth on the model used to do the simulation, the simulation itself, and the verification of the separate parts of the simulation.

3.1. Controlled element dynamics

For the simulation two different controlled element dynamics are used, a single integrator and a double integrator given by Equation 3.1. These models will first create a statistical threshold, for the difference between human expectation and observation, for normal steady-state tracking. A sigmoid activation function, Equation 3.2, will create a change in controlled element dynamics. Where here P_1 is the initial parameter value, and P_2 is the final parameter value, the time of maximum rate of change is defined by τ and the maximum rate of change by G.

$$H_c(j\omega, t) = \frac{K_c(t)}{j\omega(\tau_c j\omega + 1)} \tag{3.1}$$

$$P(t) = P_1 + \frac{P_2 - P_1}{1 + e^{-G(t-\tau)}} \tag{3.2}$$

The parameters for both single and double integrators-like controlled element dynamics are given in Table 3.1. Figure 3.1 shows the bode plot of the single integrator-like and the double integrator-like controlled element dynamics.

Table 3.1: Controlled element parameters

	K_c $[-]$	τ_c $[\frac{rad}{s}]$
SI	1.5	0.0
DI	5	1.5

3.2. Human operator model

The human operator model for the simulations consists of the human operator dynamics and the human neuromuscular dynamics. The human operator dynamics come from McRuer's crossover model for compensatory tracking [3]. The pilot model consists of a pilot gain, a lead and lag term, and a time delay. The lag term will be zero. Equation 3.3 is used for the pilot model.

$$H_p(s) = K_p \frac{1 + T_l s}{1 + T_i s} e^{-s\tau_e} \tag{3.3}$$

The neuromuscular dynamics model is given by Equation 3.4 [27].

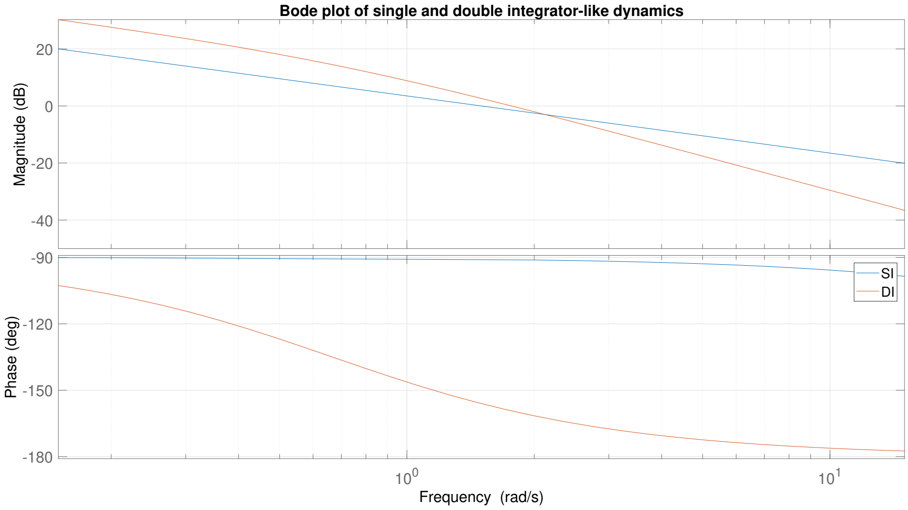

Figure 3.1: Bode plot for the single integrator-like and double integrator-like controlled element dynamics.

$$H_{nm}(s) = \frac{\omega_{nms}^2}{s^2 + 2\zeta_{nms}\omega_{nms} + \omega_{nms}^2} \tag{3.4}$$

Equation 3.5 gives the full human controller model.

$$H_p(s) = K_p\left(1 + T_l s\right) e^{-s\tau_e} \frac{\omega_{nms}^2}{s^2 + 2\zeta_{nms}\omega_{nms} + \omega_{nms}^2} \tag{3.5}$$

Table 3.2 has the values for the pilot model for a single and double integrator. Figure 3.2 show the bode plots for open loop dynamics for the single integrator and double integrator-like dynamics respectively, including the neuromuscular dynamics.

Table 3.2: Human operator values for (**SI**) single integrator and (**DI**) double integrator dynamics.

	K_p	T_l	ω_{nms}	ζ_{nms}	τ_e
SI	1.3	0.0	10.5	0.35	0.26
DI	0.6	1.5	8	0.45	0.3

3.3. Forcing function

In the control task, the human operator tries to accurately track a forcing function f_t. The forcing function consists of a sum of sinusoids represented by Equation 3.6, with different amplitudes A_n, with multiples of the base frequency ω_m, and different phases ϕ_n. The base frequency is the smallest measurable frequency and it depends on the measurement time.

$$f(t) = \sum_{n=1}^{N} A_n \sin(k_n \omega_m t + \phi_n) \tag{3.6}$$

The total simulation time will be 280 seconds of which the first 10 will be discarded to have 3 periods of 90 seconds of identifiable data, the first 10 seconds are needed to give the human controller some time to get to steady-state tracking before the measurement begins. The remaining 270 seconds of identifiable data will be split into sections of 90 seconds to avoid any leakage in the discrete Fourier transform. This ensures that the function repeats itself every 90 seconds meaning the analysis of the different parts of the

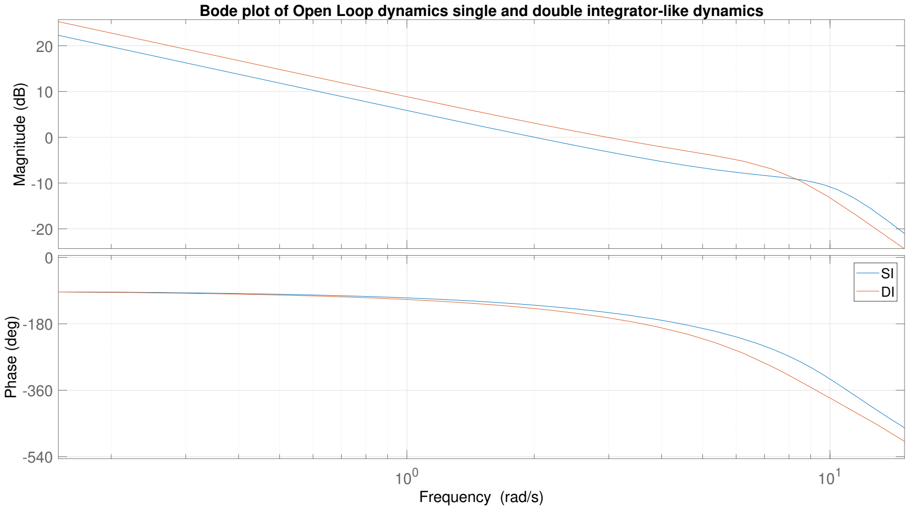

Figure 3.2: Bode plot for the open loop dynamics for the single and double integrator-like controlled element dynamics, including the neuromuscular dynamics.

tracking is easier to do, pre-transition, transition and post-transition tracking. Even though in reality 270 seconds is a very long training run in a simulation fatigue does not play a role. Using Equation 3.7 it can be seen that by reducing the measurement duration, the fundamental frequency rises. Consequently, the actions of a human operator cannot be identified within the extremely low-frequency range. Therefore, with a measurement duration T_m of 90 seconds, the fundamental frequency becomes 0.069 radians per second, still falling well below the crossover range of 1 to 5 radians per second, where human operators exert their control.

$$\omega_m = \frac{2\pi}{T_m} \tag{3.7}$$

For the simulation and determination of the detection thresholds, the forcing function f_t is used with a fixed set of frequencies and amplitudes but the phase shift is randomly altered for the Monte Carlo analysis. Changing the phase of the forcing function during the Monte Carlo analysis helps give the solution more robustness as a larger spectrum of target signals is looked at. The parameters for the forcing function are given in Table 3.3.

Table 3.3: Parameter for the forcing function

n	$k_{n,t}$	$\omega_n\ rad$	A_n [inch]
1	3	0.209	1
2	5	0.349	1
3	9	0.628	1
4	11	0.768	1
5	17	1.187	1
6	27	1.885	1
7	43	3.002	0.1
8	71	4.957	0.1
9	131	9.146	0.1
10	233	16.267	0.1

3.4. Remnant

To model the non-linear part of humans a remnant is used. The remnant is included in the simulations by filtering a zero-mean Gaussian white noise signal using a second-order filter for the single integrator dynamics $(k = 2)$ and a first-order filter for the double integrator dynamics $(k = 1)$, given in Equation 3.8. The remnant is typically represented as an independent noise input signal in the simulations. This approach allows control over how the remnant contributes to the overall control action according to specific needs. Consequently, a systematic examination of the remnant's influence on the parameter identification process can be conducted.

$$H_f(s) = \frac{K_f}{(1 + \tau_f s)^k} \tag{3.8}$$

In the context of this analysis, it is imperative to explore the influence of the remnant signal on control actions within a closed-loop control system involving human operators. The remnant signal assumes a significant role in this analysis as it represents unmodeled behaviour, disturbances, or uncertainties of the human controller that impact the performance of the control system. This influence is important to comprehend as it actively introduces unexpected variations in the system's behaviour when human operators are in control.

To manage the influence of the remnant signal on control actions, a strategy is employed that entails the adjustment of the filter gain (K_f). This adjustment aims to attain fixed and specific power ratios (P_n) for the remnant signal relative to the control signal using Equation 3.9. This process ensures that the influence of the remnant signal remains within acceptable limits and does not affect the analysis of the Monte Carlo analysis by having different remnants' power for every realisation of in the MC.

$$P_n = \frac{\sigma_n^2}{\sigma_u^2} \tag{3.9}$$

A Monte Carlo analysis is conducted, 10,000 different zero-mean Gaussian white noise realisations, to appraise the impact of different power ratios of the remnant signal, spanning from 0.00 (no remnant) to 0.25 in incremental steps, as recommended by Van Zaal [32]. This comprehensive approach enables the evaluation of how fluctuations in the influence of the remnant signal affect the performance of the control system, particularly within the context of interactions with human operators.

3.5. Mulder et al. model

The model of Mulder et al. is built on human expectations. According to the model, a human has an internal model of the task variables. The human controller's internal model consists of the controlled element dynamics, the statistical properties of the target signal and the disturbance signal. The idea behind this model is that a human controller detects a change in the task variables because the expectation obtained from the internal representation does not match their observation. The difference between the human controller's expectation and observation creates an innovation signal. This innovation signal may then trigger adaptations in the internal model of the human controller. These adaptations can be changes in the internal model of the controlled element dynamics or other task variables.

It is important to note that the human controller introduces noise during their control task through the remnant. This noise creates an innovation signal, however, the human controller should be able to recognise this as noise and not adapt their internal model or control strategy based on the innovation signal. Therefore, the human controller must have a threshold for this noise and when the innovation signal exceeds this threshold adaptation of the internal model must take place. It is essential first to figure out what the fluctuation of the innovation signal is caused by. Therefore, a simplified model of the Mulder et al. model is used Figure 3.3. The model omits the inverse dynamics of the Feedforward and Feedback blocks.

To determine what causes this difference firstly both the observation y and expectation y^* have to be determined. The system's output y is given in Equation 3.10.

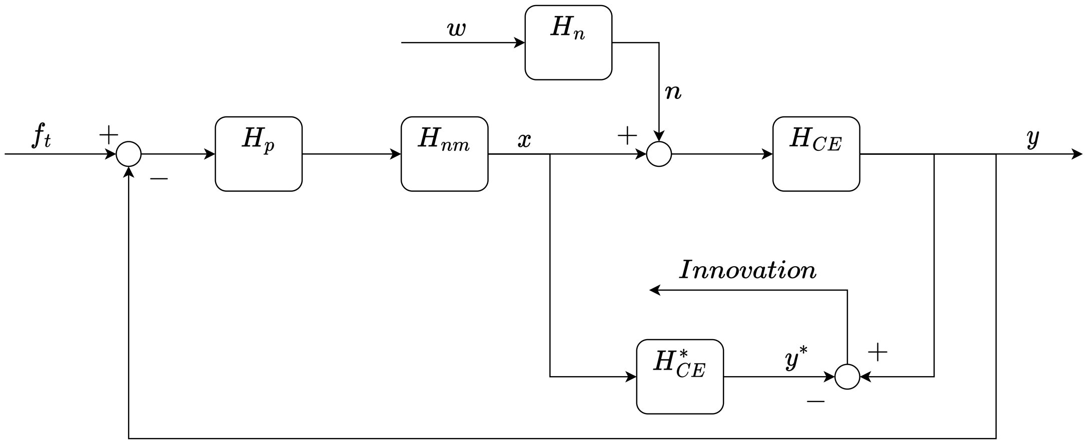

Figure 3.3: Mulder et al. model simplified.

$$y = \frac{H_cH_pH_{nm}}{1+HcH_pH_{nm}} f_t + \frac{H_c}{1+HcH_pH_{nm}n} \tag{3.10}$$

The expectation y^* is given by Equation 3.11. Therefore, the innovation signal $y - \ y^*$ is given by Equation 3.12.

$$y^* = \frac{H_pH_{nm}(H_c^* - H_c)}{1+H_cH_pH_{nm}} f_t - \frac{H_cH_pH_{nm}H_c^* - H_c}{1+H_cH_pH_{nm}} n \tag{3.11}$$

$$\begin{aligned} y - \ y^* &= \frac{H_pH_{nm}(H_c^* - H_c)}{1+H_cH_pH_{nm}} f_t - \frac{H_cH_pH_{nm}H_c^* - H_c}{1+HcH_pH_{nm}} n \\ &= \frac{H_pH_{nm}(H_c^* - H_c)}{1+H_cH_pH_{nm}} f_t - \frac{H_c(1+H_pH_{nm}H_c^*)}{1+H_cH_pH_{nm}} n \end{aligned} \tag{3.12}$$

From Equation 3.12 it can be seen that when the internal representation of the controlled element dynamics H_c^* is the same as the actual controlled element dynamics H_c then the difference is entirely caused by the remnant n. If the internal representation of the controlled element dynamics and the actual dynamics are the same then Equation 3.12 reduces to Equation 3.13.

$$y - \ y^* = H_cH_fw \tag{3.13}$$

This means that the innovation signal of the human controller is entirely caused by the filtered Gaussian white noise, the remnant n, and the controlled element dynamics. Therefore, this relationship can be used to come up with a possible statistical threshold for the adaptation by the human controller.

3.6. Monte Carlo simulations

First, the steady-state tracking innovation signal needs to be determined to determine the thresholds for the detection of a change in controlled element dynamics. To do this a Monte Carlo analysis is done, where for different values of the remnant power the innovation signal is determined. As explained before, keeping the signal-to-noise ratio constant for every run in the Monte Carlo is important. To do this firstly the variance of the control signal u needs to be determined and then using Equation 3.9 the desired variance of the noise could be calculated.

When the noise is zero-mean Gaussian white noise with mean $\mu_w = 0$, and variance σ_w^2 then Equation 3.14 can be used to calculate the variance of filtered white noise with I_n given in Equation 3.15. Where $H_f(\omega)$ is the transfer function of the filter.

$$\sigma_n^2 = WI_n \tag{3.14}$$

$$I_n = \frac{1}{2\pi}\int_{-\infty}^{+\infty} |H_f(\omega)|^2\, d\omega \tag{3.15}$$

W is the intensity of the white noise before the filter, which is σ_w^2. For the single integrator dynamics where the remnant filter is a second-order filter, Equation 3.15 becomes Equation 3.16. Now substituting Equation 3.16 into Equation 3.14 and solving for the filter gain K_f gives Equation 3.17. For the double integrator following the same steps but using a first-order filter and solving for the filter gain gives Equation 3.18.

$$I_n = \frac{K_f^2}{4\tau_f} \tag{3.16}$$

$$K_f = \sqrt{\frac{4\sigma_n^2\tau_f}{W}} \tag{3.17}$$

$$K_f = \sqrt{\frac{2\sigma_n^2\tau_f}{W}} \tag{3.18}$$

This is then used to guess the filter gain K_f. In each iteration of the Monte Carlo simulation, the filter gain is calculated, ensuring constant levels of remnant power to analyse the innovation signal. The Monte Carlo will have 10,000 simulation runs for each of the 5 different noise levels $\begin{bmatrix}0.05 & 0.1 & 0.15 & 0.2 & 0.25\end{bmatrix}$. So for every remnant power, 10,000 zero-mean Gaussian white noise realisations are created and the gain of the remnant filter is then adjusted accordingly to ensure a constant remnant power level. However, the control signal u also has a part of the forcing function and the human operator dynamics in it so the filter gain K_f needs to be adjusted to achieve the required remnant power. This is done interactively by calculating the control signal u and updating the filter gain until the remnant power is within $\pm 1\%$ for the desired remnant power.

The Monte Carlo for no noise will not be run because the innovation signal will be zero. By adjusting the filter gain based on re-calculation of the remnant variance it can be ensured that the signal consistently maintains the desired power level, thus achieving a more accurate and reliable outcome in the Monte Carlo analysis.

3.7. Verification of the different simulation steps

To draw conclusions from the simulation it is important to verify the different components. Therefore, the forcing function and the remnant will be looked at first. Also, the model of Mulder et al. will be checked with zero remnant power to make sure there is indeed no difference between the expectation and observation for that case.

3.7.1. The forcing function

To determine whether the forcing function is implemented correctly it is important to determine whether there is leakage during the 30 seconds intervals. It causes energy from the forcing function's frequency components to spread into neighbouring frequency bins, leading to inaccuracies in frequency analysis, when the frequency of the signal is not an exact integer multiple of the frequency bin spacing. Therefore, a periodogram is made. Figure 3.4 gives the periodogram of the forcing function f_t, from the graph, it can be seen that there is no leakage when the base frequency is $\frac{2\pi}{30}$.

3.7.2. The remnant signal

The verification of the remnant signal in the frequency domain will be carried out by calculating the auto-power spectrum of the filtered noise signal and comparing it to the power spectrum of the analytical model. The power spectral density is presented in Figure 3.5. This graph illustrates that, across the entire frequency spectrum, the power spectrum of the analytical model matches the power spectrum of the filtered noise signal. As a result, we confirm that the implementation of the remnant has been effectively verified. This is done for multiple realisations, however, only the periodogram of one realisation is shown.

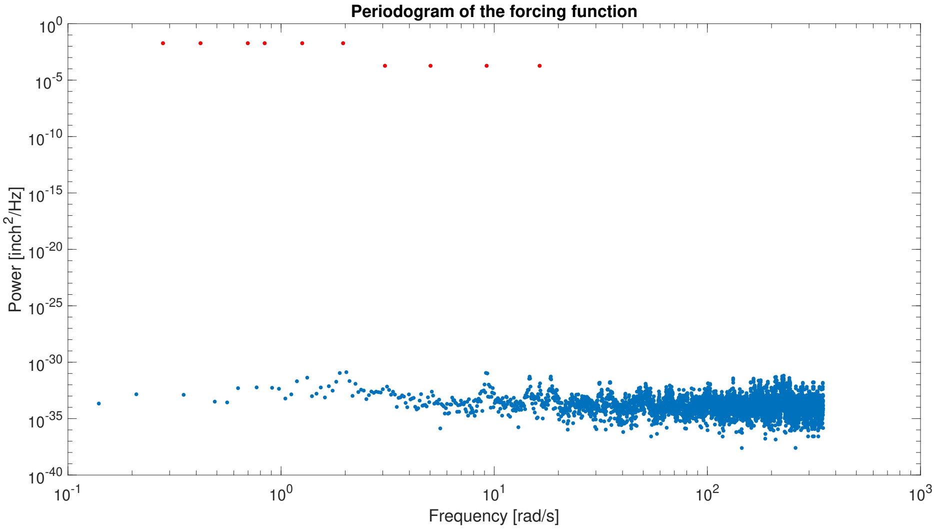

Figure 3.4: Periodogram of the forcing function.

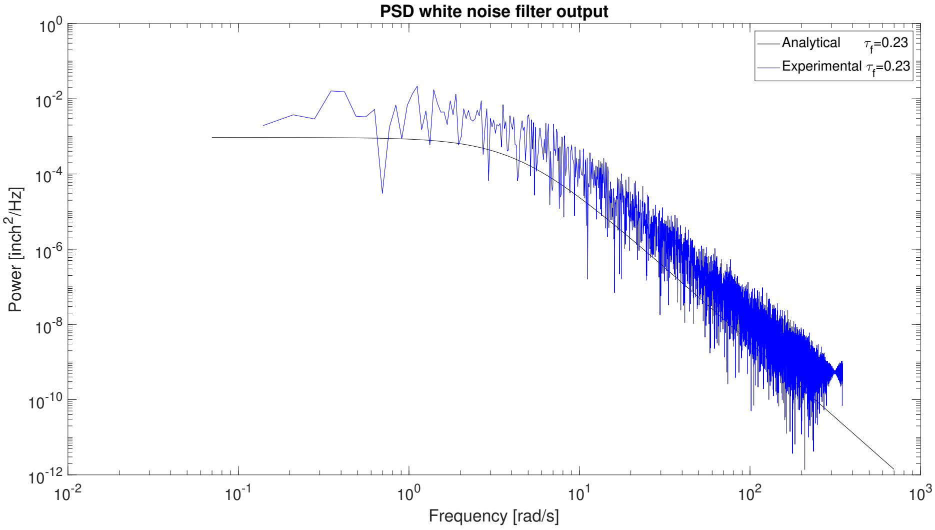

Figure 3.5: Periodogram of the filtered noise, analytically and with MATLAB.

3.7.3. Mulder et al. model

To verify the model of Mulder et al. it is important to first verify that when the internal model and real controlled element model are the same and there is no remnant then the difference between expectation and observation is zero. Figure 3.6 shows indeed that when the remnant is zero then the difference between the expectation and observation is also zero.

A single integrator-controlled element dynamics was chosen with a second-order remnant filter. This is to verify that the implementation of the Monte Carlo analysis indeed returns the expected variance. It is important to note that in the following calculations, there cannot be a pole at zero for the controlled element dynamics. So the single integrator dynamics were chosen to be Equation 3.19. The innovation signal as determined previously is nH_c with n the remnant so the innovation signal is wH_fH_c with w the Gaussian white noise. When the noise is Gaussian white noise with mean $\mu_w = 0$, and variance σ_w^2 then Equation 3.14 can be used to calculate the variance of the system excited by the white noise. To calculate I_n, Equation 3.20 is used [33]. Here $H(s)$ is the transfer function of the system, so $H(s) = H_cH_f$. When working out H_cH_f it can be found that this would be the equivalent to a third-order transfer function, Equation 3.21.

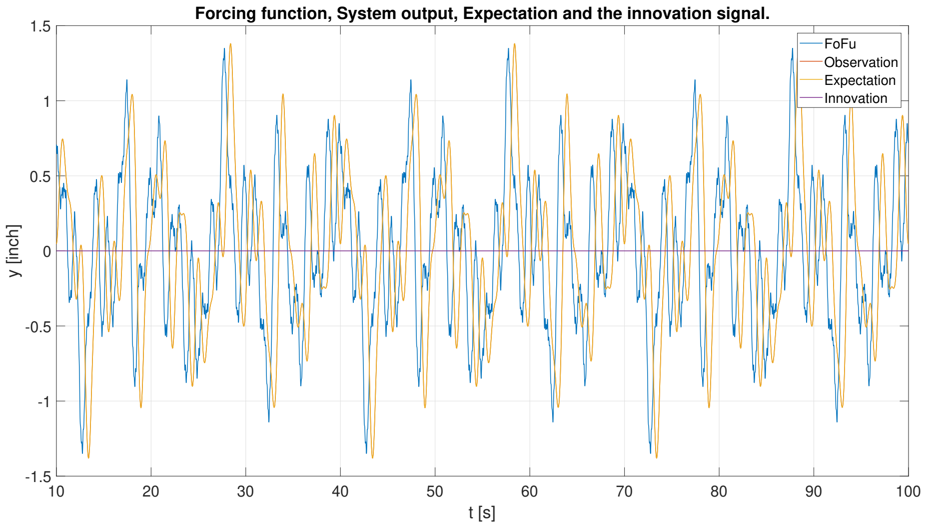

Figure 3.6: The forcing function, the pilot output, the expected output and the innovation signal.

$$H_p(s) \;=\; \frac{K_c}{1+\tau_c s} \tag{3.19}$$

$$H(s) \;=\; \frac{b_0+b_1 s+b_2 s^2+b_3 s^3+b_4 s^4+\ldots+b_{n-1}s^{n-1}}{a_0+a_1 s+a_2 s^2+a_3 s^3+a_4 s^4+\ldots+a_n s^n} \tag{3.20}$$

$$\begin{aligned} H\left(j\omega\right) &= \frac{K_c}{\left(1+\tau_c j\omega\right)}\frac{K_f}{\left(1+\tau_f j\omega\right)^2} \\ &= \frac{K_c K_f}{\tau_c\tau_f^2 s^3+(2\tau_c\tau_f+\tau_f^2)s^2+(\tau_c+2\tau_f)s+1} \end{aligned} \tag{3.21}$$

According to Newland, when H(s) is a third-order system then I_n becomes Equation 3.22 [33].

$$I_n = \frac{a_0 a_3(2b_0 b_2 - b_1^2) - a_0 a_1 b_2^2 - a_2 a_3 b_0^2}{2a_0 a_3\left(a_0 a_3 - a_1 a_2\right)} \tag{3.22}$$

With:

$$\begin{aligned} a_0 &= 1 & b_0 &= K_c K_f \\ a_1 &= \tau_c + 2\tau_f & b_1 &= 0 \\ a_2 &= 2\tau_c\tau_n + \tau_f^2 & b_2 &= 0 \\ a_3 &= \tau_n\tau_f^2 & b_3 &= 0 \end{aligned} \tag{3.23}$$

Using a filter time constant of $\tau_f = 0.23$, a CE dynamics cut-off of $\tau_c = 10$, a CE dynamics gain of $K_c = 1.5$, a remnant filter gain of $K_f \approx 0.054$, remnant power of $P_n = 0.1$ and $W = 1$ the variance of the innovation signal becomes ≈ 0.0096 inch^2. The remnant filter gain K_f was determined by running an MC of 5,000 realisations and calculating the mean value for the remnant filter gain while keeping the remnant power constant at 0.1. The Monte Carlo analysis for the variance of the innovation signal (5,000 realisations) results in Figure 3.7 and shows that the average variance of the innovation signal is around ≈ 0.0936 inch^2. This means that the MC simulation is correctly implemented and thus can be used to determine the steady-state tracking thresholds.

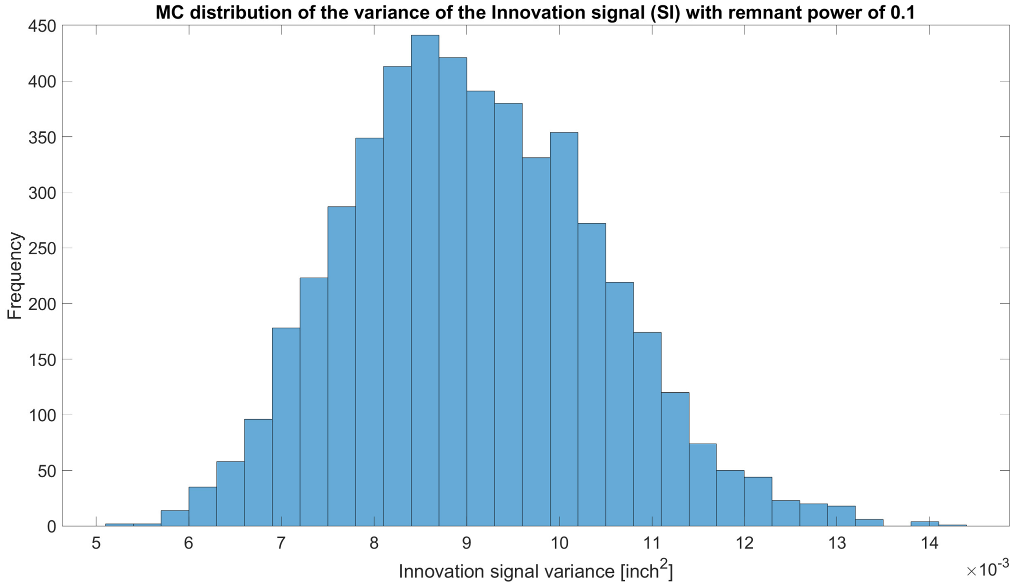

Figure 3.7: MC simulation of the distribution of the innovation signal variance for a single integrator dynamics with a remnant power P_n of 0.1.

3.8. Conclusion simulations

In this research, a comprehensive model is developed and verified to understand how humans detect changes in controlled element dynamics during a control task. Two different controlled element dynamics are used, namely a single integrator and a double integrator, to simulate system behaviour. A statistical threshold will be established to detect changes in controlled element dynamics during steady-state tracking. A sigmoid activation function will then be employed to introduce changes in these dynamics. The human operator model comprises human operator dynamics and human neuromuscular dynamics. The operator dynamics are based on McRuer's crossover model for compensatory tracking, while neuromuscular dynamics are modelled based on existing literature. A forcing function, composed of sinusoidal components with varying amplitudes, frequencies, and phases, is used as the target signal for the control task.

The simulation runs for a total of 100 seconds, with the initial 10 seconds disregarded to allow for the system to reach steady-state tracking. The remaining 90 seconds of data are divided into 30-second segments to analyze different phases of tracking, pre-transition, transition and post-transition. A remnant signal, representing unmodeled behaviour in the human control is modelled as zero-mean Gaussian white noise filtered by a remnant filter. The filter gain is adjusted to maintain a specified power ratio of the remnant signal relative to the target signal. A Monte Carlo analysis is conducted with 10,000 different realizations of zero-mean Gaussian white noise to simulate the innovation signal. The innovation signal, representing the difference between human expectation and observation, is calculated for each Monte Carlo run. Detection thresholds for changes in controlled element dynamics are determined based on the innovation signal's statistical properties. The correctness of the model is verified by examining various aspects, including the forcing function, remnant signal, and the Mulder et al. model's behaviour under zero remnant conditions. Verification ensures that the model accurately represents the desired system behaviour.

The presented model for detecting changes in controlled element dynamics during a control task is constructed and verified. The simulation setup, including controlled element dynamics, human operator models, forcing functions, and remnant signal modelling, is designed to resemble real-world pursuit tracking tasks. The MC of the innovation signal can now be used to answer the research question.

4

Preliminary Results

This chapter will explain the results of the Monte Carlo simulations. Firstly, it will give a more detailed overview of the steady-state tracking simulations. Secondly, the influence of the remnant filter and controlled element dynamics will be explained. Lastly, a conclusion will be given on determining the theoretical thresholds for human detection of changes in controlled element dynamics using the innovation signal.

The process of establishing detection thresholds begins with determining the steady-state innovation signal. This is achieved through a Monte Carlo analysis, where varying levels of remnant power are examined. Maintaining a consistent signal-to-noise ratio or noise power is crucial in every iteration of the Monte Carlo analysis. To achieve this, the variance of the forcing function is initially determined, and then, the desired variance of the noise is calculated. Using this variance the gain factor of the remnant filter can be adjusted accordingly, see Chapter 3.

4.1. Steady-state tracking

During the steady-state tracking, no change in controlled element dynamics is introduced. For the Monte Carlo analysis, the parameters determined in Chapter 3 and a set of power-to-noise ratios are used. The simulation is run for 10,000 realisations for 100 seconds per run, discarding the first 10 seconds to get 90 seconds of data per run. Then for every run, the innovation signal is determined, which is as determined in Chapter 3, nH_c with n the remnant and H_c the controlled element dynamics. The following noise powers are used $\begin{bmatrix}0.05 & 0.1 & 0.15 & 0.2 & 0.25\end{bmatrix}$, for both the single and double integrator dynamics. For both the single and double integrator controlled element dynamics only the noise power of 0.05 and 0.25 are displayed in this chapter, the noise power of 0.15 to 0.20 can be found in Appendix A. Figure 4.1, Figure 4.2, Figure 4.3 and Figure 4.4 give the results for the single and double integrator dynamics, with a noise power of 0.05 and 0.25.

After analysis, see Appendix B, it was found that the distribution of the variances of the Monte Carlo analysis follows a lognormal distribution. The distribution of the means follows a normal distribution.

This means that the distribution of the innovation signal variances is of a multiplicative nature, the impact of the remnant and controlled element dynamics on the output response is proportional and cumulative, leading to amplification or attenuation that scales with the remnant power. This multiplicative effect amplifies or attenuates certain frequency components of the remnant. As the remnant progresses through the system's integrations, its effect accumulates over time. It is clear that the spread of the variability is not constant and is distributed in a skewed manner having long tails meaning a high variability in the variane of the innovation signal.

Table 4.1 gives the values of the mean of the variances of the innovation signal for the Monte Carlo analysis. The mean of the innovation signal offers insight into how the variability of the nH_c's response evolves as the remnant power is increased. It can clearly be seen that the mean of the variances of the innovation signal scales with the remnant power. Meaning a very linear relationship between the remnant power and the innovation signal variance. When the remnant power doubles, the variance of the innovation signals doubles as well. The variance of the DI dynamics is significantly higher than the SI. A possible reason would be that the DI integrates the remnant twice amplifying higher frequencies. The gain of the DI dynamics is also higher than the SI dynamics adding to this amplification effect.

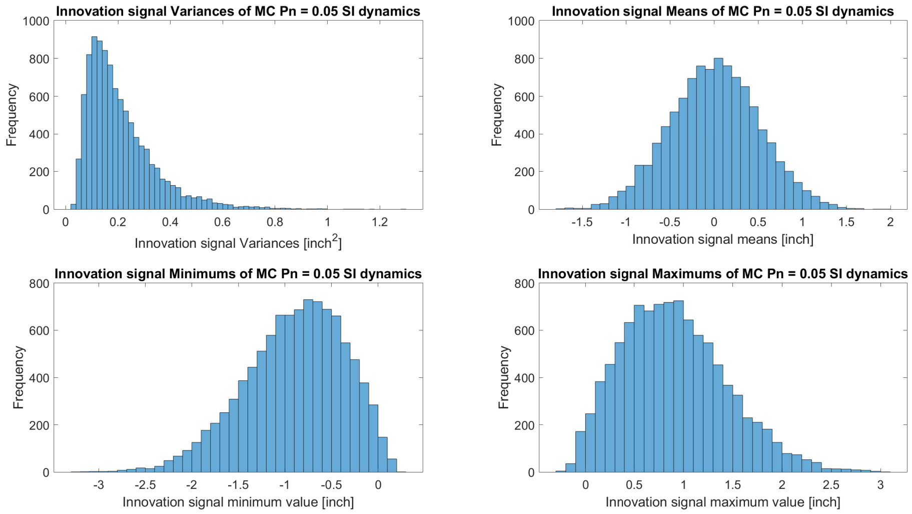

Figure 4.1: MC simulation of the single integrator controlled element dynamics of 10,000 steps showing the innovation signal variance, mean, minimum and maximum distribution for every run $P_n = 0.05$.

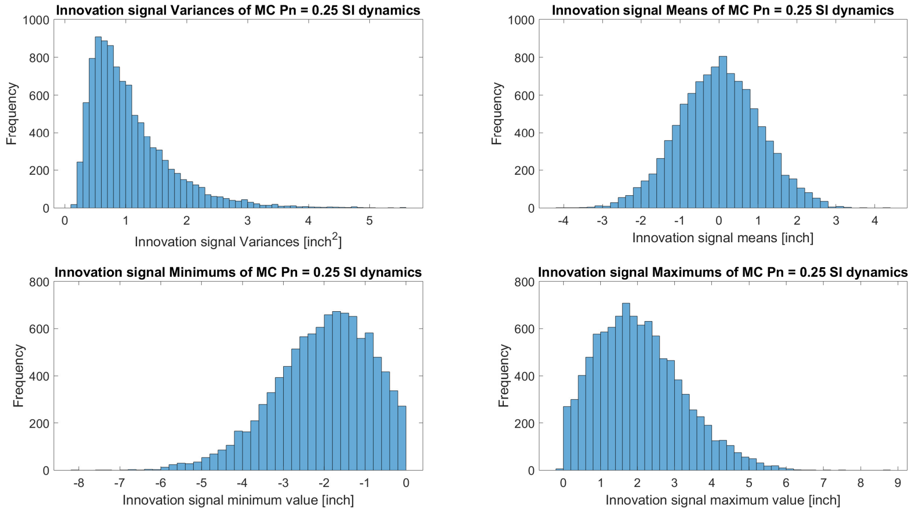

Figure 4.2: MC simulation of the single integrator controlled element dynamics of 10,000 steps showing the innovation signal variance, mean, minimum and maximum distribution for every run, $P_n = 0.25$.

Table 4.1: Mean of the innovation signal variance of the single and double integrator dynamics with variable noise powers.

	Unit	$P_n = 0.05$	$P_n = 0.1$	$P_n = 0.15$	$P_n = 0.2$	$P_n = 0.25$
SI	[inch^2]	0.2109	0.4263	0.6337	0.8514	1.0682
DI	[inch^2]	1.093	2.2475	3.3587	4.4462	5.5012

The distribution of the innovation signal means of the Monte Carlo analysis follows a normal distribution, this can be explained by the Central Limit Theorem and the properties of the system. The Central Limit Theorem is a fundamental statistical theorem that states that the distribution of sample means approaches a normal distribution as the sample size increases, regardless of the underlying distribution of the individual data points [34]. The Central Limit Theorem holds under the following conditions; the sample size is sufficiently large and the individual data points are independent and identically distributed. Which is the

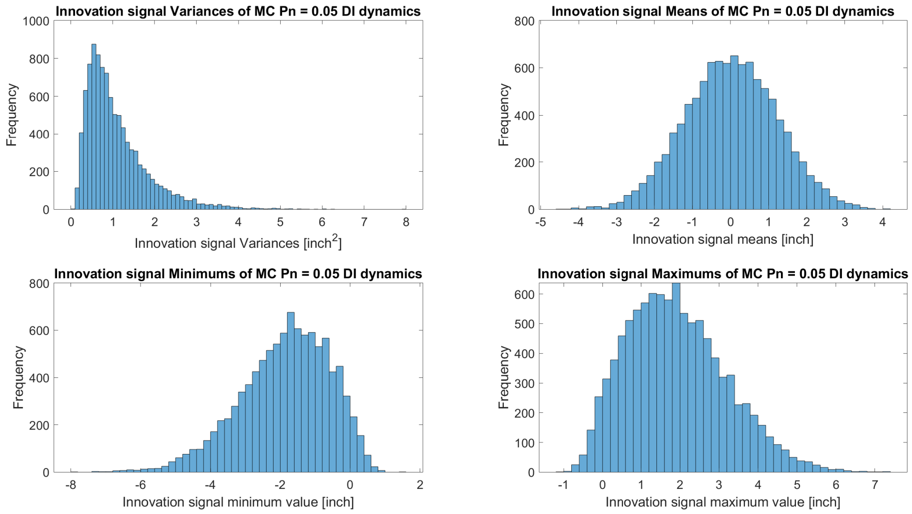

Figure 4.3: MC simulation of the double integrator controlled element dynamics of 10,000 steps showing the innovation signal variance, mean, minimum and maximum distribution for every run, $P_n = 0.05$.

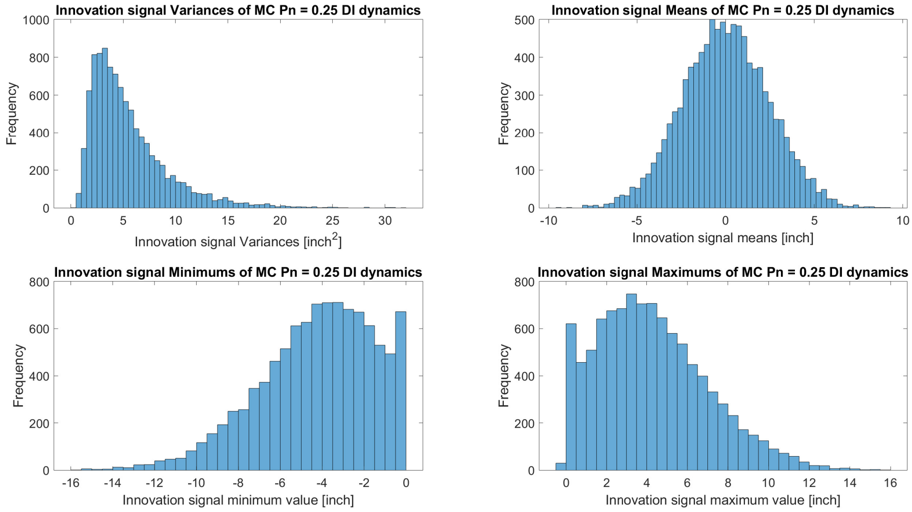

Figure 4.4: MC simulation of the double integrator controlled element dynamics of 10,000 steps showing the innovation signal variance, mean, minimum and maximum distribution for every run, $P_n = 0.25$.

case for zero-mean Gaussian white noise. The filtered white noise is zero-mean Gaussian, meaning that its individual data points follow a Gaussian distribution with a mean of zero.

The mean of the innovation signal approaches zero, as expected. However, it is not fully zero, this can be caused due to the results of the complex interaction between noise, integration, and statistical properties. Filtered white noise introduces randomness into the system's response, even with a mean of zero. Both single and double-integrator dynamics accumulate this integrated or double-integrated noise over time, contributing to non-zero values due to the inherent randomness of noise. As more simulations are conducted, the mean approaches zero, yet individual sample means may oscillate around this value due to statistical variability and finite sample sizes. So the innovation signal is a random walk.

In Table 4.2, the mean values of the innovation signal, considering both the minimum and maximum values obtained from the Monte Carlo analysis, reveal an interesting observation. Unlike the variance, which exhibited a direct relationship with noise power, the mean of the innovation signal does not follow a linear scaling pattern.

The reason behind this lies in the interaction between the remnant and the process of integration. When adjusting the gain of the remnant filter to maintain a constant noise power, it has the effect of selectively amplifying or attenuating different frequency components within the filtered noise signal. Consequently, while the mean values of the minimum and maximum of the innovation signal do increase, they do not show a straightforward linear scaling relationship.

This deviation from linearity is a result of the integration process introducing non-linearities. As various frequencies of noise accumulate during integration, their combined effects can lead to behaviours that do not conform to simple linear scaling. Additionally, because of the properties of noise, extreme values are susceptible to fluctuations.

Table 4.2: Mean of the minimum and maximum value of the innovation signal of the single and double controlled element dynamics with variable noise power.

	Unit		$P_n = 0.05$	$P_n = 0.1$	$P_n = 0.15$	$P_n = 0.2$	$P_n = 0.25$
Min	[inch]	SI	-0.8948	-1.2971	-1.575	-1.8334	-2.0335
	[inch]	DI	-1.8584	-2.712	-3.296	-3.8643	-4.2492
Max	[inch]	SI	0.9025	1.2855	1.574	1.8168	2.0474
	[inch]	DI	1.8945	2.7051	3.346	3.788	4.2587

From Figure 4.5 and Figure 4.6 it can be seen that the innovation signal is significantly large. It is much bigger than the target function and seems to slowly drift to high values, for both the SI and DI controlled element dynamics. It would be very hard to determine statistical thresholds for detecting changes in controlled element dynamics using this innovation signal, due to the extreme values and high variability. It is important to understand where this variability comes from, so both of the components of the innovation signal will be looked at, the remnant n which is the filtered zero-mean Gaussian white noise wH_n, and the CE dynamics H_c.

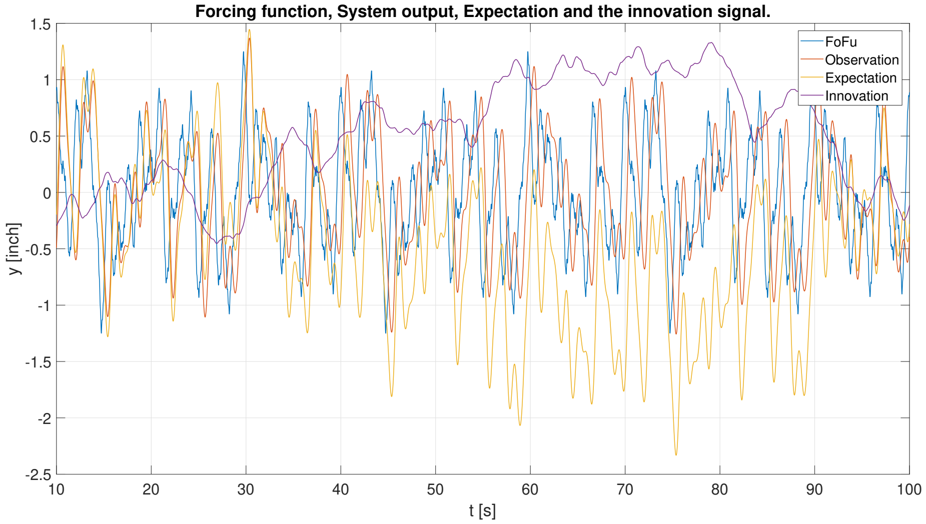

Figure 4.5: Steady-state run of SI dynamics with a $P_n = 0.05$ and remnant filter $\tau_f = 0.23$.

4.2. Influence of the remnant filter on the innovation signal

It is important to understand how the remnant filter influences the innovation signal. The power of the remnant n is influenced by the gain and time constant used in the remnant filter. The remnant filter is a second-order filter for the SI dynamics and a first-order filter for the DI dynamics, with a gain K_f and a remnant-time constant of τ_f. The gain is adjusted for each zero-mean Gaussian white noise realisation of

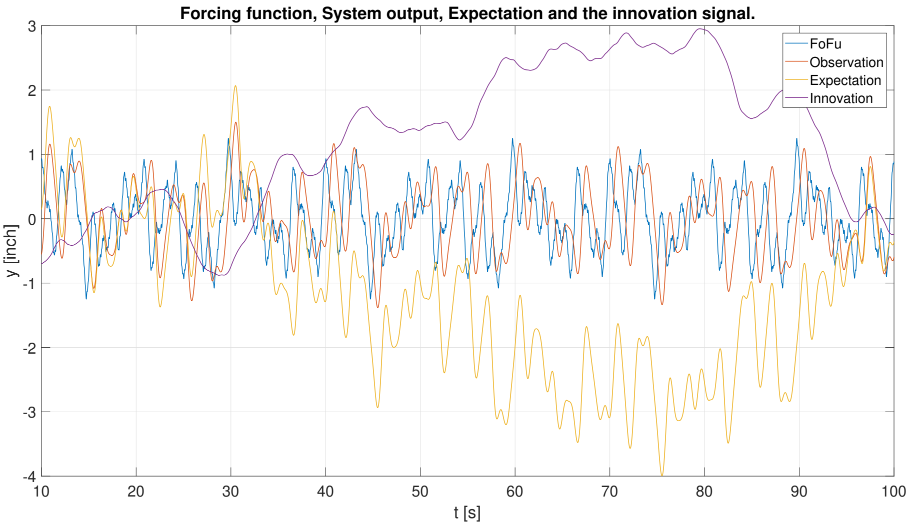

Figure 4.6: Steady-state run of DI dynamics with a $P_n = 0.05$ and remnant filter $\tau_f = 0.23$.

the Monte Carlo simulation, to make sure the noise power P_n is constant. The placement of the filter's poles influences the frequencies the filter lets through. Certain frequencies of noise are amplified or attenuated to a much greater extent, with the different pole placements. This could lead to resonant behaviour, where the system responds strongly to specific frequency components and carries cumulative effects. To better understand these effects different time constants were chosen. The following time constants were chosen $\begin{bmatrix} 0.01 & 0.1 & 0.2 & 0.3 & 0.4 \end{bmatrix}$.

In the Monte Carlo analysis, the innovation signal variance for these different values of the time constant of the remnant filter will be analysed. The mean will not be analysed as this will still be zero mean with a normal distribution irrespective of the remnant filter time constant. The bode plot of the remnant filters is given in Figure 4.7, using unit gain.

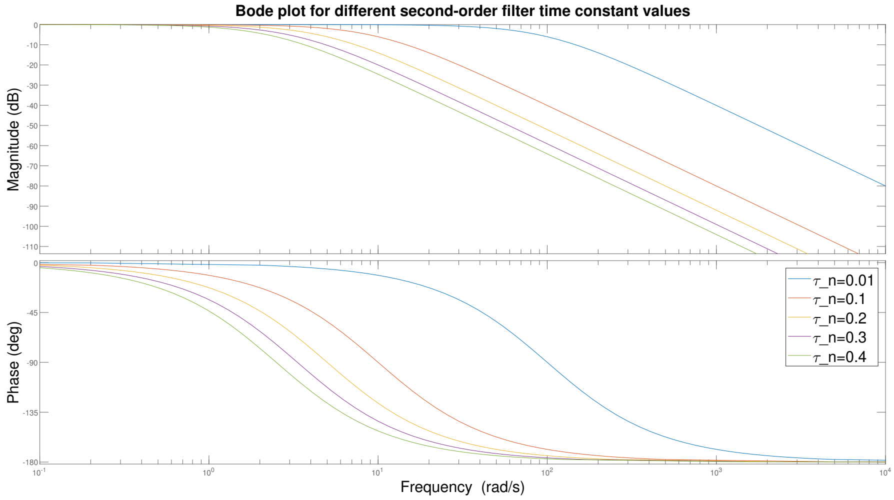

Figure 4.7: Bode plot of the second-order remnant filter with different time-constants τ_f.

The cut-off frequencies of the time-value constants of the remnant filter are given in Table 4.3. The cut-off frequency helps with a better understanding of what frequencies get attenuated and which do not. The higher the value of τ_f the lower the cut-off frequency which means the signal gets attenuated at lower-frequency levels.

Table 4.3: Cut-off frequencies for different values of time-constant τ_f of the remnant filter.

τ_f	Cut-off frequency $[rad/s]$
0.01	64.37
0.1	6.437
0.2	3.220
0.3	2.149
0.4	1.613

The different values of the remnant filter time constant are run for the single integrator dynamics with the noise power of 0.05. The lower the cut-off frequency of the remnant filter the bigger the innovation signal variance. The distribution of the innovation signal gets more right-skewed. It signifies a shift in the central values of the data toward higher values, a bigger discrepancy between the observation and expectation. This shift translates to a more right-skewed lognormal distribution. From the distributions, Appendix A, it can be seen that the data is more right-skewed meaning more extreme values in the distribution, and bigger variances meaning a bigger magnitude of the innovation signal.

Table 4.4: Mean of the distribution of the variances of the innovation signal for different filter time constants of the single integrator CE dynamics with remnant power $P_n = 0.05$.

	$\tau_f = 0.01$	$\tau_f = 0.1$	$\tau_f = 0.2$	$\tau_f = 0.3$	$\tau_f = 0.4$
SI Variance [inch^2]	0.01	0.0705	0.1376	0.2070	0.2687

It can also be seen from Table 4.4 that the mean of the variance distributions becomes bigger when the τ_f becomes bigger. This means that when the remnant filter filters out more of the high-frequency components of the white noise, lower cut-off frequency, and then the innovation signal variability increases. So when more high-frequency noise is let through the filter the innovation signal gets smaller. This is due to the noise power P_n being kept constant, meaning the power of the white noise is spread over more frequencies. This means that a filter that filters out the higher frequencies more, has more power in the lower frequencies. This effect then gets amplified by the controlled element dynamics as will be explained in the next section. The simulation of the steady-state tracking is run again, with the remnant filter values of 0.1 and 0.2. It can be seen from Figure 4.8 and Figure 4.9 that the innovation signal is smaller for the case when the filter lets through more high frequencies while keeping the noise power at the same level of $P_n = 0.05$. For the DI dynamics with the first order filter, this is also the case as can be seen in Figure 4.10 and Figure 4.11.

4.3. Conclusion Preliminary Results

It was found in this chapter that it is not possible to come up with a good threshold for human adaptation due to the effect the remnant filter has on the innovation signal. The innovation signal differs significantly and is way larger than expected. The innovation signal is a random walk which makes defining bounds for detection of a change in controlled element dynamics not feasible. The innovation signal has a tendency to be much larger than the target function making it very difficult to come up with detection thresholds. The model does not provide a good basis for the theoretical threshold for human detection due to the influence of the remnant filter and controlled element dynamics. Therefore, the moment a human detects a change in CE dynamics cannot be determined using this innovation signal as is. The simulations for the change in a controlled element using the sigmoid activation function are not run due to not being able to establish these thresholds. Therefore, the model needs to be adjusted to get more reliable results to determine the threshold for human adaptation.

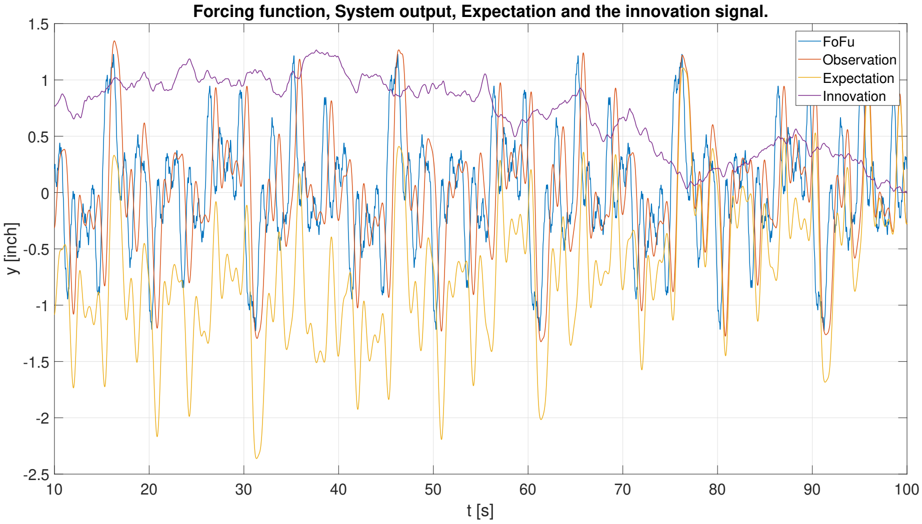

Figure 4.8: Steady-state run of SI dynamics with a $P_n = 0.05$ and remnant filter time constant $\tau_f = 0.1$.

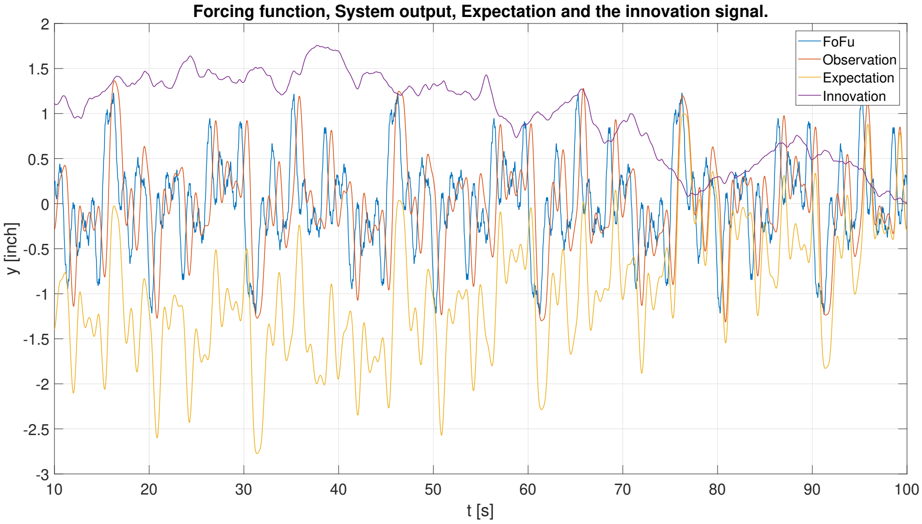

Figure 4.9: Steady-state run of SI dynamics with a $P_n = 0.05$ and remnant filter time constant $\tau_f = 0.2$.

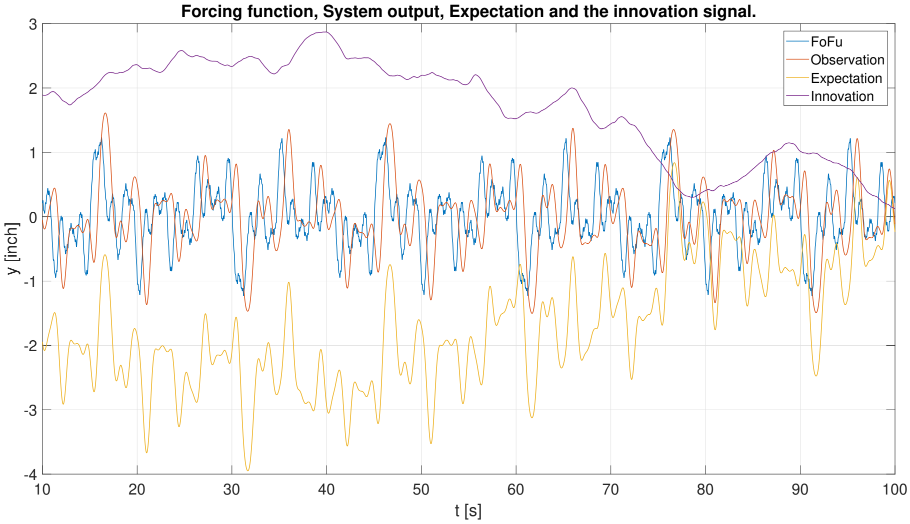

Figure 4.10: Steady-state run of DI dynamics with a $P_n = 0.05$ and different remnant filter $\tau_f = 0.1$.

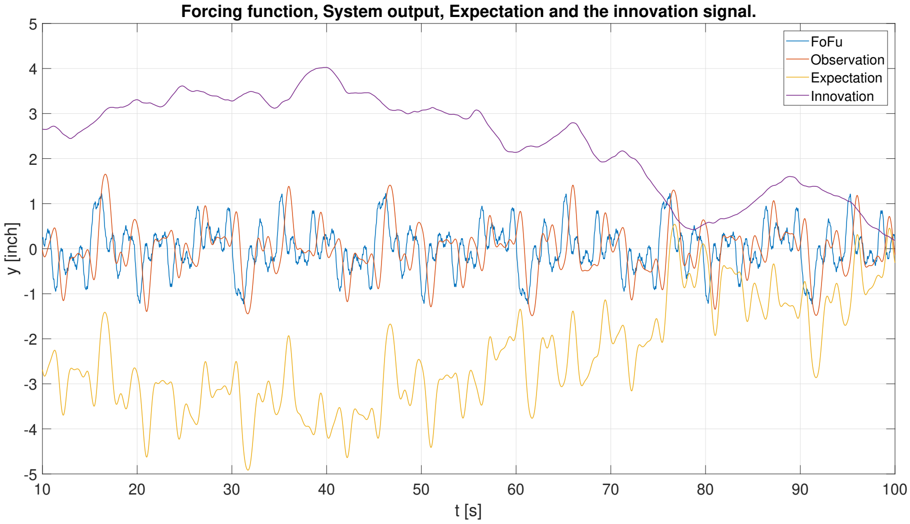

Figure 4.11: Steady-state run of DI dynamics with a $P_n = 0.05$ and different remnant filter $\tau_f = 0.2$.

5

Conclusion

The critical significance of understanding human adaptability within dynamic control systems is that control system failures can lead to catastrophic accidents.

The foundational work of McRuer and Jex introduced the crossover model, shedding light on the modelling of pilot behaviour. Subsequently, Young et al. expanded upon these insights by conducting experiments on adaptive human control, ultimately contributing to the development of adaptive control theory. The detection, identification, and modification phases constitute pivotal elements of human adaptive control behaviour. Especially detection of changes in controlled element dynamics is not yet fully understood or modelled correctly.

The model of Mulder et al. proposes that the human controller has an internal model of the controlled element dynamics that builds their own expectation. The model states that when there is a change in controlled element dynamics there is a mismatch between the human observation and expectation. When this mismatch exceeds a certain threshold the human controller will adjust their control behaviour and update their internal model. The central research question revolves around the impact of this mismatch between human observation and expectation to determine the detection of changes in controlled element dynamics during tracking tasks. It was found from the model that the difference between human observation and expectation, innovation signal, is entirely nH_c, the remnant (modelled as filtered zero-mean Gaussian white noise) and the controlled element dynamics when the internal model matches the real model.

A Monte Carlo analysis was used to try to determine these theoretical thresholds. However, it was found that the model did not provide a solid basis to determine these thresholds due to the remnant filter and controlled element dynamics, due to the innovation signal being a random walk. Therefore, more research was done into the effects of the remnant and controlled element dynamics on the innovation signal. Several critical findings were discovered, notably highlighting the non-linear and multiplicative nature of the responses to the noise and the influential role played by the remnant filter. It was found that when the noise filter has a lower cut-off frequency there is a shift in the lognormal distribution of the variances meaning the variability in the innovation signal grew significantly. This shift indicates a transition toward higher values in the original data, resulting in a more right-skewed lognormal distribution and a significant increase in the innovation signal.

Moreover, it was evident that the mean of the variance distributions increases as the time constant τ_f of the remnant filter increases. This observation suggests that when the low-pass noise filter attenuates more high-frequency components of the zero-mean Gaussian white noise (specifically with higher τ_f values), the innovation signal intensifies. Filtering out less high frequencies leads to a reduction in the innovation signal while keeping the remnant power constant, as the remnant power becomes distributed across a broader range of frequencies.

It is clear that the model does not provide a solid basis for determining the theoretical threshold for detecting a change in controlled element dynamics and the model needs to be refined further.

6

Further research

Addressing the remnant effect is crucial for improving the model of Mulder et al. A possible solution can be the integration of an observer model to mitigate the impact of the remnant and the effects of the random walk. Observer models, such as state observers or Kalman filters, offer an effective means of estimating a system's internal states, providing accurate information to guide control actions.

Observer models serve as a vital component of feedback control systems. They excel at estimating a system's current state based on available measurements. This estimation offers a more precise representation of the actual system state, including any lingering remnant effects. By utilizing this accurate state estimate the observer model can help minimize the discrepancies between the observation and expecation. The observer model compensates for any remnant effects that may have accumulated over time.

The following steps will be taken to further the research and answer the research question. Both the single and double integrator CE dynamics will be looked into. The data will be taken from an experiment involving a change in controlled element dynamics using a sigmoid activation function for pursuit-tracking tasks.

Step 1: **Determine Gain for Observer Model**

1. **Sensitivity Analysis for different gain values for the observer model**
    - Perform a sensitivity analysis with various gain values for the observer model.
    - Vary the gain to observe its impact on the innovation signal.
    - Note that a too-high gain leads to observation dominance, while a too-low gain leads to expectation dominance.
2. **Create a Change in Controlled Element Dynamics**
    - Use a sigmoid activation function to introduce a change in the controlled element dynamics.
    - Calculate the time it takes for the innovation signal to exceed multiple steady-state tracking errors.
3. **Analyze Innovation Signal**
    - Examine the innovation signal before and after the controlled element dynamics change, to determine the influence of the gain of the observer model on the innovation signal.
    - Determine whether there is a significant difference in the innovation signal during steady-state tracking and when there is a change in CE dynamics for the different gain values. When there is no significant difference a steady-state tracking threshold will not be able to be determined.
4. **Observer model Gain Selection**
    - Choose a gain value that strikes a balance between observation and expectation influence on the innovation signal. Create ROC curve for different values of the Observer gain to determine what observer gain strikes the best balance between true and false positives.
    - This selected gain will be used for steady-state tracking.

Step 2: **Monte Carlo Analysis for steady-state tracking**

1. **Run Monte Carlo Analysis for steady-state tracking**
    - Conduct a Monte Carlo analysis with varying remnant power settings.
    - Generate a change in controlled element dynamics.
2. **Threshold Determination based on the output of the MC**
    - Determine thresholds for detecting changes in controlled element dynamics using the ROC curve.

Step 3: **Validation with Experiment Data for a Pursuit Tracking task with a change in CE dynamics**

1. **Moment of Detection**
    - Utilize the previously determined thresholds to identify the moment of change detection in the simulated data and determine the average detection time
2. **Validation with Experimental Data**
    - Assess whether the thresholds successfully detect changes in real-world scenarios using the average detection time from the simulations and the experimental data.

References

[1] L.R. Young et al. “Adaptive Dynamic Response Characteristics of the Human Operator in Simple Manual Control”. In: *IEEE Transactions on Human Factors in Electronics* HFE-5.1 (1964), pp. 6–13. DOI: 10.1109/THFE.1964.231648.

[2] L.R. Young. “On Adaptive Manual Control”. In: *IEEE Transactions on Man-Machine Systems* 10.4 (1969), pp. 292–331. DOI: 10.1109/TMMS.1969.299931.

[3] D.T. McRuer et al. “A Review of Quasi-Linear Pilot Models”. In: *IEEE Transactions on Human Factors in Electronics* HFE-8.3 (1967), pp. 231–249. DOI: 10.1109/THFE.1967.234304.

[4] D.C. Miller et al. “The Adaptive Response of the Human Controller to Sudden Changes in Controlled Process Dynamics”. In: *IEEE Transactions on Human Factors in Electronics* HFE-8.3 (1967), pp. 218–223. DOI: 10.1109/THFE.1967.233971.

[5] M. Mulder et al. “Neuroscience Perspectives on Adaptive Manual Control with Pursuit Displays”. In: *IFAC-PapersOnLine* 55.29 (2022). 15th IFAC Symposium on Analysis, Design and Evaluation of Human Machine Systems HMS 2022, pp. 160–165. DOI: https://doi.org/10.1016/j.ifacol.2022.10.249.

[6] C.S. Draper et al. “Model of the Neuromuscular Dynamics of the Human Pilot’s Arm”. In: *Journal of Aircraft* 41.6 (2004), pp. 1482–1490. DOI: 10.2514/1.14434.

[7] H.J. Damveld et al. “Design of Forcing Functions for the Identification of Human Control Behavior”. In: *Journal of Guidance, Control, and Dynamics* 33.4 (2010), pp. 1064–1081. DOI: 10.2514/1.47730.

[8] J. Elkind. “Characteristics of simple manual control systems”. In: (Sept. 2005).

[9] M. Mulder et al. “Manual Control with Pursuit Displays: New Insights, New Models, New Issues”. In: *IFAC-PapersOnLine* 52 (Jan. 2019), pp. 139–144. DOI: 10.1016/j.ifacol.2019.12.125.

[10] K.S. Fu et al. “An adaptive model of the human operator in a control system”. In: *Control and Information Systems Laboratory, School of Electrical Engineering* 64-15 (1964).

[11] A.V. Phatak et al. “Model of the adaptive behavior of the human operator in response to a sudden change in the control situation.” In: *IEEE Transactions on Man-Machine Systems* 10(3).72–80 (1969). DOI: 10.1109/THFE.1967.233971.

[12] D.H. Weir et al. “Model of human operator response to step transitions in controlled element dynamics.” In: *NASA CR-671. NASA Contract Rep NASA CR.* (1967), pp. 1–33. DOI: 10.1037/e506122009-007.

[13] L. Young et al. “Bang-bang aspects of manual control in high-order systems”. In: *IEEE Transactions on Automatic Control* 10.3 (1965), pp. 336–341. DOI: 10.1109/TAC.1965.1098168.

[14] A.V. Phatak et al. “Decision processes in the adaptive behavior of human controllers”. In: *IEEE Transactions on Systems Science and Cybernetics* 5.4 (1969), pp. 339–351.

[15] J. van Ham et al. “Predicting Human Control Adaptation from Statistical Variations in Tracking Error and Error Rate”. In: *IFAC-PapersOnLine* 55 (Oct. 2022), pp. 166–171. DOI: 10.1016/j.ifacol.2022.10.250.

[16] Niemela R.J. et al. “Detection of a change in plant dynamics in a man-machine system”. In: *IEEE Transactions on Systems, Man, and Cybernetics* (1975), pp. 615–617.

[17] P.D. Neilson et al. “Adaptive Optimal Control of Human Tracking”. In: *Motor Control and Sensory Motor Integr.: Issues and Directions,* In D.J. Glencross and J.P. Piek (eds.) (1995), pp. 97–140.

[18] C. Frith et al. “Abnormalities in the Awareness and Control of Action”. In: *Philosophical transactions of the Royal Society of London. Series B, Biological sciences* 355 (Feb. 2001), pp. 1771–88. DOI: `10.1098/rstb.2000.0734`.

[19] P.D. Neilson et al. “A neuroengineering solution to the optimal tracking problem”. In: *Human Movement Science* 18 (1999), pp. 155–183.

[20] R. Hess. “A model for pilot control behavior in analyzing potential loss-of-control events”. In: *Proceedings of the Institution of Mechanical Engineers, Part G: Journal of Aerospace Engineering* 228 (July 2014), pp. 1845–1856. DOI: `10.1177/0954410014531218`.

[21] R. Hess. “Modeling Human Pilot Adaptation to Flight Control Anomalies and Changing Task Demands”. In: *Journal of Guidance, Control, and Dynamics* 39 (June 2015), pp. 1–12. DOI: `10.2514/1.G001303`.

[22] R. Hess. “Modeling Pilot Control Behavior with Sudden Changes in Vehicle Dynamics”. In: *Journal of Aircraft* 46 (Sept. 2009), pp. 1584–1592. DOI: `10.2514/1.41215`.

[23] R. Hess. “Modeling the Pilot Detection of Time-Varying Aircraft Dynamics”. In: *Journal of Aircraft* 49 (Nov. 2012), pp. 2100–2104. DOI: `10.2514/1.C031805`.

[24] N. Jakimovska et al. “Using the Hess Adaptive Pilot Model for Modeling Human Operator’s Control Adaptations in Pursuit Tracking”. In: *AIAA SCITECH 2023 Forum*. DOI: `10.2514/6.2023-0541`. eprint: `https://arc.aiaa.org/doi/pdf/10.2514/6.2023-0541`. URL: `https://arc.aiaa.org/doi/abs/10.2514/6.2023-0541`.

[25] L. Terenzi et al. “Adaptive Manual Control: a Predictive Coding Approach”. In: *AIAA SCITECH 2022 Forum*. DOI: `10.2514/6.2022-2448`. eprint: `https://arc.aiaa.org/doi/pdf/10.2514/6.2022-2448`. URL: `https://arc.aiaa.org/doi/abs/10.2514/6.2022-2448`.

[26] M. Mulder et al. “Manual Control Cybernetics: State-of-the-Art and Current Trends”. In: *IEEE Transactions on Human-Machine Systems* PP (Oct. 2017), pp. 1–18. DOI: `10.1109/THMS.2017.2761342`.

[27] M.M. van Paasen et al. “Model of the Neuromuscular Dynamics of the Human Pilot’s Arm”. In: *Journal of Aircraft* 41.6 (2004), pp. 1482–1490. DOI: `10.2514/1.14434`.

[28] R.E. Magdaleno et al. “Tracking Quasi-predictable Displays Subjective Predictability Graduations, Pilot Models for Periodic and Narrowband Inputs”. In: *In Proc. of the 5th Ann. NASA-University Conference on Manual Control* (1969), pp. 391–428.

[29] F.M. Drop et al. “The Predictability of a Target Signal Affects Manual Feedforward Control”. In: *IFAC-PapersOnLine* 49.19 (2016). 13th IFAC Symposium on Analysis, Design, and Evaluation of Human-Machine Systems HMS 2016, pp. 177–182. DOI: `https://doi.org/10.1016/j.ifacol.2016.10.482`.

[30] M. Mulder et al. “Manual Control with Pursuit Displays: New Insights, New Models, New Issues”. In: *IFAC-PapersOnLine* 52 (Jan. 2019), pp. 139–144. DOI: `10.1016/j.ifacol.2019.12.125`.

[31] D.M. Wolpert et al. “Internal Models in the Cerebellum”. In: *Trends in Cognitive Sciences* 2(9) (1998), pp. 338–347.

[32] P.M.T. Zaal. “Manual Control Adaptation to Changing Vehicle Dynamics in Roll–Pitch Control Tasks”. In: *Journal of Guidance, Control, and Dynamics* 39.5 (2016), pp. 1046–1058. DOI: `10.2514/1.G001592`.

[33] D.E. Newland. *An Introduction to Random Vibrations and Spectral Analysis*. 2nd. ed. New York: Longman Scientific and Engineering, 1984.

[34] Y. Dodge. *The Concise Encyclopedia of Statistics*. Feb. 2008. DOI: `10.1007/978-0-387-32833-1`.

[35] M. Barragan. “Modeling the Human Operator’s Detection of a Change in Controlled Element Dynamics”. In: *Delft University of Technology* (2023). DOI: `http://resolver.tudelft.nl/uuid:5d9f79a5-6686-4767-a01d-01dc341fa990`.

A

All simulation results

This chapter will display all the different Monte Carlo analyses done on both the single and double-integrator-controlled element dynamics for different noise powers. The Figure A.1-Figure A.6 show the histograms for the Monte Carlo analysis. Lastly, the Monte Carlo distributions of the variances are shown.

The Figure A.7-Figure A.8 are the distribution of the variances for a noise power $P_n = 0.05$ for single and double integrator controlled element dynamics.

The remnant filter time values τ_f of $\begin{bmatrix}0.01 & 0.1 & 0.2 & 0.3 & 0.4\end{bmatrix}$.

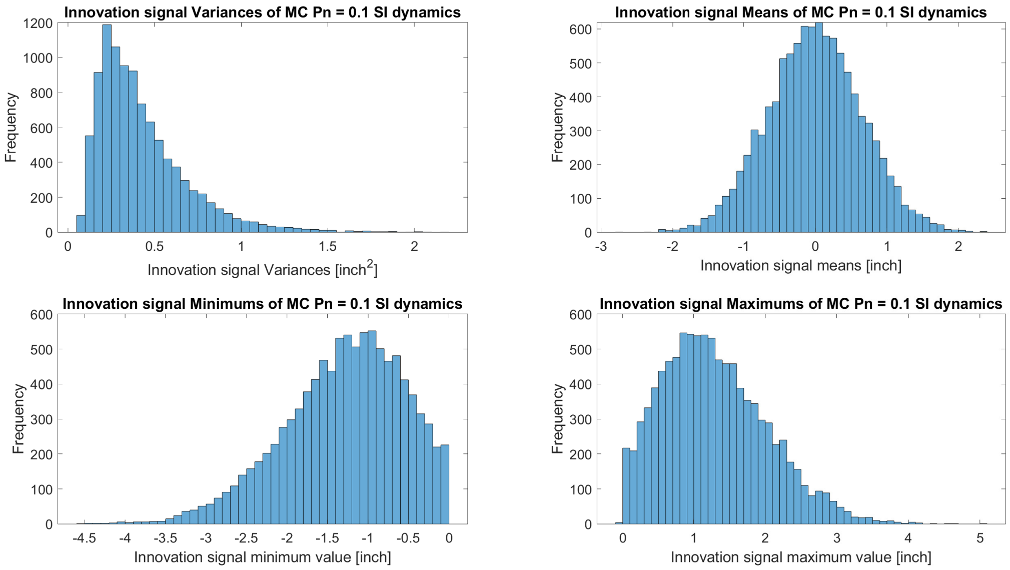

Figure A.1: MC simulation of the single integrator controlled element dynamics of 10,000 steps showing the innovation signal variance, mean, minimum and maximum distribution for every run $P_n = 0.1$.

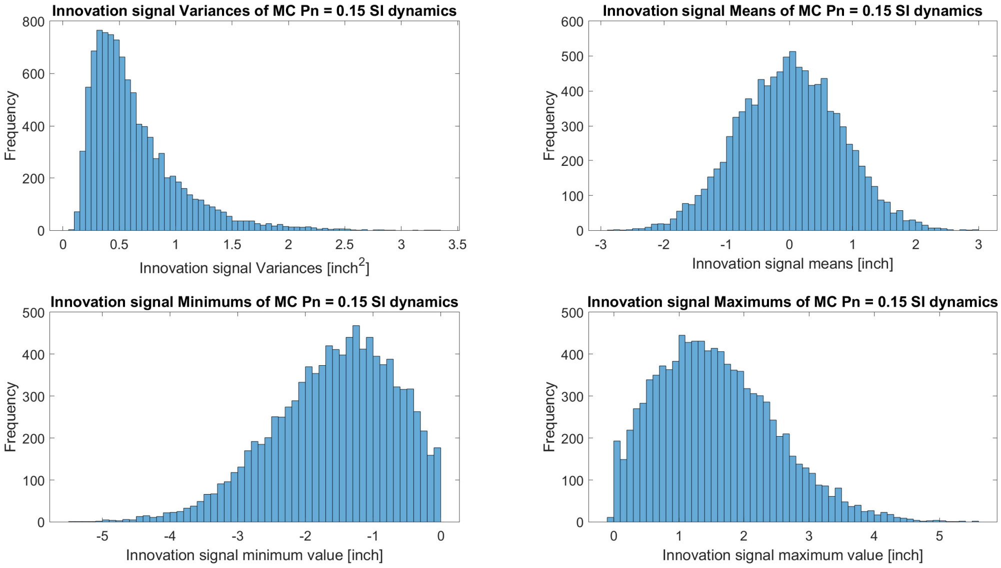

Figure A.2: MC simulation of the single integrator controlled element dynamics of 10,000 steps showing the innovation signal variance, mean, minimum and maximum distribution for every run, $P_n = 0.15$.

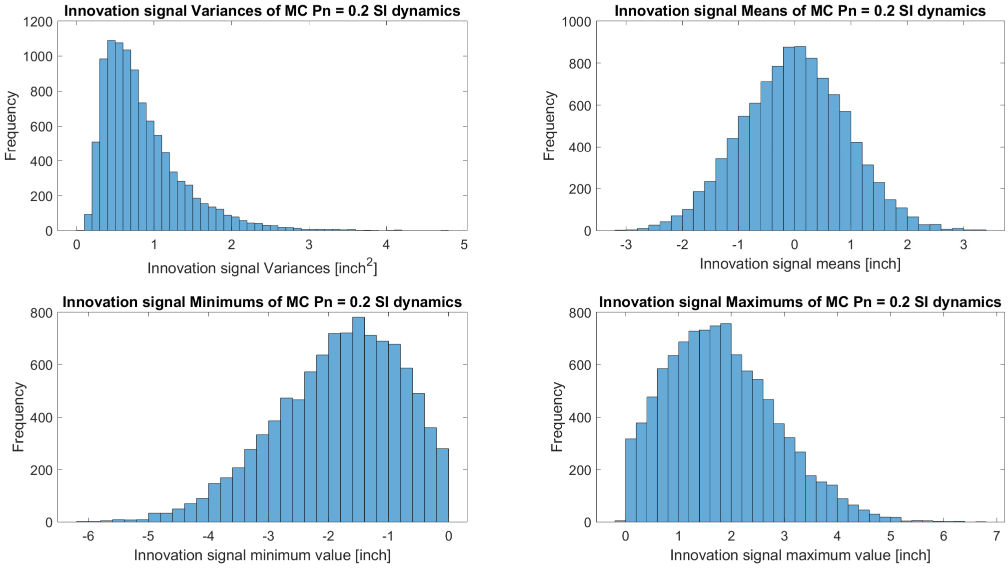

Figure A.3: MC simulation of the single integrator controlled element dynamics of 10,000 steps showing the innovation signal variance, mean, minimum and maximum distribution for every run, $P_n = 0.2$.

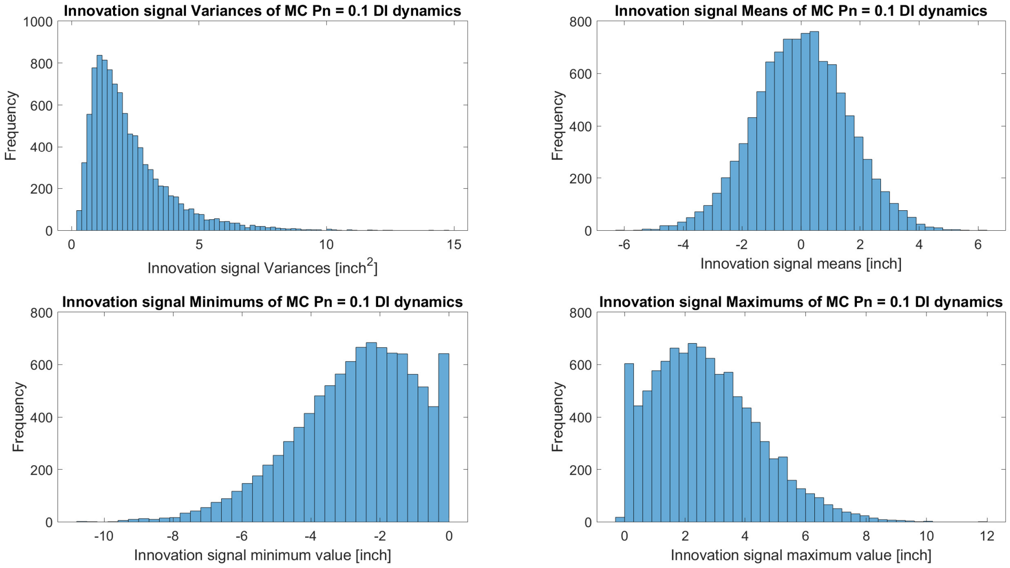

Figure A.4: MC simulation of the double integrator controlled element dynamics of 10,000 steps showing the innovation signal variance, mean, minimum and maximum distribution for every run, $P_n = 0.1$.

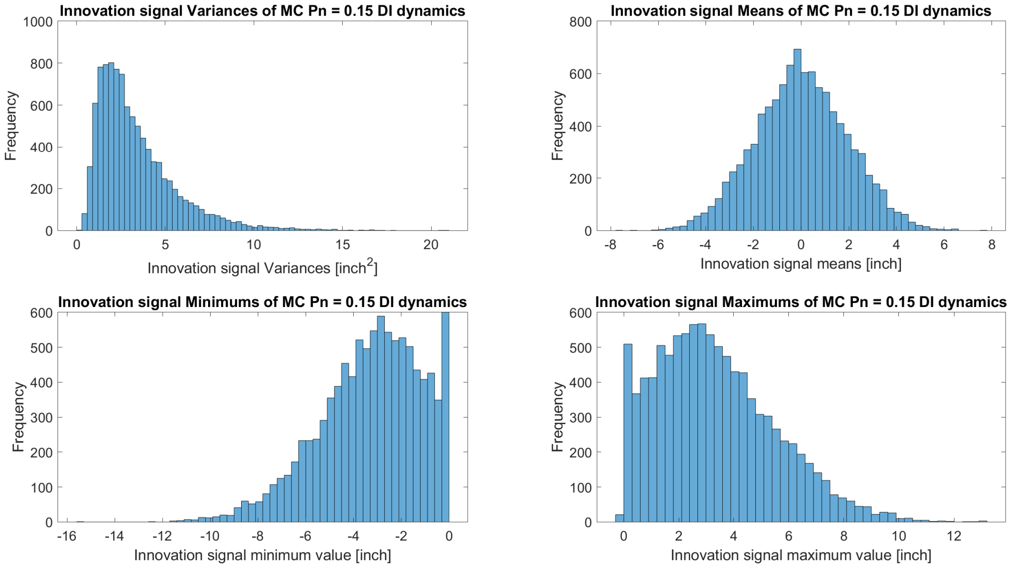

Figure A.5: MC simulation of the double integrator controlled element dynamics of 10,000 steps showing the innovation signal variance, mean, minimum and maximum distribution for every run, $P_n = 0.15$.

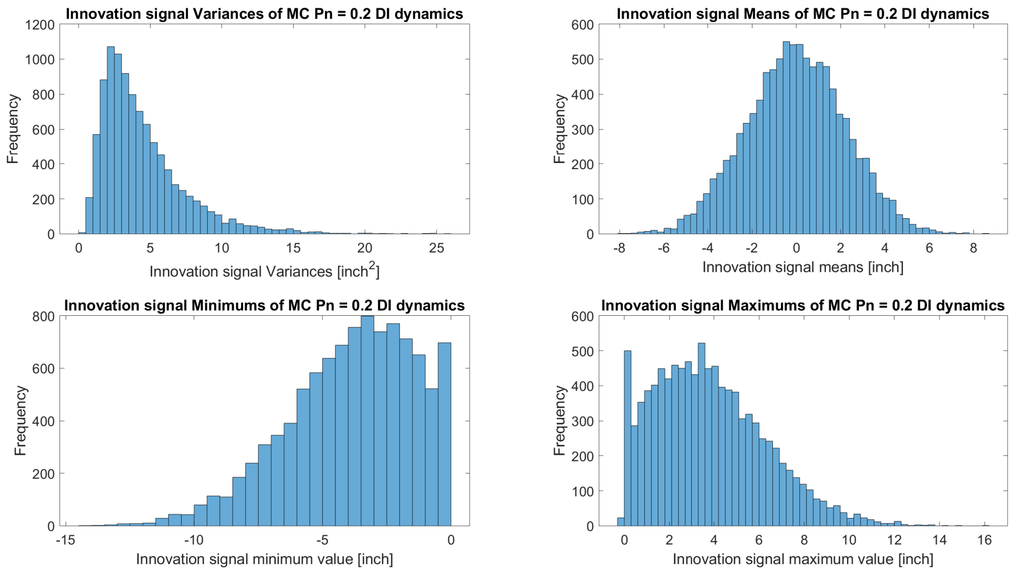

Figure A.6: MC simulation of the double integrator controlled element dynamics of 10,000 steps showing the innovation signal variance, mean, minimum and maximum distribution for every run, $P_n = 0.2$.

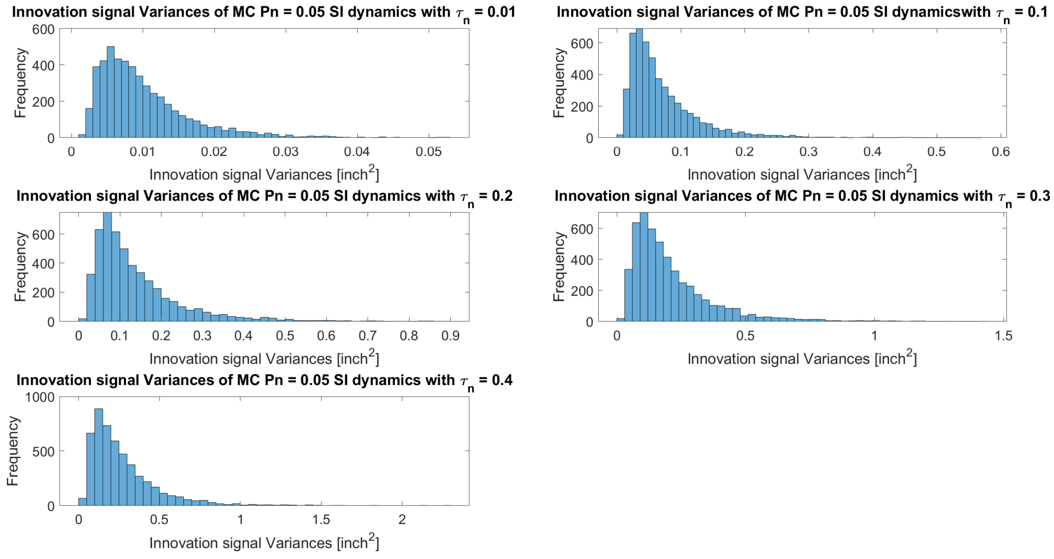

Figure A.7: Variances of the innovation signal MC SI Dynamics with $P_n = 0.05$ and varying τ_f.

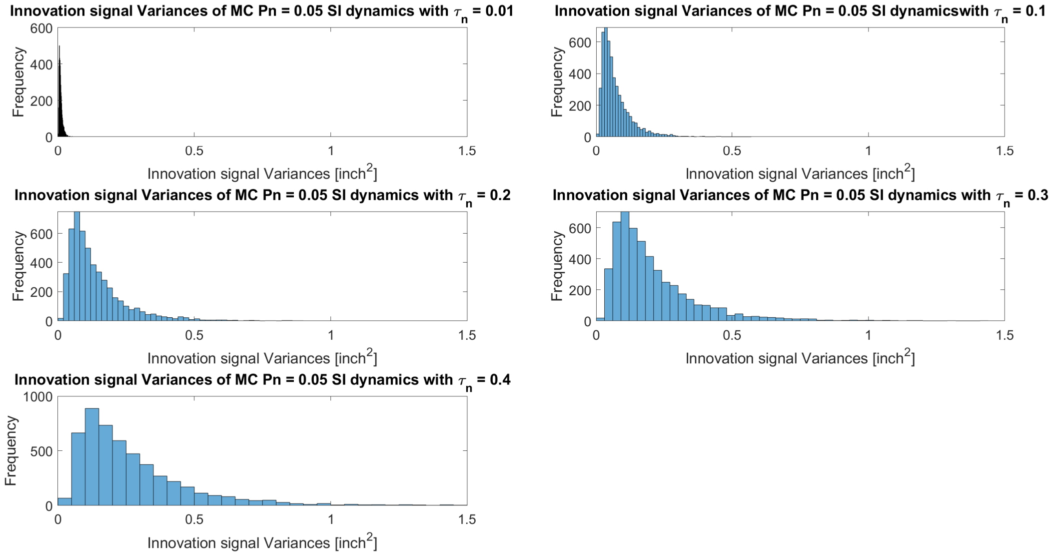

Figure A.8: Variances of the innovation signal MC SI Dynamics with $P_n = 0.05$ and varying τ_f, with standardized x limit.

B

Distributions analysis explained

This chapter gives a bit more insight into why the distribution of the variance is a lognormal distribution.

B.1. Visual inspection

From visual inspection, it became clear that the distribution of the variances of the Monte Carlo analysis was either a lognormal or log-logistic distribution, as can be seen in Figure B.1. The distribution only has positive values and is right-skewed indicating that it could be either lognormal or log-logisitc.

The lognormal distribution often arises for variables from multiplicative processes. For the lognormal distribution, the natural logarithm of the data follows a normal distribution. Its parameters, the location parameter (μ) and the scale parameter (σ), correspond respectively to the mean and standard deviation of the logarithm of the data.

On the other hand, the log-logistic distribution also exhibits positive values and a right-skewed shape, this distribution models a variable where the logarithm of the variable follows a logistic distribution. The log-logistic distribution is described by parameters α (location) and β (scale). Just like the lognormal distribution, it arises in distributions where the variables undergo multiplicative changes.

Although the lognormal and log-logistic distributions share many characteristics due to their right-skewed shapes and positive values, they diverge in their underlying distributions for logarithms and their tail behaviour. The log-logistic distribution, in particular, is known to accommodate extreme values more effectively due to its heavier tails.

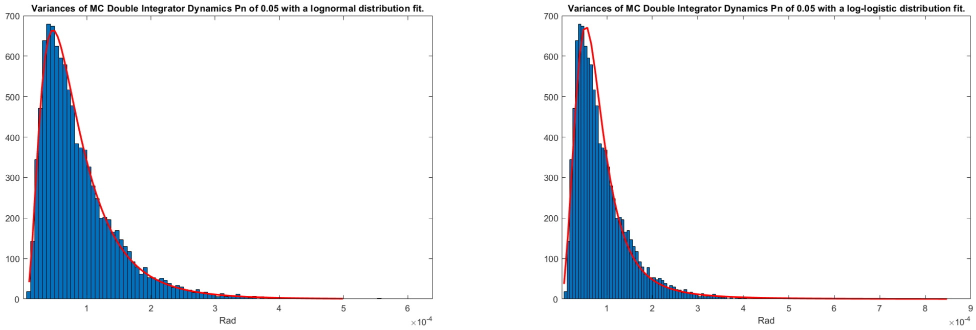

Figure B.1: Variances of MC Double Integrator Dynamics P_n of 0.05 with a lognormal and log-logistic distribution fit.

From the visual inspection, it seems clear that both these distributions can be a good fit, therefore, more test is needed to figure out the correct distribution.

B.2. Cumulative Distribution Function (CDF) plots

The Cumulative Distribution Function (CDF) in statistics provides a powerful way to understand the probability distribution of a random variable. It quantifies the likelihood that the variable takes on a value less than or equal to a specific value. The CDF graphically represents the cumulative probabilities, starting from zero for the lowest possible value and approaching one as the value increases. In essence, it offers a comprehensive view of how data is spread across a range of values, making it a valuable tool for probability analysis.

The analytical CDF serves as a pivotal tool in assessing the goodness of fit of a particular probability distribution to empirical data. By comparing the analytical CDF, generated from a hypothesized distribution, to the empirical CDF derived from observed data, it can be gauged goodness of a distribution fit between the model and reality. This visual comparison allows for an examination of potential discrepancies in how well the assumed distribution describes the observed data. The analytical CDF of both the lognormal and log-logistic distributions can be found in Figure B.2 and Figure B.3 respectively. It can be seen from the figure that both distributions still fit quite well compared to their theoretical distributions, but the lognormal distribution seems to fit a bit better.

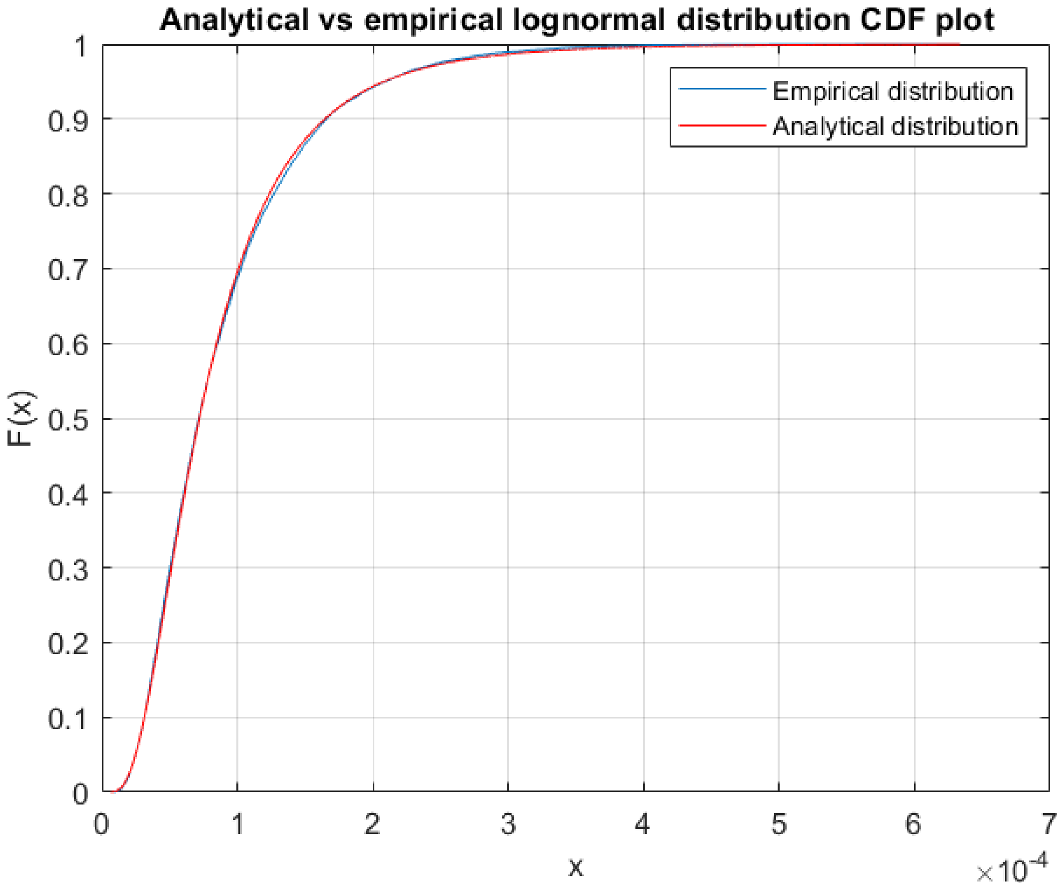

Figure B.2: CDF plots of the variances for the analytical and empirical lognormal distribution.

B.3. Q-Q plots

Q-Q plots, short for quantile-quantile plots, are a graphical tool used in statistics to assess the goodness of fit between a sample dataset and a theoretical probability distribution. They help determine whether the assumed distribution accurately describes the observed data. In a Q-Q plot, the x-axis represents quantiles from the theoretical distribution, while the y-axis represents quantiles from the sample dataset. If the data follows the assumed distribution perfectly, the points on the plot would form a straight line at a 45-degree angle. Deviations from this line indicate departures from the assumed distribution.

For a lognormal distribution, its Q-Q plot typically exhibits a distinctive pattern. When the data is log-transformed, the plot transforms into a straight line of 45 degrees. This transformation aligns the log-transformed data with a normal distribution, making it useful for assessing whether the data is lognormally

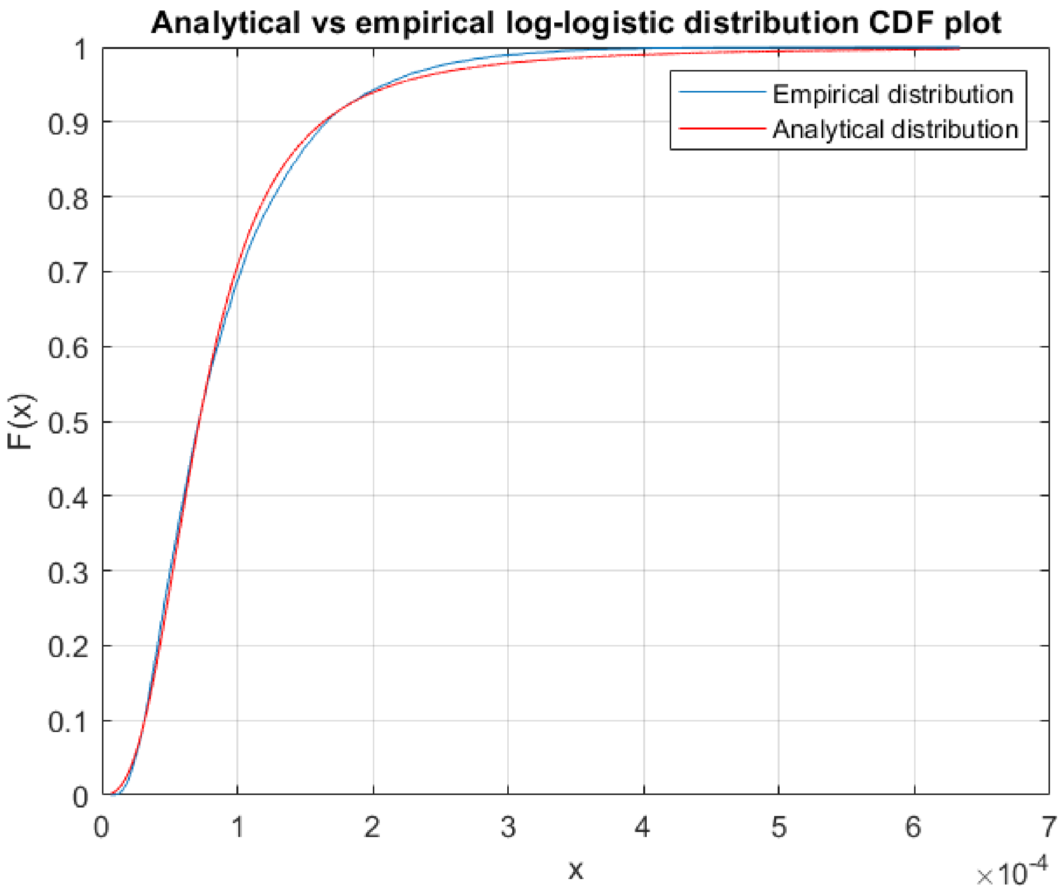

Figure B.3: CDF plots of the variances for analytical and empirical log-logistic distribution.

distributed. Deviations from this line indicate departures from lognormality. From Figure B.4 the points bend upward at the ends, which implies heavier tails than a lognormal distribution.

In the case of a log-logistic distribution, the Q-Q plot would exhibit a characteristic S-shaped curve. The reason lies in the nature of the log-logistic distribution, which can have heavier tails compared to a normal distribution. In the plot of the quantiles of the data against the quantiles of the log-logistic distribution, the S-shaped curve should emerge. This curve shape indicates that the log-logistic distribution has heavier tails than the assumed normal distribution. From Figure B.5 it can be seen that the theoretical and empirical distributions do not overlap very well.

B.4. Statistical tests

The Kolmogorov-Smirnov test, often referred to as the K test, is a non-parametric statistical test used to assess whether a sample of data follows a specific probability distribution or whether two samples of data come from the same underlying distribution. It is a versatile and widely used method in data analysis and hypothesis testing.

At its core, the K test works by comparing the Empirical Cumulative Distribution Function (ECDF) of the sample data with the CDF of the hypothesized theoretical distribution. The null hypothesis for the K test assumes that the sample data and the theoretical distribution are drawn from the same underlying population. In other words, it suggests that there is no significant difference between the sample distribution and the theoretical distribution being tested.

The test produces a statistic, often denoted as 'H', which represents 0 when the null hypothesis is accepted and 0 when it is rejected. The K-S test then computes a p-value, which quantifies the level of agreement between the sample data and the theoretical distribution. A small p-value (typically below

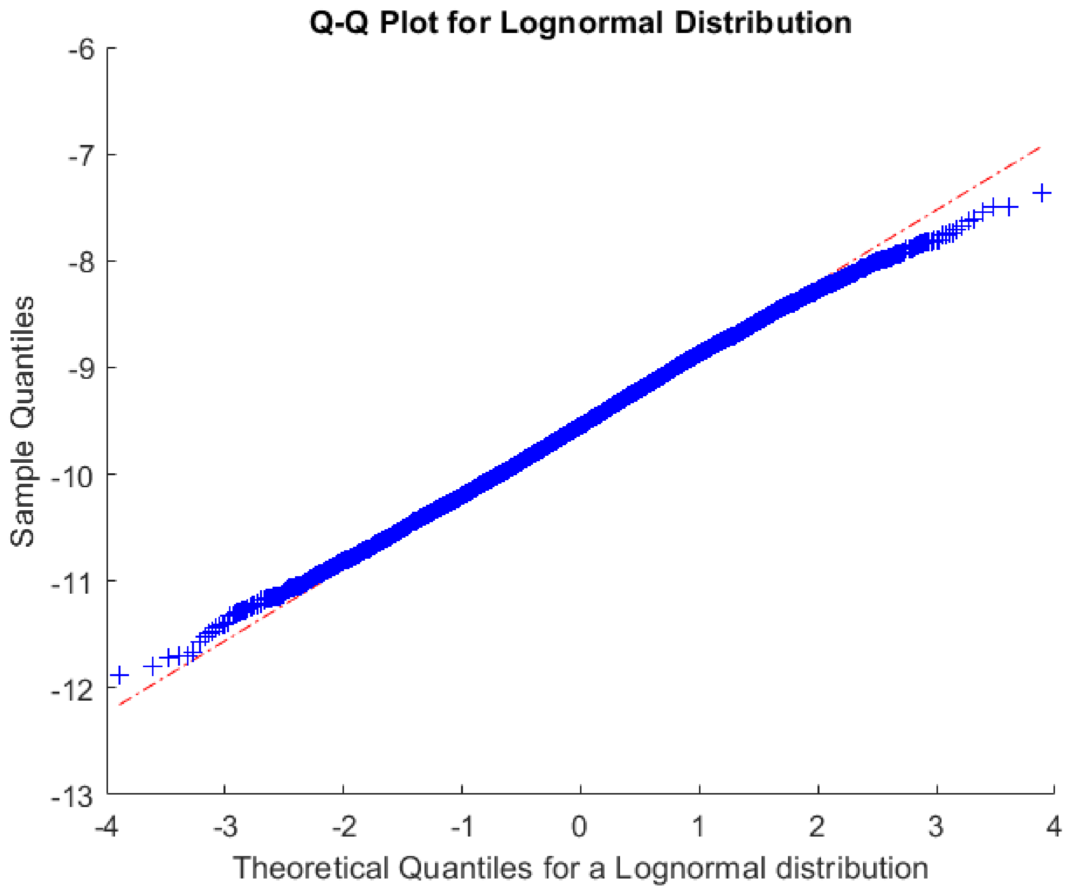

Figure B.4: Q-Q plot of the log-transformed variances of the analytical vs. empirical distribution.

a chosen significance level, such as 0.05) suggests that there is evidence to reject the null hypothesis, indicating that the sample data does not follow the hypothesized distribution. Conversely, a larger p-value indicates that there is no significant evidence to reject the null hypothesis, implying that the sample data is consistent with the theoretical distribution.

Interpreting the results of the K-S test is straightforward:

If the p-value is small (e.g., less than 0.05), the null hypothesis would be rejected. This means that the sample data is not well-described by the hypothesized distribution. If the p-value is large (e.g., greater than 0.05), the null hypothesis would not be rejected. This suggests that the sample data is consistent with the hypothesized distribution. The K test is run for all different noise powers for both the single and double integrator dynamics and for both the theoretical vs. empirical lognormal and log-logistic distributions. The values are summarised in Table B.1. It can be seen from the table that the lognormal distribution is the better fit for the distribution of the variances.

B.5. Conclusion

When the log-transformed variances are distributed normally, then the underlying distribution is lognormal distributed. It can clearly be seen that from Figure B.6 the distribution is normally distributed. From the different statistical tests, the Q-Q plot and the CDF plot, it can be concluded that indeed the variances of the Monte Carlo analysis are lognormal distributed.

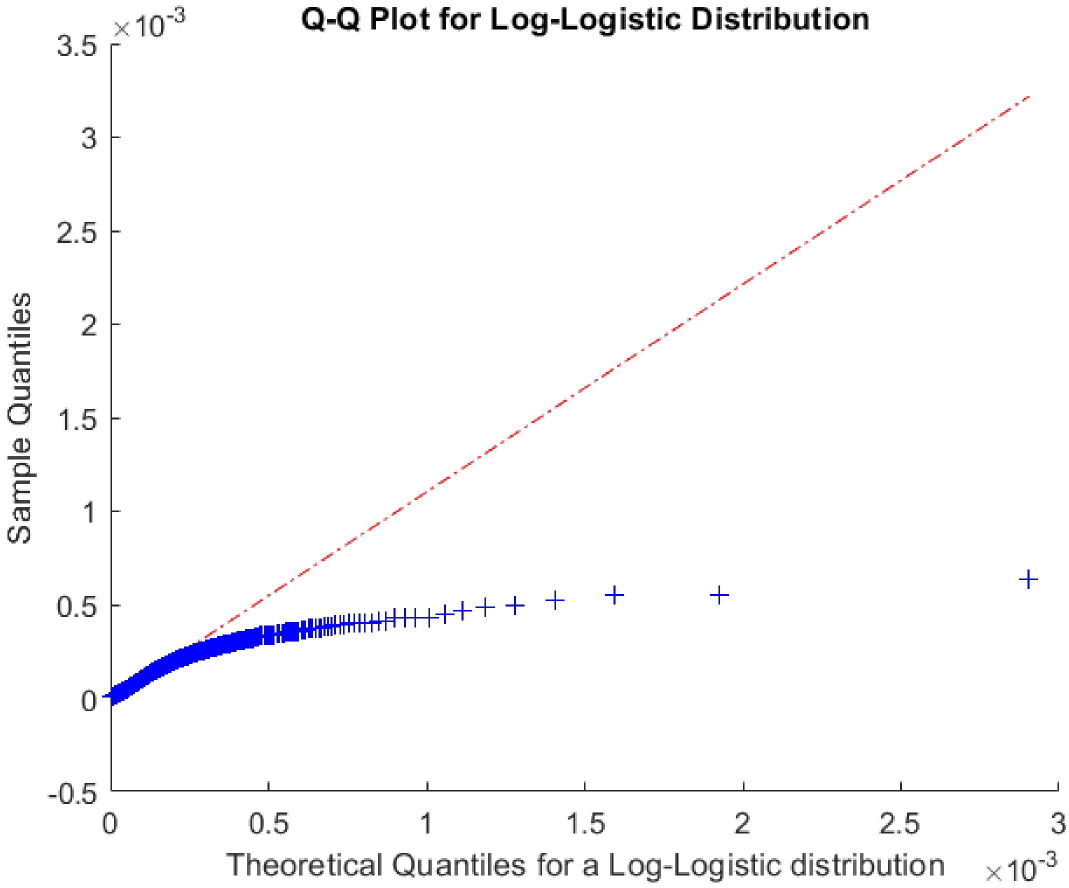

Figure B.5: Q-Q plot of the log-logistic distribution of the analytical vs. empirical distribution.

Table B.1: H and p values for both the lognormal and log-logistic K test for the SI and DI dynamics for the varying noise power.

Dynamics	P_n	H-value lognormal	p-value lognormal	H-value log-logistic	p-value log-logistic
SI	0.05	1	0.0482	1	$4.904 \cdot 10^{-5}$
SI	0.1	0	0.0628	1	$1.743 \cdot 10^{-5}$
SI	0.15	0	0.0834	1	$4.375 \cdot 10^{-5}$
SI	0.2	1	0.0158	1	$1.039 \cdot 10^{-5}$
SI	0.25	1	0.0201	1	$2.154 \cdot 10^{-5}$
DI	0.05	0	0.1135	1	$4.457 \cdot 10^{-5}$
DI	0.1	0	0.1511	1	$4.665 \cdot 10^{-5}$
DI	0.15	1	0.0183	1	$1.661 \cdot 10^{-5}$
DI	0.2	0	0.1948	1	$3.509 \cdot 10^{-5}$
DI	0.25	1	0.0303	1	$7.422 \cdot 10^{-5}$

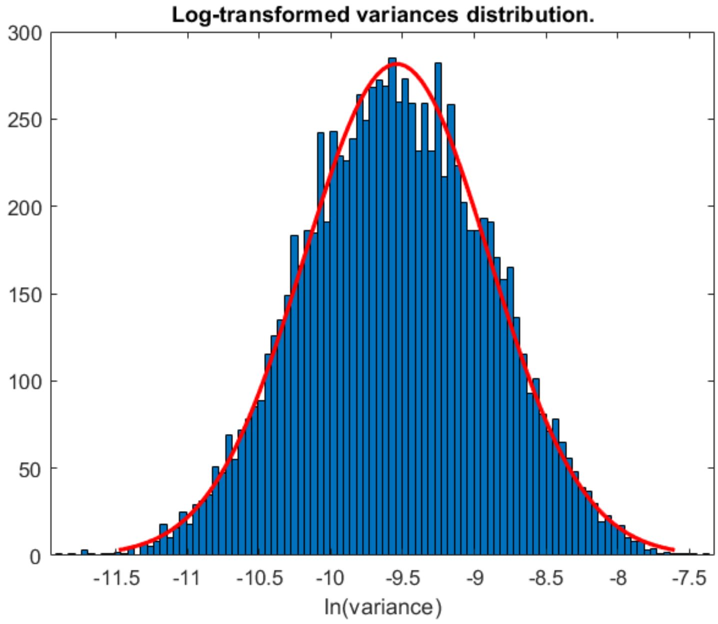

Figure B.6: Log-transformed variances of the Monte Carlo analysis.

Part III

Scientific Article Appendix

C

Additional simulation results

The simulation was also run for different HC and CE dynamics parameter settings. The CE dynamics were, before the transition, single integrator-like and post-transition double integrator-like. However, the CE dynamics pre- and post-transition were more similar. The simulation was still run for an HC with a low crossover frequency and a high crossover frequency. The target function was the same 3,000 crested forcing function as used in the aforementioned simulation. The models for both HC and CE dynamics were the same. Table C.1 shows the extra simulation settings for the HC model and Table C.2. Figures C.1-C.2 show the ROC curves and the average detection times respectively.

Table C.1: Extra simulation settings HC.

HC	K_p (-)	ω_c (rad/s)	ϕ_m (deg)	T_L (s)	T_I (s)	τ_e (s)	ω_{nm} (rad/s)	ζ_{nm} (-)
$\omega_{c_{low}}$	1.3	2	50.5	0	0	0.26	10.5	0.35
$\omega_{c_{high}}$	3.3	3.2	25.9	0	0	0.26	10.5	0.35

Table C.2: Extra simulation settings CE dynamics.

Dynamics	K_c (-)	ω_b (rad/s)
Pre-transition	150	3.22
Post-transition	3.333	0.67

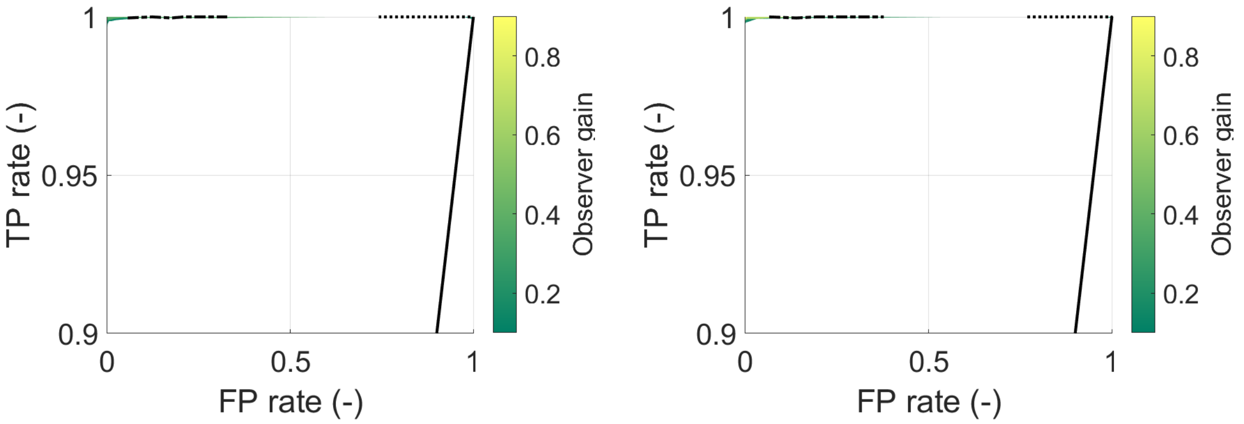

(a) ROC curve for an HC with a $\omega_c = 2$ rad/s, $P_n = 0.05$. (b) ROC curve for an HC with a $\omega_c = 3.2$ rad/s, $P_n = 0.05$.

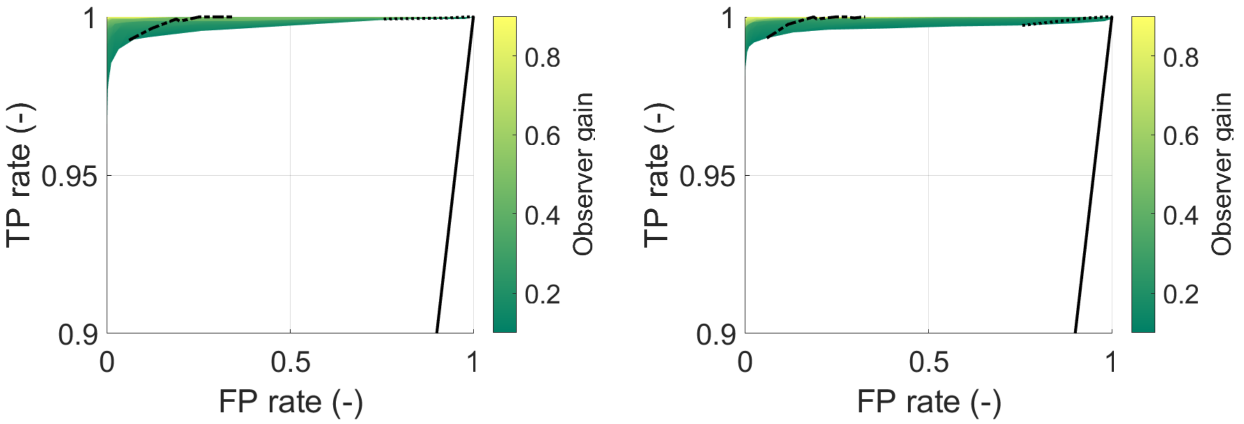

(c) ROC curve for an HC with a $\omega_c = 2$ rad/s, $P_n = 0.1$. (d) ROC curve for an HC with a $\omega_c = 3.2$ rad/s, $P_n = 0.1$.

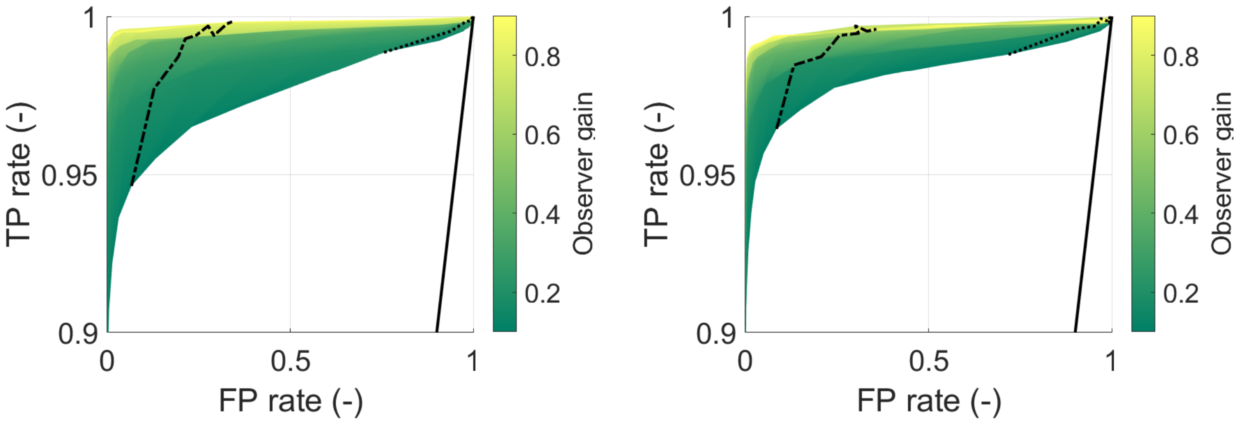

(e) ROC curve for an HC with a $\omega_c = 2$ rad/s, $P_n = 0.2$. (f) ROC curve for an HC with a $\omega_c = 3.2$ rad/s, $P_n = 0.2$.

Figure C.1: ROC curves with the TP against the FP rate, for $C\sigma_\eta$, with C from 1 to 10, calculated with 3,000 target and remnant realisations for various remnant power ratios P_n and observer gain K from 0.1-0.9. With the dash dotted line 3σ_η and the dotted line 2σ_η. Note the y-axis is from 0.9 to 1.

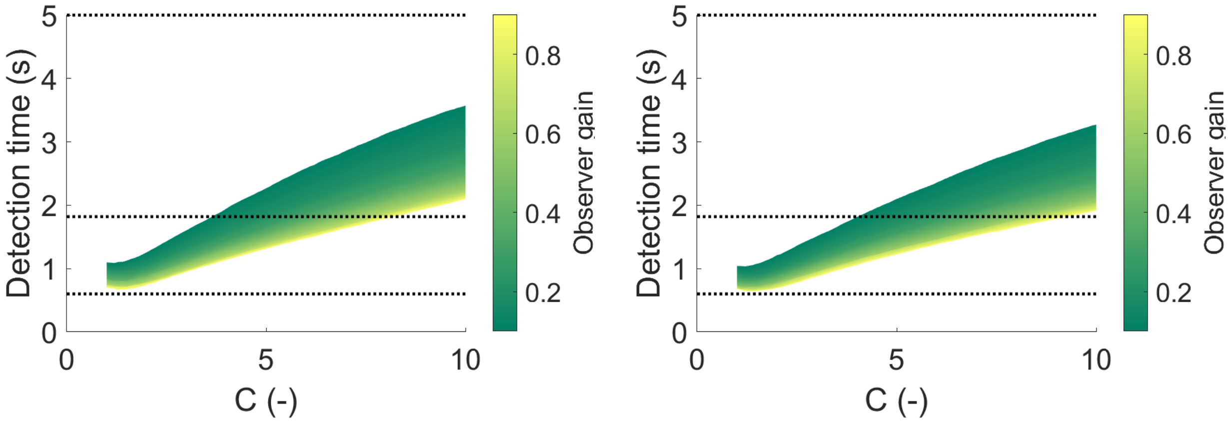

(a) Average detection times against C for an HC with a $\omega_c = 2$ rad/s and $P_n = 0.05$.

(b) Average detection times against C for an HC with a $\omega_c = 3.2$ rad/s and $P_n = 0.05$.

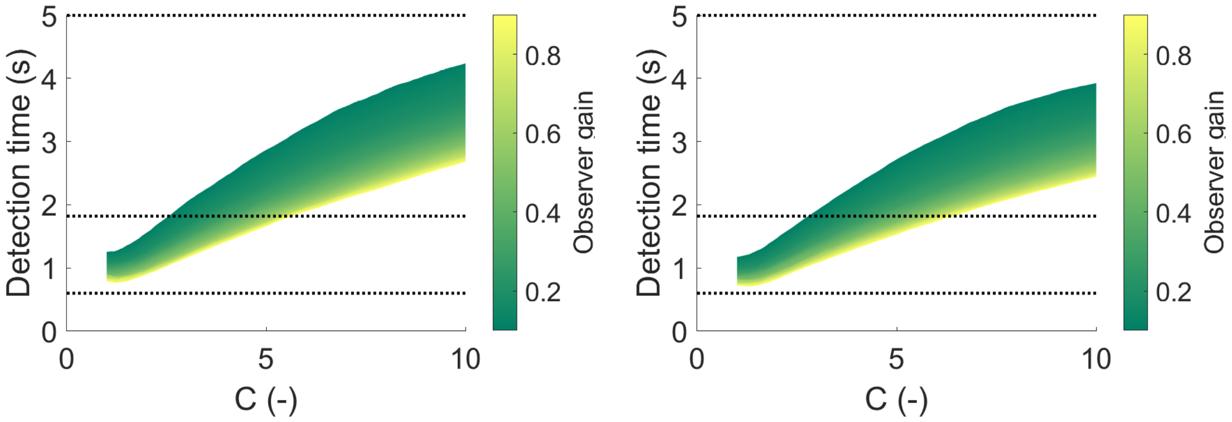

(a) Average detection times against C for an HC with a $\omega_c = 2$ rad/s and $P_n = 0.1$.

(b) Average detection times against C for an HC with a $\omega_c = 3.2$ rad/s and $P_n = 0.1$.

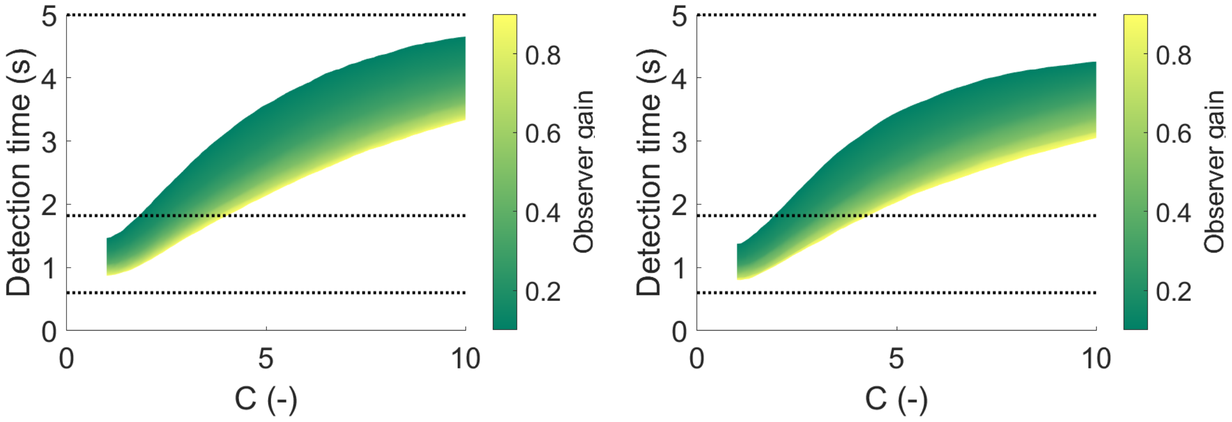

(a) Average detection times against C for an HC with a $\omega_c = 2$ rad/s and $P_n = 0.2$.

(b) Average detection times against C for an HC with a $\omega_c = 3.2$ rad/s and $P_n = 0.2$.

Figure C.2: Average detection time against $C\sigma_\eta$, with C from 1 to 10 for various remnant power ratios P_n and observer gain K from 0.01-0.9. With the fastest, average and slowest detection from the experiment data from Barragan [35] indicated.